

DEVELOPMENT OF BUFFER LAYERS BY CHEMICAL SOLUTION DEPOSITION
FOR YBCO COATED CONDUCTORS

By

YALCIN AKIN

A DISSERTATION PRESENTED TO THE GRADUATE SCHOOL
OF THE UNIVERSITY OF FLORIDA IN PARTIAL FULFILLMENT
OF THE REQUIREMENTS FOR THE DEGREE OF
DOCTOR OF PHILOSOPHY

UNIVERSITY OF FLORIDA

2003

Copyright 2003

by

Yalcin Akin

Dedicated to:

My parents,

and

my wife, Mergin Akin, and my son, Mehmet Ali Akin,

in appreciation of their endless support, guidance, patience, and belief in me.

ACKNOWLEDGMENTS

I would like to take this opportunity to thank first and foremost my advisor, Dr. Wolfgang Sigmund, for his support, guidance and enthusiasm, and I feel very fortunate to have met and worked with him. I also especially thank my co-advisor, Dr. Y.S. Hascicek, from the National High Magnetic Field Laboratory for his guidance, support and his contribution to my professional and personal growth. His knowledge of science, quick solutions on hard problems and humbleness always enlighten me. I sincerely thank my committee members, Drs. E. Dow Whitney, Norton David and Charles R. Martin, for their time, support, comments and suggestions.

I was fortunate enough to get the chance to conduct my dissertation's experiments at the National High Magnetic Field Laboratory (NHMFL) in Tallahassee, FL. For this opportunity, I am indebted especially to Dr. Jack Crow, the director of NHMFL, and Dr. Steven W. Van Sciver, the director of Magnet Science and Technology, for supporting this project and conference travel expense for the latest CEC/ICMC-2003 at The Great Land of Alaska. Working at the NHMFL allowed me to gain incredible experience as I was able to interact with many professional people and scientists to build a network of friends and colleagues. I would also like to thank Dr. Z. K. Heiba for his help on XRD characterization of mixed oxides, and Mr. Robert E. Goddard and Dr. Ulf Trociewitz from NHMFL for their help in microstructure and DTA characterizations. In addition, I would like to extend my thanks to Dr. Hamid Garmestani and Cristiane Bacaltchuk for

their help and discussions about pole figure characterization of materials, and to many others from Dr. Sigmund's and Dr. Hascicek's group.

Financial support from Turkish Higher Education Council and National Science Foundation (NSF) is gratefully acknowledged.

Last but not least I would like to thank my wife, my son, my parents and my brother for their motivation, encouragement, support and love.

TABLE OF CONTENTS

	<u>page</u>
ACKNOWLEDGMENTS.....	iv
LIST OF TABLES	viii
LIST OF FIGURES.....	ix
ABSTRACT	xii
 CHAPTERS	
1 INTRODUCTION.....	1
1.1 Brief History.....	1
1.2 Motivation.....	2
1.3 Problem Definition	5
1.3 Contribution to the Field	6
 2 LITERATURE REVIEW	 8
2.1 Introduction	8
2.2 Explanation of Biaxial Texture	12
2.3 Substrates	15
2.3.1. Polycrystalline Non-Textured Substrates.....	15
2.3.2 Rolling Assisted Biaxially Textured Substrates (RABiTS™)	15
2.3.2.1 Biaxial texture formation in pure FCC metals	16
2.3.2.2 Biaxially textured Ni alloys.....	18
2.4 Buffer Layers.....	21
2.4.1 Conducting Buffer Layers.....	24
2.4.2 Effect of Sulfur Structure on Growth of Biaxially textured Buffer Layers	25
2.5 YBCO Films.....	25
2.6 Fabrication of YBCO Coated Conductors by Vacuum Deposition Approaches	27
2.6.1 Buffer Layers Deposition Techniques.....	28
2.6.1.1 Ion beam assisted deposition.....	28
2.6.1.2 Inclined substrate deposition.....	31
2.6.2 YBCO Deposition	32
2.6.2.1 Grain boundary issues in YBCO thin films	34
2.6.2.2 Thickness issues in YBCO thin films	36

2.7 Chemical Solution Deposition Approaches	37
2.7.1 Fundamental	37
2.7.2 Sol-Gel Process	38
2.7.3 Chelate Process	39
2.7.4 MOD Solution Synthesis	40
2.7.5 Thin Films Coatings	41
2.7.5.1 Dip coatings	42
2.7.5.2 Spin coatings	42
2.7.6 Chemical Solution Deposition of Buffer Layers	43
2.7.7 Chemical Solution Deposition of YBCO	43
3 EXPERIMENTAL PROCEDURES	46
3.1 Substrate Preparation	46
3.2 Processing of CeO ₂ Buffer Layers by Chemical Solution Deposition	47
3.3. Engineered Buffer Layers for 100% Lattice Match with YBCO	50
3.4 Microstructure Characterization	53
3.4.1 Differential Thermal Analysis (DTA)	53
3.4.2 X-ray Diffraction Analysis (XRD)	54
3.4.3 Environmental Electron Microscopy (ESEM)	57
3.4.4 Orientation Imaging Microscopy (OIM)	58
3.4.5 Energy Dispersive X-ray Spectroscopy	60
4 RESULTS AND DISCUSSIONS	61
4.1 Processing and Characterization of Textured Nickel Substrate	61
4.2 Processing and Characterization of CeO ₂ Buffer Layers	71
4.3 Processing and Characterization of (Eu _{1-x} Yb _x) ₂ O ₃ Buffer Layers	84
4.4 Multi Buffer Layers Structures	100
5 CONCLUSIONS	109
5.1 Conclusions	109
5.2 Suggestions for Future Work	112
LIST OF REFERENCES	115
BIOGRAPHICAL SKETCH	128

LIST OF TABLES

<u>Table</u>	<u>Page</u>
4.1. Some of the physical properties of Ni and CeO ₂	74
4.2. FWHM values of ω and ϕ - scans of Ni and CeO ₂ buffer layers, which were annealed at varying conditions	80
4.3. Some of the physical properties and lattice mismatches of selected oxides with Ni and YBCO.....	88
4.4. Lattice parameters of (Eu _{1-u} Yb _u) ₂ O ₃ for varying “u” values.....	90
4.5. FWHM values of ω and ϕ - scans of Ni and (Eu _{0.893} Yb _{0.107}) ₂ O ₃ buffer layers, which were annealed at varying conditions.....	95
4.6. FWHM values of ω and ϕ - scans of Ni and (Eu _{0.893} Yb _{0.107}) ₂ O ₃ buffer layers, which were coated 5 times with dip coating process.....	97
4.7. FWHM values of ω and ϕ - scans of Ni, Gd ₂ O ₃ /Ni, CeO ₂ /Gd ₂ O ₃ /Ni and (Eu _{0.893} Yb _{0.107}) ₂ O ₃ /CeO ₂ /Gd ₂ O ₃ /Ni buffer layers structures.....	106

LIST OF FIGURES

<u>Figure</u>	<u>Page</u>
2.1. Schematic drawing of a typical YBCO coated conductor.....	11
2.2. Schematic representation of alignments of grains.....	14
2.3. Schematic of RABiTS™ process for fabrication of HTS coated conductors.....	16
2.4. Schematic of IBAD process for fabrication of HTS coated conductors	30
3.1. The picture of the 0.5 cm wide Ni tape as wrapped on a quartz tube for annealing process	46
3.2. The reel-to-reel dip coating system with an in-line three zone furnace	49
4.1. The X-ray $\theta/2\theta$ scan of a bulk Ni piece, a cold rolled Ni tape, and an annealed Ni tape	62
4.2. The logarithmic scale and background corrected typical (111) pole figures of Ni substrates	63
4.3. The ω - scan of biaxially textured Ni substrate, which was annealed at 1050 °C for 30 min.	65
4.4. The ϕ - scan of (111) plane of the biaxially textured Ni substrate, which was annealed at 1050 °C for 30 min.....	65
4.5. FWHM values of ω and ϕ - scans of 10 cm long biaxially textured Ni substrates, which were annealed at 1050 °C for 30 min.....	67
4.6. EBSD patterns of a biaxially textured Ni substrate	68
4.7. OIM Micrographs of biaxially textured Ni substrate	69
4.8. ESEM micrographs of biaxially textured Ni substrate, which was annealed at 1050 °C for 30 min. Grain boundary grooves are clearly seen from the surface plain view micrographs.....	70

4.9. Plane view schematic drawing of crystal structures of CeO_2 and YBCO. Only Ce atoms of CeO_2 and Cu atoms of YBCO are shown	73
4.10. Plane view schematic drawing of crystal structures of CeO_2 and Ni. Only Ce atoms of CeO_2 and Ni atoms are shown	73
4.11. Surface morphologies of non-continuous CeO_2 films on biaxially textured Ni substrate, which was processed from 0.05 M Ce cation precursor solution	75
4.12. Surface morphologies of cracked CeO_2 films on biaxially textured Ni substrate, which was processed from 0.15 M Ce cation precursor solution.....	76
4.13. DTA analysis of RT dried Ce xerogels	77
4.14. The X-ray $\theta/2\theta$ scans of CeO_2 buffer layers, which were annealed at varying temperatures and time as marked, on biaxially textured Ni substrate.....	78
4.15. The logarithmic scale and background corrected (111) pole figures	79
4.16. The ω - scan of biaxially textured CeO_2 buffer layer, which was annealed at 1150 °C for 10 min., on biaxially textured Ni substrate.....	81
4.17. The ϕ - scan of biaxially textured CeO_2 , which was annealed at 1150 °C for 10 min., on biaxially textured Ni substrate	82
4.18. FWHMs of ω and ϕ - scan of 10 cm long biaxially textured CeO_2 buffer layer, which was annealed at 1150 °C for 10 min., on biaxially textured Ni substrate	82
4.19. Surface morphologies of biaxially textured CeO_2 films on biaxially textured Ni substrate.....	83
4.20. Schematic illustration of heteroepitaxial structures	85
4.21. The X-ray diffraction patterns of the powder samples of $(\text{Eu}_{1-u}\text{Yb}_u)_2\text{O}_3$ for varying “u” values as marked	89
4.22. Variation of the lattice parameter of $(\text{Eu}_{1-u}\text{Yb}_u)_2\text{O}_3$ for varying “u” values	90
4.23. Surface morphologies of non-continuous $(\text{Eu}_{0.893}\text{Yb}_{0.107})_2\text{O}_3$ films, which was processed from 0.05 M precursor solution, on biaxially textured Ni substrate	92
4.24. The X-ray $\theta/2\theta$ scans of $(\text{Eu}_{0.893}\text{Yb}_{0.107})_2\text{O}_3$ buffer layers, which were annealed at varying temperatures and time, on biaxially textured Ni substrate	93
4.25. The logarithmic scale and background corrected (222) pole figure of $(\text{Eu}_{0.893}\text{Yb}_{0.107})_2\text{O}_3$ buffer layer, which was annealed at 1150 °C for 10 min., on biaxially textured Ni substrate.	93

4.26. The ω - scan of biaxially textured $(\text{Eu}_{0.893}\text{Yb}_{0.107})_2\text{O}_3$ buffer layer, which was annealed at 1150 °C for 10 min., on biaxially textured Ni substrate.....	95
4.27. The ϕ - scan of biaxially textured $(\text{Eu}_{0.893}\text{Yb}_{0.107})_2\text{O}_3$ buffer layer, which was annealed at 1150 °C for 10 min., on biaxially textured Ni substrate.....	96
4.28. FWHM values of ω and ϕ - scans of 10 cm long biaxially textured $(\text{Eu}_{0.893}\text{Yb}_{0.107})_2\text{O}_3$ buffer layer, which was annealed at 1150 °C for 10 min., on biaxially textured Ni substrate.....	97
4.29. The X-ray $\theta/2\theta$ scan of $(\text{Eu}_{0.893}\text{Yb}_{0.107})_2\text{O}_3$ buffer layers which were dip coated multiple times as marked.....	98
4.30. Surface morphologies of biaxially textured $(\text{Eu}_{0.893}\text{Yb}_{0.107})_2\text{O}_3$ films on biaxially textured Ni substrate.....	99
4.31. The ω - scan of $\text{CeO}_2/\text{Gd}_2\text{O}_3$ buffer layer structure, which was annealed at 1150 °C for 10 min., on biaxially textured Ni substrate.....	101
4.32. The ϕ - scan of $\text{CeO}_2/\text{Gd}_2\text{O}_3$ buffer layer structure, which was annealed at 1150 °C for 10 min., on biaxially textured Ni substrate.....	102
4.33. EDS spectrum of $\text{CeO}_2/\text{Gd}_2\text{O}_3$ buffer layers structure and the Ni substrate	102
4.34. ESEM micrographs of $\text{CeO}_2/\text{Gd}_2\text{O}_3$ buffer layers structure on biaxially textured Ni substrate.....	104
4.35. The ω - scan of $(\text{Eu}_{0.893}\text{Yb}_{0.107})_2\text{O}_3/\text{CeO}_2/\text{Gd}_2\text{O}_3$ buffer layers structure, which was annealed at 1150 °C for 10 min., on biaxially textured Ni substrate.....	105
4.36. The ϕ - scan of $(\text{Eu}_{0.893}\text{Yb}_{0.107})_2\text{O}_3/\text{CeO}_2/\text{Gd}_2\text{O}_3$ buffer layers structure, which was annealed at 1150 °C for 10 min., on biaxially textured Ni substrate.....	105
4.37. EDS spectrum of $(\text{Eu}_{0.893}\text{Yb}_{0.107})_2\text{O}_3/\text{CeO}_2/\text{Gd}_2\text{O}_3$ buffer layers structure and Ni substrate.....	106
4.38. ESEM micrographs of $(\text{Eu}_{0.893}\text{Yb}_{0.107})_2\text{O}_3/\text{CeO}_2/\text{Gd}_2\text{O}_3$ buffer layers structure on biaxially textured Ni substrate	108

Abstract of Dissertation Presented to the Graduate School
of the University of Florida in Partial Fulfillment of the
Requirements for the Degree of Doctor of Philosophy

DEVELOPMENT OF BUFFER LAYERS BY CHEMICAL SOLUTION DEPOSITION
FOR YBCO COATED CONDUCTORS

By

Yalcin Akin

December 2003

Chairman: Wolfgang Sigmund

Major Department: Materials Science and Engineering

Short length YBCO coated conductors have been fabricated by vacuum thin film deposition techniques. However, the fabrication process increases the cost, and makes them impractical to use for commercial applications even if they are fabricated in kilometer lengths. YBCO coated conductors could be available in the market with a cheaper price by developing non-vacuum deposition techniques. The objective of this research was to investigate development of buffer layers by chemical solution deposition technique for YBCO coated conductors. Buffer layer structures are mainly used to prevent metal ion diffusion, and to reduce the lattice mismatch between YBCO and the metallic substrate. The technical approach, which was adapted here, is the reel-to-reel sol-gel dip coating process to fabricate long length coatings by developing buffer layers' chemical solutions. Rolling assisted biaxially textured Ni substrates were used for deposition of buffer layers. Cold rolled Ni strips were heat-treated at certain conditions to form biaxially textured structure, which became templates for textured growth of buffer layers that is necessary to obtain high critical current in the coated conductors. CeO_2 was

chosen as a buffer layers because it has been recognized as one of the best cap layers. Growth of highly textured, crack free, pinhole free and smooth CeO_2 buffer layers have been demonstrated by chemical solution deposition technique on biaxially textured substrates. A new buffer layer with pseudocubic lattice parameters matching YBCO, $(\text{Eu}_{0.893}\text{Yb}_{0.107})_2\text{O}_3$, was developed for the first time by using a mixture of Eu_2O_3 and Yb_2O_3 to eliminate lattice mismatch, which adversely affected the critical current of the coated conductors. Highly textured $(\text{Eu}_{0.893}\text{Yb}_{0.107})_2\text{O}_3$ buffer layers were deposited on biaxially textured Ni substrates by chemical solution deposition technique. Finally, the growth of CeO_2 and $(\text{Eu}_{0.893}\text{Yb}_{0.107})_2\text{O}_3$ buffer layers were investigated on oxide layers because both CeO_2 and $(\text{Eu}_{0.893}\text{Yb}_{0.107})_2\text{O}_3$ are used as cap layers. CeO_2 buffer layers were deposited on Gd_2O_3 buffer layers and $(\text{Eu}_{0.893}\text{Yb}_{0.107})_2\text{O}_3$ buffer layers were deposited on $\text{CeO}_2/\text{Gd}_2\text{O}_3$ buffer layers structure. It has been demonstrated that biaxially textured buffer layers can be grown on both biaxially textured metallic substrates and oxide thin films. These results are very promising for applicability of chemical solution deposition technique for coated conductors fabrication.

CHAPTER 1 INTRODUCTION

1.1 Brief History

Superconductors have been known since 1911. The superconducting transition temperature, which is called critical temperature (T_c), of the first discovered superconductor is around 4 K [1]. Therefore, liquid helium (4.2 K) had to be used to cool the material to obtain the superconducting state. After discovery of the first superconducting materials, scientists from all over the world started to search for new superconducting materials, because superconductors have no resistance to electric current flow offering the feasibility of new electric power equipment with improved energy efficiency, smaller size, and lower operating costs. Since liquid nitrogen is much cheaper than liquid helium (liquid nitrogen typically costs 35 cents per liter versus \$2.75 per liter for liquid helium), finding new superconducting materials with higher T_c than the boiling temperature of liquid nitrogen (77 K), was highly sought after all over the world.

$\text{YBa}_2\text{Cu}_3\text{O}_{7-\delta}$ (YBCO), with critical temperature of 92 K above the boiling temperature of liquid nitrogen, was discovered after 76 years passed from discovery of the first superconductor [2]. Later, other superconducting materials with higher critical temperatures were found, and they were called high temperature superconductors (HTS). Long length and flexible HTS, which is called first generation HTS tapes, have been fabricated by powder-in-tube (PIT) method using $\text{Bi}_2\text{Sr}_2\text{Ca}_1\text{Cu}_2\text{O}_{8+\delta}$ superconductor ($T_c \sim 80$ K) [3, 4]. Fabrication of HTS tapes by coating YBCO thin films on metallic substrates

is called coated conductors or second generation HTS conductors. YBCO coated conductors are very attractive because of the superior performance of YBCO in high magnetic fields compared to other superconductors [5, 6]. However, YBCO coated conductors have not been fabricated in commercial lengths, except for a new lone promising result in 2002. The maximum length of good quality YBCO coated conductors (critical current density, $J_c = 10^6 \text{ A/cm}^2$) is about 10 meter so far[4].

1.2 Motivation

Demand on increasing capacity of utility power systems in crowded cities motivates research to find more efficient and cost effective underground cables and power transformers because of reaching capacity of today's conventional power systems. Currently 70% of the U.S. transmission lines and transformers are over 25 years old, which is close to their designed lifespan. Moreover, almost 7% of the total generated electricity, which corresponds to billions of dollars, is now lost in existing transmission lines and power distribution systems [7]. These underground transmission cable power systems will need to be replaced with in the next 15-20 years with either the same conventional cables and power systems but in bigger size or high temperature superconducting power systems in smaller size. Billions of dollars could be saved by taking advantage of zero resistance capabilities of HTS cables and power systems. Therefore, this is an opportune time for high temperature superconducting cables and superconducting power system components to replace conventional cables and power utility systems. However, some fundamental problems still remain in fabrications of HTS wires and YBCO coated conductors, and these problems have to be resolved before the window of opportunity is reached.

Mainly, fundamental requirements for superconducting wires are flexibility and high current carrying capacity for potential applications such as power transmission cables, motors, transformers, superconducting coils, etc. The amount of current a superconducting wire can carry before losing its superconducting properties is called the critical current (I_c). Intrinsic properties of Bi-based superconductors limit the operation conditions of the Bi-based wires and prototype devices to either low magnetic fields and high temperatures (>75 K), or to low temperatures (<30 K) for high magnetic fields, because Bi-based HTS tapes can only carry sufficient I_c in these operating conditions [6, 8]. Critical engineering current density, (J_c), of a typical HTS conductor is around 15 kA/cm^2 at 77 K and self magnetic field [4]. The J_c dramatically decreases with external weak magnetic fields as low as (0.5 Tesla (T)) which is the magnetic field of most electric power systems such as transformers, motors, and generators. The current price of Bi-2223/Ag superconducting tape is approximately \$200/kA-m and is predicted to fall to approximately \$50/kA-m as manufacturing capacity increases [9]. It has been estimated that approximately 1.5 tons of silver are needed to produce one mile of cable with the PIT method [7]. The current density of a copper conductor used in cable or in a transformer/reactor winding is between 100 to 400 A/cm^2 and the price of the cable is \$10 – 30/kA-m [10].

Compared with Bi-based compounds, typical high quality YBCO coated conductors can have high J_c and J_{c0} , which are around 2 MA/cm^2 and 33 kA/cm^2 (*total thickness of the one side coated conductors was assumed to be $60 \text{ }\mu\text{m}$ including $55 \text{ }\mu\text{m}$ thick substrate), respectively, in moderate magnetic fields at 77 K. Since nickel and YBCO are incompatible, fabrication of long length high quality YBCO coated conductors

can only be achieved by deposition of biaxially textured oxide buffer layers between Ni and YBCO layers. These buffer layers provide structural template and chemical barriers for the subsequent YBCO depositions [11]. Therefore deposition of biaxially textured buffer layers is extremely important, and they play a crucial role for deposition of biaxially textured YBCO films. Currently, the most preferred buffer layers structure is the $\text{CeO}_2/\text{YSZ}/\text{CeO}_2$ three-layer structure, which has been grown on biaxially textured nickel tapes by conventional vacuum techniques [12-14]. Growths of different oxide buffer layers have been investigated and some of them deposited on biaxially textured substrates by non-vacuum chemical solution deposition techniques[15-18]. Chemical solution deposition of all the layers and YBCO layer dramatically reduces the cost of YBCO coated conductors because of fast deposition rate, low cost of capital equipment and inexpensive coating process. Only few candidate buffer layer systems have so far developed by solution deposition technique; therefore, a combination of chemical solution deposition and vacuum deposition techniques could be the current solution of the fabrication of long length YBCO coated conductors with reduced cost. If deposition of even one or two layers i.e., CeO_2 out of four layers are deposited by chemical solution techniques, fabrication cost of YBCO coated conductors would be reduced. It is estimated that high quality YBCO coated conductors will be manufactured in kilometer lengths in 2005, and the cost of wires will be less than \$50/kA-m at 77 K operating conditions [7].

Currently, processing of high quality short length YBCO coated conductors has been demonstrated with vacuum thin film deposition techniques the scale-up of which is very challenging, and the deposition rates are very slow, around 0.6 m/h. On the other

hand, non-vacuum chemical solution deposition techniques are very attractive because the double sides of the substrate can be coated by non-vacuum dip coating technique in one coating process that would double the engineering current density, $J_e \sim 66 \text{ kA/cm}^2$ of the conductor, if quality of the conductor is same in both sides. Fast deposition rates, low cost, easy to scale up by reel to reel deposition system, better homogeneity and composition control make chemical solution deposition techniques extremely fascinating for deposition of both YBCO films and buffer layers.

1.3 Problem Definition

One of the main obstacles for manufacturing commercial lengths of YBCO coated conductors is the lack of having the uniform highly textured structures with low angle grain boundaries over the entire length of conductors. The high angle grain boundaries in the YBCO layer, which have been known as weak links as far as current carrying capacity is concerned, have to be avoided [19, 20]. Therefore, YBCO grains have to be highly aligned to obtain low angle boundaries ($5^\circ - 7^\circ$). Highly textured YBCO films have been grown on biaxially textured buffer layers using ion beam assisted deposition (IBAD) technique [5, 21] and using rolling assisted biaxially textured substrates (RABITSTM) by various vacuum and non-vacuum deposition techniques in short lengths [8, 11]. Basically, the textured structures of buffer layers determine grain boundary misorientations of YBCO films. $1 - 2 \text{ MA/cm}^2$ critical current density can be obtained in highly textured YBCO films at 77 K in the presence of moderate external magnetic field [22]. Epitaxial growth of YBCO films on biaxially textured buffer layers is the solution for commercialization of YBCO coated conductors, but only high quality short length YBCO coated conductors have been fabricated so far [23]. The main

problem associated with development of long length coated conductors is control of texture quality of both buffer layers and YBCO films over the length of the conductor. The second obstacle is that thick YBCO films about 5 μm with high critical current densities are desirable for potential applications, however, critical current density of the conductor decreases with increasing YBCO thickness because of formation of high angle grain boundaries and maybe grains with totally different orientations [24]. Also surface roughness of the YBCO increases with increasing the thickness of the YBCO film, and high surface roughness causes poor connectivity in the YBCO; as a result J_c decreases with increasing surface roughness [24]. Challenges remain in maintaining high J_c of YBCO coated conductors while increasing film thickness and deposition rates on long length tapes. Grain boundary grooving in the substrates, grain boundary misorientations, and defects need to be controlled for fabrication of high J_c YBCO coated conductors [25].

Up to now the most successful YBCO deposition techniques on biaxially textured buffer layers are pulsed laser deposition (PLD) and non-vacuum chemical solution deposition technique using trifluoroacetic acid precursor solutions [26]. Non-vacuum chemical solution deposition techniques offer very fast deposition rates and double sided coating compared to vacuum techniques. However, more research needs to be done on deposition of long length buffer layers and YBCO films by non-vacuum chemical solution deposition techniques to understand and control problems of epitaxial growth over the length.

1.4 Contribution to the field

Growth of buffer layers is generally carried out by vacuum deposition processes for fabrication of YBCO coated conductors. However, more adaptive and easily scalable

processing techniques are highly desired to fabricate coated conductors for practical applications. Chemical solution deposition of buffer layers would dramatically reduce cost of YBCO coated conductors because of fast deposition rate, low cost and inexpensive coating process. It is easy to scale up for deposition of kilometers long buffer layers compared to vacuum thin film deposition techniques. Therefore, chemical solution deposition of buffer layers was investigated in this work. A wet-chemical process was developed for deposition of the most preferred buffer layer, which is CeO_2 for YBCO coated conductors. The sol-gel dip coating process was adapted and the processing parameters were established. Using the process biaxially textured, crack free and pin hole free buffer layers were grown on biaxially textured Ni substrates and Gd_2O_3 buffer layers. Also a new buffer layer, $(\text{Eu}_{0.893}\text{Yb}_{0.107})_2\text{O}_3$, was developed for the first time by mixing of Eu_2O_3 and Yb_2O_3 . Pseudocubic lattice parameters of this buffer layer are the same as the lattice parameter of YBCO. By fabricating $(\text{Eu}_{0.893}\text{Yb}_{0.107})_2\text{O}_3$ buffer layers, buffer layer induced strain effects due to lattice mismatch were eliminated at the interface of the cap layers and YBCO. A wet-chemical process was also developed for $(\text{Eu}_{0.893}\text{Yb}_{0.107})_2\text{O}_3$, and processing parameters were established for biaxial textured growth. Biaxially textured $(\text{Eu}_{0.893}\text{Yb}_{0.107})_2\text{O}_3$ were grown on biaxially textured Ni substrate and $\text{Gd}_2\text{O}_3/\text{CeO}_2$ buffer layers structure. It was demonstrated that highly textured buffer layers could be synthesized via a wet-chemical method on biaxially textured Ni substrates and oxide thin films.

CHAPTER 2 LITERATURE REVIEW

2.1 Introduction

A phenomenon of superconductivity was first discovered by Kamerlingh Onnes in 1911. Having developed a method to liquefy helium, he undertook a systematic study of the properties of matters at low temperature. He chose pure mercury as his sample, and discovered the first superconductor that at a temperature close to 4 K the electrical resistance of it abruptly vanished. The phenomenon of superconductivity is manifested in the electrical resistance vanishing at a finite temperature [1]. Superconducting metals, alloys and compounds were also discovered such as vanadium–silicon V_3Si in 1953, and T_c of V_3Si was found to be 17.1 K [27]. Until 1975 more than 2000 superconductors had been discovered, and the critical temperature had reached up to 22.3 K with the discovery of Nb_3Ge in 1973. A theoretical understanding of superconductivity was advanced in 1957 by BCS theory [28]. The BCS theory explained superconductivity at temperature close to absolute zero. Even when the BCS theory explained the phenomena of low temperature superconductivity, many scientists believed that higher critical temperatures could not be reached without finding new superconducting phenomena. The BCS theory has later become insufficient to fully explain electron behavior of superconductors, after the discovery of different superconductor systems with higher T_c .

In 1986, a truly breakthrough discovery was made in the field of superconductivity. G. Bednorz and K.A. Müller (IBM-Zurich) discovered a new class of

superconducting material, a ceramic compound (La-Ba-Cu-O) system [29] that superconducted at the highest temperature around 35 K. The discovery of the first superconducting ceramics won Bednorz and Müller a Nobel Prize the following year. This discovery was so remarkable because ceramics were normally known as insulators up to the discovery of ceramic superconductors. Only a year later, Chu et al. announced that a compound Y-Ba-Cu-O [2] system becomes superconducting at a temperature higher than that of liquid nitrogen: its T_c is around 92 K, and in the following 12 months, many new compounds were discovered. Notable among these were the Bi-Sr-Cu-O compound discovered by Michel et al. [30] (France), the Bi-Sr-Ca-Cu-O compound discovered by Maeda et al. [31] (Japan), with transition temperatures up to 115 K. Tl-Ca-Ba-Cu-O system with $T_c \sim 125$ K was discovered in 1988 by Sheng and Hermann [32] (Uni. of Arkansas). Among the high temperature superconductors, $\text{HgBa}_2\text{Ca}_2\text{Cu}_3\text{O}_{8+\delta}$ (Hg-1223) has the highest zero resistance $T_c \sim 135$ K at ambient pressure [33]. Today over 6000 superconducting materials are known and the majority of superconductors are alloys. The active search for new superconducting materials continues, and this number is constantly growing. It is possible that higher T_c 's will be found [1].

In the last decade, several high T_c superconducting (HTS) materials such as $\text{Bi}_2\text{Sr}_2\text{Ca}_2\text{Cu}_3\text{O}_{10}$ (BSCCO) [3, 4, 34], $\text{Tl}_2\text{Ba}_2\text{Ca}_2\text{Cu}_3\text{O}_{10}$ (TBCCO) [35, 36] and $\text{YBa}_2\text{Cu}_3\text{O}_{7-\delta}$ (YBCO) [8, 21] have been studied for technological applications. Significant progress has been made towards fabricating long length and flexible multi filamentary HTS conductors by (PIT) process using Bi-2212/(Ag/Ag-x) and Bi-2223/(Ag/Ag-x) compounds [4]. In this process silver tubes are filled with HTS materials Bi-2212 or Bi-2223, and then processed by a combination of drawing, rolling, and

heating steps, which is called thermo-mechanical process [3]. The PIT process has become the most promising technique for making long length Bi based superconducting tapes with good electrical and mechanical properties, and these wires are used in transformers, motors, and fault current limiters. Even though considerable progress is made in improving the critical current density which is critical current (I_c) divided by cross-sectional area of the superconductor, strain tolerance of it, and long length performance of these conductors, they are still in no way even close to the performance of YBCO thin films in the presence of external magnetic fields [4, 37]. Therefore, among these materials $\text{YBa}_2\text{Cu}_3\text{O}_{7-\delta}$ is the most promising material for HTS applications because it is readily synthesized in bulk and textured in thin film form. YBCO films do not require a special handling method. On the other hand, other high temperature superconductors like thallium and mercury are toxic.

Extensive research has been going on in many universities [38-40], national labs [41-44], and some major US companies [4, 37, 45] to develop high quality, long length and flexible YBCO coated conductors [46]. A schematic drawing of typical YBCO coated conductor is seen in Figure 2.1. It consists of a metallic substrate, three buffer layers, a YBCO layer, and the final silver layer. Mainly there are two approaches to attain long length YBCO coated conductors with high critical current densities ($>10^6 \text{ A/cm}^2$). The first one is deposition of biaxially textured buffer layers by complex deposition techniques like ion beam assisted deposition, (IBAD) [21] or incline substrate deposition (ISD) techniques [47] on polycrystalline metallic substrates followed by epitaxial growth of YBCO layers. In the second approach, first biaxially textured metal substrates are formed by thermomechanical process; after that biaxially textured buffer layers and

superconducting layers are grown on the substrates[8, 11]. In each case, the ultimate objective is to have biaxially textured YBCO layers with low angle grain boundaries.

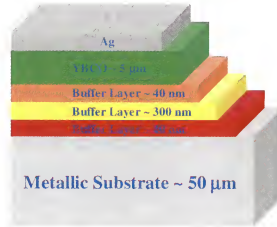


Figure 2.1. Schematic drawing of a typical YBCO coated conductor. Fabrication of short length, biaxially textured, YBCO coated conductors with $> 1 \text{ MA/cm}^2$ critical current density has been demonstrated using various conventional vacuum techniques. In 1995, 4 cm long YBCO coated conductor with 1 MA/cm^2 at 77 K was fabricated [48]; after that 1 meter long YBCO coated conductor was reported by pulsed laser deposition technique (PLD) in Los Alamos National Laboratory [49]. Six years later, the Los Alamos team and most others still cannot make YBCO coated conductors longer than a meter, kilometers of which are needed for commercial and military applications [23].

In order to stimulate the development of YBCO coated conductors in the U.S., critical goals and dates, which were set by the Department of Energy (DOE) to be achieved by December 2003 include one meter long YBCO coated conductor with critical current measured end-to-end greater than 100 Amps per centimeter of width of the wire; and 10 meters long with critical current measured end-to-end greater than 50 Amps per centimeter of width of the wire [50]. American Superconductors (AMSC)

fabricated 10-meter long YBCO coated conductors in October 2002 using metal organic decomposition technique for YBCO films. The measurements in AMSC and the Oak Ridge National Laboratory confirmed that AMSC has achieved fabrication of YBCO coated conductors with I_c over 100 Amps on 10 meter long wires 15 months ahead of the original DOE goal [51]. A high quality 11 meters of YBCO coated conductor was fabricated in 2002 [23]. These improvements are very impressive but not close to being ready for practical uses.

A new 10,000 square feet Los Alamos Research Park Building under the Los Alamos National Laboratory and two new laboratories approximately 2,500 square feet in the Oak Ridge National Laboratory were dedicated in April 2001 for fabrication and evaluation of long length coated conductors, and technology transfer to industrial partners under the Department of Energy Accelerated Coated Conductors Initiative. It is anticipated that YBCO coated conductors will be available in km length in 2005 [7].

2.2 Explanation of Biaxial Texture

The meaning of crystallographic texture is preferred alignment of grains in a polycrystalline material [52]. In the case of biaxial texture all the grains should be aligned both perpendicular to the plane of the substrate (out-of-plane) and parallel to the plane of the substrate (in-plane). When all grains of a polycrystalline material are aligned to within 20° with respect to all three crystallographic axes, the texture of materials is called biaxial texture [53]. However, less than 10° is desirable for YBCO coated conductors. X-ray pole figure, rocking curve and phi scans give complete information about degree of biaxial texture, and these techniques will be explained in the experimental and discussions parts of the dissertation. The degrees of alignments such as out-of-plane and

in-plane textures are quantified by full-width-at-half maximum (FWHM) values of rocking curve (ω - scan) and phi (ϕ)- scans, respectively. Figure 2.2(a), (b), and (c) represents randomly oriented grains, only out-of-plane aligned grains (c-axis aligned grains) and both out-of-plane and in-plane aligned grains (biaxial texture), respectively.

One of the most important properties of YBCO coated conductors is high current carrying capacity, and many important potential applications of the coated conductors require flexible, long conductors with high J_c in low and high magnetic fields. However, randomly oriented polycrystalline thin film or bulk YBCO could carry no more current than copper wire because of high angle grain boundaries. Dimos et al. investigated the relationship between grain boundary misorientation angles and transport currents in YBCO films using SrTiO_3 bicrystals [54]. They concluded that large angle grain boundaries in a-b planes (in-plane) degrade critical current densities of the superconducting films, and very weak superconducting coupling exist in these superconducting films. According to the results, sufficient critical currents could hardly be obtained if large-angle grain boundaries exist in the a-b plane of YBCO films. Critical current densities of YBCO films decrease drastically in the presence of even small magnetic fields, when weak links are present in YBCO films [54, 55]. Higher misorientations angles ($\geq \sim 10^\circ$) cause more reductions in J_c [56]. In order to achieve flexible long length YBCO coated conductors with high J_c of about 10^6 A/cm^2 (MA/cm^2) in liquid nitrogen (77 K) and in self magnetic fields, both in-plane and out-of-plane alignments need to be satisfied in YBCO grains. These alignments can be accomplished by epitaxial growth of YBCO films on biaxially textured oxide buffer layers over the

entire length of the conductors [8, 11]. Critical current densities approaching 3 MA/cm^2 have been reported for YBCO coated conductors [22].

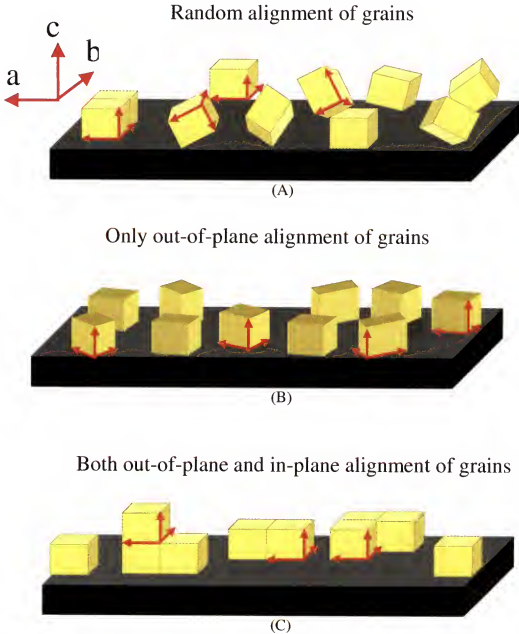


Figure 2.2. Schematic representations of alignments of grains. A) Random alignment. B) Only out of plane alignment. C) Both out of plane and in-plane alignments (biaxial texture).

2.3 Substrates

2.3.1 Polycrystalline Non-Textured Substrates

An extensive review of substrate selection for growth of high temperature superconducting thin films has been published by Phillips [57]. Silver was the first investigated substrate for YBCO coated conductors, because it is chemically compatible with YBCO [58-60]. However, because of its poor mechanical properties, high cost and large linear thermal expansion coefficients compared to YBCO, polycrystalline non-textured nickel based alloys became the choice of researchers for YBCO coated conductors' research. Mainly three different Ni alloys, Hastelloy C-276, Haynes 242 and Inconel 625, have been used as substrates, but Hastelloy C-276 (57% Ni, 16% Mo, 16% Cr, 5% Fe, 4% W, 0.56% Co, 1% Mn, 0.35% V, 0.08% Si, 0.01% C weight percent) is the most frequently used substrate. Biaxially textured buffer layers are grown on these substrates by ion beam assisted deposition or incline substrate deposition techniques.

2.3.2 Rolling Assisted Biaxially Textured Substrates (RABiTS™)

In this process, first polycrystalline face centered cubic (FCC) metal rods are cold rolled; after that the cold rolled metal tapes are heat treated for recrystallization at defined temperatures to form the biaxially textured structure. This process is a thermomechanical process, and very sharp biaxial texture is obtained from FCC metals like Cu and Ni. The heat treatment takes place either under vacuum or in reducing gas flow (4% H₂ – Ar) to prevent oxidation of the metal substrates. Then appropriate buffer layers are epitaxially grown on these substrates. These buffered metallic substrates are called rolling assisted biaxially textured substrates (RABiTS™) [8]. The biaxially textured substrates provide the underlying template for YBCO coated conductors, and they enable the

superconducting materials to have a high degree of grain alignment in all directions that is a necessary condition for high J_c . The schematic drawing of RABiTS™ is seen in Figure 2.3.

Biaxial texture formation in FCC metals by thermomechanical process has been known more than 40 years [56, 61-64]; however, the use of biaxially textured metal tapes as substrates for fabrication of YBCO coated conductors using buffer layers have been developed by Goyal et al. in the Oak Ridge National Laboratory [8].

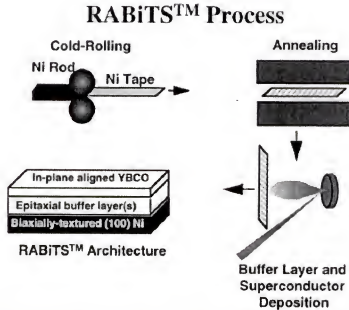


Figure 2.3. Schematic representation of the RABiTS™ process for fabrication of HTS coated conductors [25].

2.3.2.1 Biaxial texture formation in pure FCC metals

Plastic deformation (or mechanical process) from wire drawing or sheet rolling processes generates preferred orientations, which are called deformation textures in the metallic materials due to the self induced crystal rotation of each grain. In the rolling process each grain undergoes slip and rotation in a complex way depending upon applied forces. Development of textures is strongly influenced by the deformation mode, alloy

composition, stacking fault energy, strain rate, temperature, grain size, prior heat treatment and deformation history etc. Especially stacking fault energy is a fundamental parameter that controls the type of deformation texture. Metal or alloys with medium to high stacking faults energy ($\gamma > 100 \text{ mJ/m}^2$) develop a deformation texture which promote cube texture during recrystallization [65]. The rolling speed and thickness reduction per pass are important parameters for the plastic deformation process. Effect of rolling speed on the texture development is not dominating, however, higher rolling speeds are desirable for economical purposes. On the other hand thickness reduction per pass and total size reductions are important for texture developments. Generally, less than 30% reduction per pass and about 95% total size reduction are desirable for biaxial texture formation in the final product. Initially, randomly oriented starting materials are required for biaxial texture. Therefore, some heat treatment and deformations may be designed to give a random texture in the starting materials prior to rolling process [56]. When a plastically deformed metal is heat treated, recrystallization, grain growth and preferred alignments take place. The obtained alignment of grains (texture) after heat treatment, which is called recrystallization texture or annealing texture, depends on the annealing conditions like time and temperature, [56, 66]. Generally, textures of materials are described by notations of crystallographic planes and their directions like $(hkl)[uvw]$. (hkl) represents the plane and $[uvw]$ represents the direction. For example cube texture is described by $(100)[001]$ notation. The notation symbolizes that each grain is oriented with its (100) planes nearly parallel to the sheet surface and the $[001]$ direction in these planes nearly parallel to the rolling direction, and recrystallization texture is seen in many FCC metals and alloys under suitable conditions [56, 66].

Researchers from all over the world have been trying to fabricate long lengths of biaxially textured silver strips because of chemical compatibility of silver with YBCO. However, due to the unique deformation characteristics of silver, full-width-at-half maximum value of in-plane texture of silver tape within the desired angle of 10° or less has not been succeeded yet. Moreover, other disadvantages, which were mentioned before like lack of mechanical strength, cost of silver and big thermal expansion coefficient made the usage of silver substrates unfavorable in YBCO coated conductors. On the other hand, sharp biaxial texture in nickel can easily be achieved, and nickel is cheaper than silver and has better mechanical properties compared to silver. In terms of thermal expansion, Ni has the closest thermal expansion coefficient to YBCO, and Ni doesn't severely oxidize at high deposition temperatures compared to other metals like copper. Therefore, pure nickel or nickel alloys with minor atomic percentage alloying elements used as substrates for fabrication of coated conductors.

2.3.2.2 Biaxially textured Ni alloys

Generally 50-125 μm thick substrates have been used for fabrication of YBCO coated conductors, and 50 μm thick substrates are desired to maximize engineering critical current densities (J_c). High purity Ni tapes (99.99%) with 50 μm thicknesses are mechanically weak and can be bend easily after heat treatment compared to Ni alloys. Especially, handling of these tapes becomes very crucial in a long length fabrication process, because significant defects such as bends and kinks could be introduced in the soft, flexible Ni tapes [22]. Hence, nickel alloy substrates with low atomic percentage alloying elements become necessary for certain applications of YBCO coated conductors. Therefore some small amounts of alloying elements are added into pure nickel to increase

tensile strength and to change magnetic properties. For example, the average of several tests on Ni-3at.%W-1.7at.%Fe (magnetic) samples gave yield strength (YS) of 143 and 154 MPa at 0.02% and 0.2% strain, respectively. Similar tests for 99.99% pure Ni showed YS of 40 and 58 MPa at 0.02% and 0.2% strain, respectively. In these experiments it was showed that mechanical strength of the particular Ni alloy was about three times higher than that of pure Ni, even when both samples were prepared with same method using powder metallurgy and having similar grain sizes, thickness and annealing conditions. The mechanism of mechanical strength improvement in this example is believed to be solid solution strengthening [22]. Moreover, some applications like high field superconducting magnet and alternating current (AC) applications of YBCO coated conductors require non-magnetic substrates. Since pure nickel is known as a ferromagnetic material and ferromagnetic properties of pure Ni complicates design of superconducting magnets. Use of coated conductors with magnetic substrate in AC applications runs the risk of increased energy loss, due to hysteretic loss in the magnetic material [67]. Hence, it is clearly desirable to develop non-magnetic substrates (Ni alloys) with improved mechanical strength for YBCO coated conductors. Increasing the percentage of alloying elements in pure Ni greatly affect surface characteristics and texture. Basically, high percentage of alloying elements increase surface roughness of the substrate depending upon the percentage of alloying element, and also higher annealing temperature and longer time become necessary to obtain required cube texture. Obtaining sharp biaxial texture become difficult with increasing amount of alloying elements. Ni alloys such as Ni-13 at.%Cr and Ni-9 at.%V are paramagnetic at 77 K, and have similar surface characteristics and sharp biaxial texture [22, 68]. It is hard to obtain cube texture

in Ni alloys, when the amount of alloying elements exceeds the certain amount. As it was mentioned before, Hastelloy and Inconel are polycrystalline nickel alloys with high amount of alloying elements, and cube texture cannot be formed, and these substrates require additional surface modification like chemical polishing to have smooth surfaces.

Effects of surface roughness of biaxially textured Ni tapes were investigated on texture quality of deposited buffer layers [69]. Basically, there are two sources of surface roughness of Ni tapes. First, rolling traces, which can be minimized or avoided by using high quality rollers. Second one is called thermal etching or grain boundary grooving. Grain boundary grooves, which formed during the annealing process is an inevitable outcome of the recrystallization process. Grain boundary grooves can be clearly seen in sol-gel [70] and rf-magnetron sputtering [71] deposited buffer layers, because the buffer layers follow surface morphology of the nickel substrates. It has been shown that the grain boundary grooves can be transferred into YBCO films through buffer layer structures, and they may significantly disrupt epitaxy of YBCO at that region because YBCO films tend to align the c-axis perpendicular to the growing surface. The disturbed regions in YBCO films may reduce the J_c of YBCO coated conductors [25, 72].

Grain boundary groove formation in metals [72-75] and ceramic [76, 77] was investigated, and found that grooves in metals may occur by evaporation–condensation or surface diffusion process. The processing conditions such as annealing temperature determine the profile of the grooves [72]. Effects of alloying elements on grain boundary grooving are different for Ni. For example, 10 wt%Cr in Ni increase the depth of grooves because, high annealing temperatures are required in order to obtain cube texture [72], however, addition of 5 at%W in Ni reduces the susceptibility of nickel substrate against

grain boundary grooving up to 900 °C and very sharp biaxial texture FWHM = 6.6 - 7.0° can be obtained from the Ni-W alloy [64].

2.4 Buffer Layers

It has been observed that direct deposition of YBCO films on pure Ni or Ni alloys degrades superconducting properties of YBCO, because of Ni ion diffusion into YBCO film, NiO formation during YBCO process around 700 °C, and lattice mismatch between Ni and YBCO [78]. Therefore fabrication of YBCO coated conductor on flexible metallic substrates can only be achieved by having intermediate oxide layer(s) such as CeO₂, YSZ, Gd₂O₃, SrRuO₃ etc., between Ni substrate and YBCO layers [5]. These biaxially textured oxide layers, which are called buffer layers, are deposited to provide a chemical and diffusion barrier between the nickel and the superconductor while maintaining the same texture on the bare nickel substrates without any further surface treatment such as polishing [41]. The functions of the buffer layers are the following:

- i) to prevent diffusion of metal ions into YBCO
- ii) to prevent any chemical reaction between the substrate and YBCO
- iii) to retard oxidation of metallic substrate during YBCO processing at high temperature and in the presence of oxygen
- iv) to reduce lattice mismatch between Ni and YBCO

Several multilayered buffer layers structures were fabricated and satisfied all of these functions, and the most commonly used buffer layers structures are Hastelloy/YSZ/CeO₂, and Ni/CeO₂/ YSZ/CeO₂ [79]. YSZ is known as one of the best diffusion protection layers for YBCO coated conductors [78]. Several groups have been demonstrated YBCO films with J_c higher than 10⁶ A/cm² using YSZ intermediate layers

on silicon wafers [80]. However, critical current densities' of YBCO films deposited under similar conditions on YSZ buffer layers with non-textured Ni alloys were two to three orders of magnitude lower. The reason for this low J_c is texture quality of YSZ layers. Highly textured YSZ layers can be grown on single crystal Si substrates, whereas randomly oriented or only out-of-plane oriented YSZ films can be grown on non-textured Ni alloys [78]. Growth of only out-of-plane (c-axis) oriented YBCO films on randomly oriented or c-axis oriented YSZ layers are relatively easy and had been demonstrated [21, 55, 81]. However, their J_c were around 10^3 - 10^4 A/cm², and J_c degraded severely in magnetic fields, indicative of lack of in-plane texture. High angle grain boundaries become present when YBCO films deposited on only c-axis or randomly oriented YSZ buffer layers, because in-plane alignment doesn't form in YBCO, and YBCO grains are weakly coupled. As a result high angle grain boundaries in a-b planes of YBCO cause low critical current [55]. The challenge was how to obtain both in-plane and out-of-plane alignment in YSZ and YBCO layer. In order to control in-plane texture of YBCO films, Iijima et al. attempted to grow both in-plane and out-of-plane textured YSZ films on polycrystalline Ni alloys. However, it is difficult to grow in-plane textured YSZ films on polycrystalline substrates by conventional methods such as PLD, sputtering or MOCVD etc. Therefore, they used complex and expensive IBAD technique for YSZ processing, and succeeded to discover growth conditions of both in-plane and out-of plane textured (biaxial textured) YSZ films on non-textured Ni alloys. Subsequently, biaxially textured YBCO were deposited on the YSZ films by PLD [21].

Epitaxially grown oxide layers like CeO₂, YSZ, Y₂O₃, Eu₂O₃, Gd₂O₃, Yb₂O₃, SrTiO₃, on biaxially textured substrates have been investigated as buffer layers [82-84].

The most common buffer layer structure is Ni/CeO₂ or Y₂O₃/YSZ/CeO₂ [22, 25]. Since direct deposition of YSZ layers on biaxially textured substrates showed cracks in the microstructure of YSZ and in-plane texture of YSZ was high, CeO₂, Y₂O₃ or Gd₂O₃ buffer layers, which are called seed layers are deposited on bare Ni substrates. Their functions are to become template layer to grow crack free and highly textured YSZ thin films. Biaxially textured YSZ layers are deposited on the seed layers as diffusion barriers. Finally CeO₂, Y₂O₃, Gd₂O₃ buffer layers or engineered oxide thin films (Eu_{1-x}Yb_x)₂O₃ [85] as 100% lattice match with YBCO are deposited as cap layers. Since deposition of YBCO on YSZ buffer layers shows some reactions between YBCO and YSZ, especially when e-beam deposition technique is used for YBCO deposition, a cap buffer layer is necessary between YSZ and YBCO layers. Moreover, these cap layers are deposited to reduce lattice mismatch between YSZ and YBCO. High lattice mismatch between YSZ and YBCO cause poor in-plane texture in the YBCO layers.

The rolling-assisted biaxially textured substrates (RABiTS™) approach is one of the important leading technology for fabrication of coated conductors [8], and YBCO coated conductors with high critical current densities have been demonstrated with RABiTS™ substrates [22]. Moreover, the RABiTS™ approach is simple, well-established, and industrially scaleable processes. It eliminates slow deposition rate step of buffer layers in IBAD process. These special substrates enable the high-temperature superconducting wires to be used in power transmission cables, transformers, current limiters, motors, generators and many new industrial and commercial applications. It is difficult and complicated to scale-up IBAD process because of very low deposition rate.

2.4.1 Conducting Buffer Layers

Most of the buffer layers, which were investigated for fabrication of YBCO coated conductors, are insulating oxide layers. However, the superconducting YBCO layers have to be coupled with a good thermal and electric conducting layer for stable operation of the end product. In case of a local failure in the superconducting layer, electrically conducting buffer layers share the large current flow and help to remove generated heat in the YBCO film. Electrical coupling of YBCO layers can be done in two ways. First, if the substrate is pure Ni which has very low electrical resistivity, biaxially textured and conducting buffer layers like, SrRuO₃ (SRO) [86-88], LaNiO₃ (LNO) [86, 87], (LaSr)TiO₃ [89], (LaSr)MnO₃ [71] and In₂O₃ [90] are preferred to establish appropriate electrical contact between Ni and YBCO thin films. Second, if the substrate is Ni alloys, Ag layer deposition is preferred at the top of the YBCO films, because of high resistivity of Ni alloys. Generally, Ag layer is deposited by sputtering technique at low temperatures, and both ways satisfy electrical stability of YBCO coated conductors. YBCO films on LNO/Ni showed considerably suppressed T_c and J_c because of Ni contamination from LNO. Since biaxial textured growth of SRO on Ni has not been accomplished yet, SRO was grown on LNO/Ni. Very sharp biaxial texture was obtained from SRO/LNO/Ni, and J_c of YBCO grown on the structure was 1.2 MA/cm² which is comparable to J_c of YBCO on CeO₂/YSZ/CeO₂ buffer layer structure [86, 87]. YBCO films were deposited on highly textured La_{0.7}Sr_{0.3}MnO₃ (LSMO). However the J_c of this YBCO coated conductor was lower compared to the J_c of YBCO films on LaMnO₃ buffer layers due to Sr contamination [71].

2.4.2. Effect of Sulfur Structure on Growth of Biaxially Textured Buffer Layers

Nucleation and epitaxial growth of seed layers on biaxially textured Ni tapes was investigated by Cantoni et al.[91, 92]. It is very important to deposit in kilometer length oxide seed layers with uniform texture, because texture quality of seed layers control texture quality of the next deposited layers. Growth process of seed layers involves interaction of two different surfaces (metal-oxide interface) with different chemical and electronic properties. It was shown that lattice match is not enough to obtain epitaxial growth of seed layers like YSZ and CeO₂ on biaxially textured Ni substrates, and presence of sulfur superstructure on the Ni surface play a key role for epitaxial growth of seed layers [91]. Growths of YSZ films on biaxially textured Ni substrate with and without sulfur superstructure were investigated, and the films were deposited under the same conditions by PLD. Only (111) oriented YSZ films, which are not desirable for YBCO coated conductors were obtained when Ni substrates without sulfur superstructure was used, however only (200) oriented YSZ films obtained when Ni tape with sulfur superstructure was used. This experiment clearly showed effects of sulfur superstructure on textured growth of seed layers. Totally, two different seed layer grain alignment were obtained with and without sulfur superstructure. 100% sulfur superstructure covered Ni tapes could be obtained by annealing of Ni tapes under H₂S-Ar gas mixture [91].

2.5 YBa₂Cu₃O_{7-δ} (YBCO) Films

YBa₂Cu₃O_{7-δ} was the first discovered HTS material with a critical temperature (T_c ~ 92 K) above liquid nitrogen's temperature (77 K). The structure of YBa₂Cu₃O_{7-δ} is classified as perovskite type. There is no special scientific meaning of perovskite, it is just a label for a family of structures whose generic class is represented by SrTiO₃.

Perovskite is a name of a small village in Russia where over the years many oxides with similar structures were found [93].

$\text{YBa}_2\text{Cu}_3\text{O}_6$ has a tetragonal perovskite structure tripled along the c-axis.

Dimensions of the unit cell are approximately 4 \AA and 12 \AA in the a-b and c axis directions, respectively. In the unit cell an yttrium ion in the center and barium ions above and below the copper-oxygen planes. The structure consists of a sequence of oxide layers perpendicular to the c-axis as follows:

- 1) Cu-O layer has two oxygen vacancies as compared with the fully oxidized $\text{YBa}_2\text{Cu}_3\text{O}_7$. Cu(1) site in this oxygen layer has coordination 4 and is surrounded by 4 oxygen ions. In $\text{YBa}_2\text{Cu}_3\text{O}_7$, this is the plane made by the CuO chains.
- 2) Ba-O layer
- 3) Cu-O layer in which Cu(2) has a coordination number 5 and is surrounded by 5 oxygen ions which form a polyhedra. This plane is called CuO_2 plane
- 4) Yttrium layer which has 4 oxygen vacancies as compared with the fully oxidized $\text{YBa}_2\text{Cu}_3\text{O}_7$. The rest of the structure is symmetric with respect to yttrium ion [93].

Copper is found in two different sites: Cu(1) within CuO_4 (squares) and Cu(2) within CuO_5 (a square-based pyramid). The separation of yttrium ions gives a two-dimensional characteristic to the structure [93]. In all of the high temperature cuprate superconductors, charge carriers play a crucial role to determine transport properties of superconductors. The transport properties of YBCO can be varied from insulating to metallic and superconducting as other cuprate superconductors. For example, $\text{YBa}_2\text{Cu}_3\text{O}_6$ (tetragonal) is an insulator, and it becomes a metallic conductor and superconductor below the critical temperature when it is doped with charge carriers (holes). The doping

is achieved by increasing the oxygen content in the formula, $\text{YBa}_2\text{Cu}_3\text{O}_{6+x}$, and it eventually reaches the $\text{YBa}_2\text{Cu}_3\text{O}_7$ composition in which there are no oxygen vacancies. Additional oxygen atoms form CuO chains, and these oxygen atoms attract electrons from the CuO_2 planes, which therefore become metallic. Critical temperatures of the compounds also change depending upon oxygen content. The maximum T_c is reached for $x \sim 0.93$ ($T_c = 94$ K), however, T_c is 92 K, when x is equal to 1. The optimally doped compound, $\text{YBa}_2\text{Cu}_3\text{O}_{6.9}$, is usually referred to as YBCO or Y-123. YBCO has an orthorhombic unit cell with $a = 3.82 \text{ \AA}$, $b = 3.88 \text{ \AA}$, and $c = 11.63 \text{ \AA}$ lattice parameters [93].

2.6 Fabrication of YBCO Coated Conductors by Vacuum Deposition Approaches

Vacuum thin film deposition techniques have been used for fabrication of YBCO coated conductors. In these methods the phase of a depositing material is formed, while deposition is taking place on a heated substrate. Many in-situ thin film deposition techniques investigated the biaxial textured growth of buffer layers and YBCO films on metallic substrates. In-situ deposition techniques include physical vapor deposition (PVD) methods, such as pulsed laser deposition (PLD), sputtering techniques including ion beam assisted sputtering deposition (IBAD) and chemical vapor depositions techniques (CVD) like metallorganic chemical deposition (MOCVD) have been used for fabrication of long length YBCO coated conductors. Fundamentals and details of these techniques can be found in the following references [94, 95]. All these thin film deposition techniques were originally developed for coating of short length samples. Therefore, deposition chambers of the techniques needed to be redesigned for deposition of long length samples. This was accomplished by adding a reel-to-reel deposition

apparatus to the conventional systems. A conductively heated roller heats the metallic substrate and drives the tape with a stepper motor. The moving substrate is heated around 700 – 800 °C. As an additional change rotating and translating target is used to uniformly remove target material during extended coating runs [42].

2.6.1 Buffer Layer Deposition Techniques

Choice of thin film growth techniques for deposition of buffer layers depends on the types of substrates. Biaxially textured buffer layers can only be grown on non-textured metal substrates by IBAD [21] or ISD [47] techniques. Since IBAD and ISD techniques are relatively new, brief background information will be given in the following sections. On the other hand, the majority of the vacuum thin film growth techniques can be used for the deposition of biaxially textured buffer layers on biaxially textured Ni or Ni alloys. Several biaxially textured buffer layers were deposited by electron beam evaporation [96-99], sputtering [69, 82, 100], PLD [88, 101, 102], CVD [103], and MOCVD [104] techniques. For example, Y_2O_3 , Yb_2O_3 , Gd_2O_3 buffer layers were grown on textured Ni substrates by e-beam evaporation technique [98]. After the deposition chamber was evacuated to 1×10^{-6} torr at room temperature a gas mixture of 4% H_2 and 96% Ar was introduced into the chamber to prevent NiO formation during the deposition. The background H_2O pressure was around 1×10^{-5} torr. The H_2O pressure in the chamber was sufficient to oxidize the films to form stoichiometric RE_2O_3 , and O_2 partial pressure was 10^{-8} torr during deposition [98].

2.6.1.1 Ion beam assisted deposition

In the IBAD process, rolled and polished nickel alloys generally Hastelloy is used as substrate, and buffer layers are deposited by ion beam assistance. An ion beam or a

dual ion beam is utilized to form in-plane alignment in the depositing buffer layers. After that YBCO films are deposited by PLD. Schematic drawing of IBAD process is seen in Figure 2.4. There are two models to explain biaxial texture development with ion beam assisted deposition [105]. The first model explains it with ion channeling. Ions that travel along the crystallographic planes interact with and damage the planes, and they lose less energy while they are interacting with the planes, which have large interplanar (d) spacing. The planes perpendicular to the ion beam get more disordered by the beam and they do not grow, planes parallel to the ion beam with large d are least disordered and more stable. Thus grains of this orientation grow at the expense of the others. The second model explains the texture formation with dependence of sputtering yield on grain orientations [106, 107]. Like the first model grains with different orientations have different sputtering yield, and reduced sputtering yield is obtained from grains with more open planes to the ion beam. Therefore these grains grow preferentially. Both in-plane and out-of-plane texture of thin films is strongly dependent on ion beam incident angle. Iijima et al. used a dual ion sputtering technique to grow YSZ thin film on Hastelloy substrate with an Ar ion sputtering source directed to the YSZ target and the second Ar + O mixture beam directed to the Hastelloy, and they successfully deposited biaxially textured YSZ films [21]. The YSZ film deposition rate was estimated to be 0.18 $\mu\text{m/h}$, and the film thickness was 0.3 μm . In-plane misorientations were measured to be $>30^\circ$ for optimum incident ion angle. Subsequently, they successfully deposited biaxially textured YBCO films [21]. J_c of the film were $2.5 \times 10^5 \text{ A/cm}^2$ and $2.2 \times 10^4 \text{ A/cm}^2$ at 77 K for self magnetic field and 8.0 T (magnetic field perpendicular to c axis), respectively. A new method to prevent intergranular weak links has been developed for potential

applications using practical polycrystalline substrates. FWHM values of in- plane and out-of-plane of YSZ buffer layers were about 30° and 5.3° , respectively [5, 21, 108].

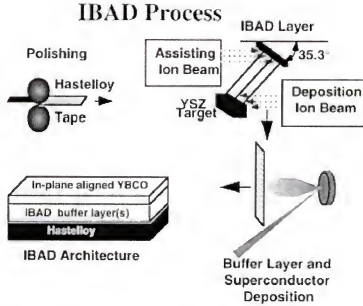


Figure 2.4. Schematic representation of the IBAD process for fabrication of HTS coated conductors [25].

Significant improvements followed these J_c enhancements, and Reade et al. demonstrated highly textured growth of YSZ layers on polycrystalline Ni alloys by ion-assisted pulsed laser deposition. YBCO films with 6×10^5 A/cm² and 8×10^4 A/cm² for 0 T and 0.4 T, respectively, had been grown on these YSZ layers [78]. In-plane texture of YSZ buffer layers has been improved by optimizing IBAD processing parameters. The FWHM value of in-plane texture of YSZ is obtained between 10° - 12° . Other long length biaxially textured buffer layers such as about 113 cm MgO and 60 m Gd₂Zr₂O₇ have been deposited by IBAD on Hastelloy substrates [109]. The average FWHM of in-plane texture of 113 cm MgO buffer layer was 11° . The best 25 cm section of the MgO with an average FWHM value of 9° was selected for subsequent YBCO deposition, and the J_c was around 1 MA/cm². The average FWHM of in-plane texture of continuous and

uniformly deposited $\text{Gd}_2\text{Zr}_2\text{O}_7$ films was $10^\circ - 12^\circ$ in the 15 m length and of $16^\circ - 18^\circ$ in the 60 m length, at a coating rate of 1.0 m/h [109]. IBAD MgO offers great economic advantage in the commercial production of YBCO coated conductor compare with IBAD YSZ. Because IBAD MgO requires only ~ 10 nm thickness to develop a texture structure, however, IBAD YSZ require about $1\text{ }\mu\text{m}$ thickness to develop same textured structure. When the required thickness issue is translated to the process, IBAD MgO is 100 times faster than IBAD YSZ [110]. In an optimized sample, I_c of 140 A and J_c of 1.2 MA/cm^2 were obtained from 8 cm YBCO coated conductor that $\text{Gd}_2\text{Zr}_2\text{O}_7$ buffer layer was deposited by IBAD. Continuous processing of YBCO films were carried out by pulsed laser deposition on long IBAD template tapes at a tape speed of 1.0 m/h. The I_c and J_c were achieved 50.0 A and J_c of 0.42 MA/cm^2 , respectively, from a 9.6 m YBCO coated conductor. The FWHM value of in-plane texture of YBCO film was 9° . Furthermore 1.0 MA/cm^2 were obtained from an 8 cm YBCO film. The FWHM value of in-plane texture of YBCO film was 8° with a 4.0 m/h YBCO coating speed [109].

2.6.1.2 Inclined substrate deposition (ISD)

Inclined Substrate Deposition (ISD) is a specialized technique, which is used to deposit biaxially textured buffer layers such as MgO and YSZ on non-textured metallic substrates like Hastelloy C-276 [47]. Since high quality biaxially textured buffer layers can be deposited on the poly crystalline substrates by ISD without the assistance of an ion beam, this method is especially attractive when high mechanical strength and non-magnetic polycrystalline substrates are chosen for fabrication of YBCO coated conductors. In this technique a polycrystalline metallic substrate is held at an angle to the direction of the plume of an e-beam evaporation system, and deposition takes place on

the inclined substrates. The ISD process allows high deposition rate compared to IBAD. Deposition rates of oxide layers can be selected between 20 and 200 Å/sec., and deposition can be done at room temperature. Moreover, the ISD process is reliable and a simple process. It is relatively a new technique and offers the potential to produce high quality biaxially textured buffer layers on non-textured substrates [47, 111-114]. The MgO, YSZ and CeO₂ thin films were deposited on non-textured Ni substrates by ISD technique [113, 115, 116]. So far good in-plane and out of plane texture were only obtained from MgO buffer layers. FWHM values of in-plane and out of-plane texture of MgO buffer layers were 9.2° and 5.4°, respectively. YBCO films were subsequently deposited by pulsed laser deposition on these ISD-MgO buffer layers, and 2×10^5 A/cm² critical current density was obtained from 0.5 – 1 µm thick, 0.5 cm wide, and 1 cm long sample [113].

2.6.2 YBCO Deposition

YBCO thin films are the most studied superconducting materials among HTS compounds. High quality YBCO films, which J_c 's exceeding 10^6 A/cm², have been grown on biaxially textured buffer layers on flexible metallic substrates. The superconducting properties of YBCO are sensitive to oxygen content in the formula, and in the ideal case it should be close to 7. Almost every in-situ thin film growth technique was tried for deposition of biaxially textured YBCO films since the discovery of YBCO. Generally, in-situ films grow in a more or less layer-by-layer manner. Surface diffusion takes place and deposited atoms and molecules migrate to the equilibrium lattice sites [117]. Surface smoothness and texture quality define the J_c of the YBCO films. Generally almost featureless and sharp textured YBCO films are necessary for high J_c . Especially

in-situ thin film growth techniques like electron beam evaporation [118, 119], sputtering [120, 121], PLD [109, 122], CVD [123, 124] and MOCVD [14, 125] have been exploited to grow epitaxial YBCO films on biaxially textured buffer layers. Among these techniques, pulsed laser deposition is the most commonly used technique for YBCO deposition, because the deposition rates are fast, and biaxially textured films with high J_c have been obtained up to 2 μm [105]. Typical YBCO deposition rates are ~ 0.5 nm/s. Deposition of YBCO films with high J_c was first demonstrated on single crystal substrates like SrTiO_3 , LaAlO_3 , etc [126-128], then YBCO films with high J_c were deposited on buffered metallic substrates [21]. Extremely high quality YBCO films have been deposited using in-situ deposition techniques, but these growth techniques have a number of disadvantages. The growth apparatus are complex and thin film deposition rates are low.

1 MA/cm^2 level was exceeded in the Los Alamos National Laboratory (1.3×10^6 A/cm^2) by careful control of processing variables and deposition of a second buffer layer, CeO_2 , on IBAD YSZ buffer layers in 1995. CeO_2 has better lattice match with YBCO and promote fewer high angle grain boundaries. The thickness of the YBCO was above 1 μm and length of the conductor was around 1 cm. Iijima et al. also demonstrated more than 1 MA/cm^2 J_c in the PLD deposited YBCO on IBAD YSZ in 1996 [129], and using RABiTSTM approach Goyal et al. obtained J_c 's exceeding 1 MA/cm^2 in 1996 [8]. 1 μm thick YBCO layers were deposited on a 13 cm long moving polished and buffered tape in Intermagnetics General Corporation (IGC-SuperPower). The average FWHM value of in-plane texture of the buffer layer and YBCO deposited on moving metal substrates are 20° and 15° , respectively. The average J_c over the 13 cm long tape was 0.5×10^6 A/cm^2 . The

J_c value over the best 3 cm exceeded $1 \times 10^6 \text{ A/cm}^2$ [130]. Not much progress has been accomplished in terms of fabrication of YBCO coated conductors longer than 1 meter with J_c of 1 MA/cm^2 critical current density since 1995. Summary of the additional results of YBCO coated conductors using IBAD YSZ can be seen in ref [49, 105].

2.6.2.1 Grain boundary issues in YBCO thin films

The most important property of YBCO coated conductors is to have high J_c in high magnetic fields. But existence of high angle grain boundaries in YBCO layers is the main hindrance to have high J_c in YBCO coated conductors. Therefore a lot of work has been done to understand effects of grain boundaries in high temperature superconductors. Hilgenkamp and Mannhart reviewed grain boundary issues of HTS materials in their recent paper by citing 659 papers [131]. So far J_c 2-5 MA/cm^2 has been obtained from high quality biaxially textured YBCO films, and effect of external magnetic field on reduction of J_c was investigated by several researchers [22, 48, 129, 132]. To solve the detrimental effect of grain boundaries on J_c of YBCO coated conductors a three-fold strategy have been proposed [133]:

- i) Grain alignment
- ii) Grain boundary doping
- iii) Maximize the effective grain boundary area

The detrimental effects of high angle grain boundaries on J_c [134], and the importance of grain alignment (biaxial texture) [54] was clearly established more than a decade ago. Importance of biaxial texture has already been discussed in the early sections of this chapter. Now grain boundary doping and maximization of the effective grain boundary area will be discussed here. High critical current densities (10^6 A/cm^2) are

obtained by deposition of biaxially textured YBCO films in short samples, and the minimum FWHM values of in-plane and out-of-plane textures of YBCO films were around 5° - 7° . Since less than 5° alignment has not been demonstrated yet, improvements in J_c are limited with grain orientations. Moreover, grain orientation itself might not be good enough to improve J_c and performance of YBCO coated conductors in magnetic fields. Because grain boundaries have different electronic structures, and depletion of charge carriers in YBCO grain boundaries have been shown both experimentally and theoretically [135]. This depletion leads to weak link between grains, and limits critical currents in superconductors. Recently improved grain boundaries have been showed in Ca-doped YBCO grain boundaries, and the effect of Ca doping has been explained by increasing charge carriers (holes) concentration in grain boundaries [135, 136]. In order to preferentially dope grain boundaries, Ca diffusion in the bulk as well as along the grain boundaries was studied. Ca diffusion coefficients have been established in YBCO bulk and PLD thin films, and it was found that the Ca diffusion coefficient in the epitaxial PLD films is about 20 times lower than in the bulk pellet. J_c of an epitaxial YBCO film was increased by a factor of 2 at 40 K but not in 77 K [136-138]. However, Hammerl et al. reported J_c of 6 MA/cm² in Ca doped YBCO coated conductors [139]. On the other hand, reduction in T_c was reported in Ca over doped YBCO films [140].

The third strategy, which is optimization of the microstructure to maximize the effective grain boundary area, was proposed by Mannhart [141], and Hammerl et al. [133] recently found ways to utilize large effective grain boundary area to enhance J_c of coated conductors that have two or three dimensional grain boundary networks. They demonstrated by theoretical approach using calculations based on Dijkstra's shortest path

algorithm. According to the approach, two coated conductors may be placed on top of each other such that the I_c of the structure exceeds the sum of the I_c of the individual coated conductors. Large I_c is achieved by establishing an extended superconducting contact between the two superconducting surfaces. Even though no experimental results have been published yet about the third strategy, combination of the three approached could be the solution to commercialize long length YBCO coated conductors.

2.6.2.2 Thickness issues in YBCO thin films

The relationship between YBCO film thickness and the J_c of the coated conductors was studied to understand the limits of current carrying capacity of YBCO coated conductors [24, 142]. The logical approach to have high I_c from a conductor is to increase YBCO films thickness. In fact it has been shown that I_c increases with increasing YBCO film thickness up to 1.5 μm then stay constant up to 3 μm and finally decreases up to 5 μm . To investigate this dilemma Foltyn et al. systematically studied the relationship between YBCO film thickness and the J_c of the coated conductors by thinning several films using ion mills [24]. It has been found that three things mainly cause the J_c reduction:

- 1) Deposition of thicker films takes longer time at temperature, thereby diffusion of metal ions contaminates the YBCO film at interface.
- 2) Increasing YBCO thickness cause additional crystalline orientations in the YBCO film like a - b axes orientations instead of c-axis orientation.
- 3) The film morphology becomes rougher and microstructure changes as YBCO thickness increases. Cross-sectional SEM investigation of 6 μm thick YBCO film

revealed that morphology of the bottom 1-2 μm of YBCO film is very dense and smooth, while above this thickness YBCO appears more disordered [24].

2.7 Chemical Solution Deposition (CDS) Approaches

2.7.1 Fundamentals

Chemical solution deposition of thin films is a non-vacuum thin film deposition approach, which is categorized under the ex-situ thin film deposition techniques. In the ex-situ thin film deposition techniques, first amorphous or individual polycrystalline phases are deposited at room temperature or very low temperatures, and subsequently the films are heat treated to form desired phase and crystallographic orientation [143].

Generally, fabrication of thin films by chemical solution deposition approach involves four steps:

- 1) Synthesis of the solution using metal organic precursors
- 2) Deposition of the solution by dip or spin coating technique
- 3) Low temperature heat treatment of the coating for drying (100 – 250 $^{\circ}\text{C}$), pyrolysis of organic species (300 – 450 $^{\circ}\text{C}$), and formation of an amorphous film (500 – 550 $^{\circ}\text{C}$);
- 4) Higher temperature heat treatment of the coating for densification and crystallization into desired oxide phase and crystallographic orientation (600 – 1200 $^{\circ}\text{C}$).

The final three steps are similar for most chemical solution deposition approaches, but the first step shows differences in the characteristics of precursor solution depending upon the solution route employed [144]. Typically metalloorganic compounds are used as starting precursors, which are dissolved in organic solvents and modifying ligands. Solubility and reactivity of starting precursors are always considered, while selection of precursors is made. The degree of homogeneity, reactivity, cation interaction, precursor

size, structure and shape of the solution precursor species depend on starting reagents. The solution route will also determine the range of mixing of the metal cations, formation of a three dimensional network or individual inorganic phases, carbon content of the film, temperature for pyrolysis of organic species, densification and crystallization behavior of the film. Solution chemistry variations like differences in precursor structure and solvent can have a significant impact on the processing behavior of the as-deposited film [144].

Chemical solution depositions of thin films have variety of approaches including sol-gel, chelate and metalloorganic decomposition processes that all have been employed in preparation of oxide thin films, bulk materials, and powders. More information about each approach will be given below.

Non-vacuum chemical solution deposition techniques have several advantages over vacuum techniques. They require considerably less equipment, and they are inexpensive and easy to scale-up. The solution process gives better homogeneity, high deposition rates, and composition control, because the precursors are mixed at atomic levels. Microstructure of the deposited film such as the pore volume, pore size, and surface area could be controlled using chemical solution deposition techniques by controlling chemistry of the solution. Substrates with various shapes can be easily coated with chemical solution dip coating techniques, and long length coatings can be accomplished by a reel-to-reel dip coating systems. Chemical solution deposition (CSD) methods have been utilized for deposition of long length buffer layers and YBCO.

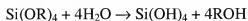
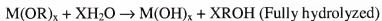
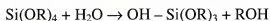
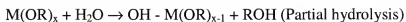
2.7.2 Sol-Gel Process

In sol-gel process, starting reagents are typically metal alkoxide compounds, $M(OR)_x$, where M is a metal and R is an alkyl group (CH_3 , C_2H_5), and 2-methoxyethanol

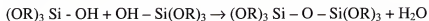
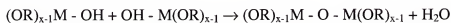
(CH₃-OCH₂CH₂OH) is the most extensively used solvent and reactant due to the ability to dissolve a variety of starting reagents. Since the reactivity of the reagents is high if alcohol exchange occurs or if modifying ligands are used, the structure of the species in the solution will be different than from starting compounds.

In sol-gel process some key reactions leading to the formation of polymeric species are hydrolysis and condensation of the alkoxide reagents, in which metal-oxygen-metal (M – O – M) bonds are formed when alkoxide precursors react with water. Two reactions are needed to form (M – O – M) network. In the first reaction a water molecule partially hydrolyzes the alkoxide molecule, and in the second reaction a partially hydrolyzed molecule reacts with another alkoxide molecule [145].

Hydrolysis: Reaction of metal alkoxide with water.



Condensation: Two partially hydrolyzed molecules can link together in a condensation reaction.



The process of polymerization is the continuation of condensation reaction and formation of larger molecules in the solution [146].

2.7.3 Chelate Process

In this solution synthesis approach like sol-gel process alkoxide compounds are

used as starting reagents, but these molecules are modified through reactions with other reagents which is called chelating ligands such as acetylacetone (acac, 2,4-pentanedione), or amine compounds. The primary reason for using chelating agents is to reduce the hydrolysis sensitivity of the alkoxide compounds and to make them usable in air. Although air and water insensitive solutions are produced with the chelating process, the initial stage of solution preparation process is usually carried out under the inert atmosphere conditions. Since molecular modifications of alkoxide compounds takes place, the structure and pyrolysis behavior of resulting species becomes different from the starting compound depending upon the used ligands such as acetate or acac. Viscosity of the solution is adjusted by adding alcohol or water.

Hydrolysis and condensation reactions also occur in the chelate process, and the reactions depend on solvent/chelating agent ratio. The key reaction is chelation of the metal alkoxide which can be illustrated here for acetic acid [144]:



Chelate process is relatively simple compare to sol-gel process. Distillation and refluxing strategies are not required in the process, and the process is very rapid, typically solution synthesis requires less than 1 hour. One drawback of the chelate process is that the chemical reactions in the precursor solution continue, and the characteristics of precursors change over time (weeks to months) and thereby degradation in film properties. Despite these disadvantages, a number of research groups have successfully fabricated oxide thin films with excellent electrical and microstructural properties [144].

2.7.4 MOD Solution Synthesis

Historically, in the metalloorganic decomposition (MOD) approach, large

carboxylate compounds such as 2-ethylhexanoate, neodecanoate, dimethoxy dinedecanoate, which are water insensitive reagents, have been used for processing of perovskite thin films. Commercially available precursors or in-house synthesized starting reagents can be used by dissolving these metalloorganic compounds in a common solvent, usually xylene, and precursor species in the solution retain a strong resemblance to the starting molecules. The use of non-interacting solvents makes it easy to characterize the solution because the solution simply consists of a mixture of the starting compounds.

One of the disadvantages of this process is crack formation during thin film processing because pyrolysis of large carboxylate compounds causes large weight loss and shrinkage. Therefore, proper thermal processing and solution concentration is required. Crack formation in thin films has been solved by Haertling's new solution preparation route. In this approach short chain and low reactivity carboxylate (e.g., acetate) and B-diketonate (e.g., acac) compounds are used as starting agents. The compounds are water insensitive and commercially available, therefore solution synthesis is straightforward for non-chemists. Since this is a low organic content in the precursor solutions, less weight loss and shrinkage occurs during pyrolysis of the films. As a result the crack formation in the films is minimized or avoided [144].

2.7.5 Thin Film Coatings

The basis of the coating process is the pyrolysis of precursor solutions into oxide layers. Precursor solutions are deposited on substrates by either dip coating or spin coating techniques. Generally small and flat substrates like single crystal wafers are coated with spin coating, however, irregular shape or large size objects and long length

wires or tapes are coated with dip coating. The microstructures of thin films depend on the size and extent of branching (or aggregation) of the solution species prior to the film deposition and condensation and evaporation rates during film deposition. Control of these factors enables tailoring the microstructure of the film [144, 146].

2.7.5.1 Dip coating

Generally dip coating process is divided into five stages: immersion, start up, deposition, drainage, and evaporation [146]. The substrate is dipped into the solution bath and withdrawn vertically at a constant speed in a dip coating technique. The fluid-substrate boundary layer splits in two. The inner layer moves upward with the substrate, while the outer layer is returned to the solution bath. Depending upon the solution's nature, evaporation starts at the deposition stage. The thickness of the deposited film is related to the position of the streamline dividing the upward and downward moving layers, withdrawal rate and viscosity of the solution. The film thickness increases with increasing viscosity, and decreases with slow withdrawal rate. Most of the solution returns back to the solution's bath with slower withdrawal rates. Physics of film formation was extensively reviewed by Brinker [146].

2.7.5.2 Spin coating

Spin coating is divided into four stages: deposition, spin-up, spin-off, and evaporation [147]. In the deposition stage the solution is placed on a substrate and excess of the liquid is dispensed on the surface. The liquid flows outward by centrifugal force in the spin-up stage, and then during the spin-off stage excess liquid flows to the perimeter and leaves as droplets. Finally evaporation takes place and it is the primary mechanism for the thinning of the film [146, 147]. Thin films with uniform thickness are obtained by

spin coating and this is the one of the most important advantages of this technique.

However, size and shape of the substrates are limited to be coated with this technique.

2.7.6 Chemical Solution Deposited Buffer Layers

Buffer layers such as CeO_2 [70], Gd_2O_3 [132, 148, 149], Yb_2O_3 [18], Eu_2O_3 [17], $\text{La}_2\text{Zr}_2\text{O}_7$ [150, 151], $(\text{EuYb})_2\text{O}_3$ [85] have been successfully deposited on biaxially textured Ni substrates by chemical solution deposition approach. When they were annealed between 1050 °C and 1160 °C for 10 minutes to 1 hour under the reducing gas atmosphere, biaxially textured structures have been obtained. However, both in-plane and out-of-plane textures of the chemical solution deposited buffer layers were $2^\circ - 4^\circ$ worse than that of buffer layers deposited by vacuum techniques. For example, FWHM of sol-gel and e-beam deposited Yb_2O_3 were 10.11° (in-plane), 9.89° (out-of-plane) [18] and 8.8° (in-plane), 6.4° (out-of-plane) [98], respectively. One meter length of Gd_2O_3 also deposited on a textured Ni alloy by sol-gel process [132]. The texture of the film was uniform along the 1-meter length, and the average FWHM values of in-plane and out-of-plane textures were 8.74° and 9.96° , respectively. These chemical solution deposited buffer layers were deposited as seed layers. Almost every scientist had a different recipe to prepare solutions of these buffer layers. But, generally sol-gel and chelating approaches were used for these buffer layers. More information about solution preparation and deposition process can be found in the original papers.

2.7.7 Chemical Solution Deposition of YBCO

Chemical solution deposition approach for deposition of YBCO films carry great potentials, because it is a fast, efficient and inexpensive process. Therefore, chemical solution deposition of YBCO thin films get attentions of the researchers all over the

world. YBCO solutions have been prepared by using different precursors like nitrates [152] and carboxylates [153], and deposited by either spin coating on single crystal substrates (LaAlO_3 , SrTiO_3 , YSZ) or dip coating on RABITSTM [154-156]. However, during decomposition of organics, barium reacts with organics and forms BaCO_3 which degrades superconducting properties of YBCO films [26]. Hence, precursor selection, solution preparation and pyrolysis play crucial role in the formation of YBCO. Successful chemical solution deposited YBCO films were reported by Gupta et al. [26] using Y, Ba, Cu trifluoroacetates (TFA) precursors, the process was named TFA or BaF_2 process. Carbon contamination was prevented using BaF_2 precursor instead of Ba metal or BaO , which are more sensitive to moisture and carbon contamination. On the other hand, BaF_2 is stable in air, and annealing of the stoichiometric precursor film at high temperature in oxygen and water vapor (wet atmosphere) promotes growth of biaxially textured YBCO films. A wet atmosphere is necessary for the decomposition of BaF_2 and complete removal of fluorine from the film during the high temperature annealing. By-product of the process is hydrofluoric acid (HF), which necessitates special handling and corrosion resistive equipments. To avoid HF evolution, different chemical solution routes have been tried. Shi et al. used yttrium trimethyl acetate, barium hydroxide, and copper trimethyl acetate powders, and dissolved them in a mixture of propionic acid and amine solvents. They only succeeded growth of out-of-plane oriented YBCO films on LAO substrates, and J_c was around 10^5 A/cm^2 [157].

High critical current density ($5 \times 10^6 \text{ A/cm}^2$ at 77 K) was obtained from 70 nm thick TFA YBCO films [158]. Dawley et al. have succeeded in depositing high quality 0.1 μm and 0.25 μm TFA-YBCO films on LaAlO_3 substrates with current densities 3.0

MA/cm² and 2.0 MA/cm², respectively [154]. YBCO films with TFA process were also grown on BABITSTM substrates, and J_c of 1.3 MA/cm² was obtained [155]. As buffer layers Nb doped SrTiO₃ was used, because water vapor of TFA-YBCO process react with YSZ and MgO. Takahashi et al. obtained J_c of 0.9 MA/cm² from TFA-YBCO on CeO₂(PLD)/Zr₂Gd₂O₇(IBAD)/Hastelloy tapes [159].

Always thick (~ 5 μm) and high J_c YBCO coated conductors are desired for power transmission applications. But, typically 0.1 μm thick high quality thin films can be coated per process from low viscosity solutions, which have high volume fractions of organics. As a result, the coating process has to be repeated 20 to 50 times in order to achieve the desired thickness, which is not an efficient way. Tailoring the solution concentration and processing parameters like withdrawal rate increase the films thickness, but some micro and macro cracks may be introduced in the film because of drying stresses. In recent years addition of high viscosity compounds such as diols, triols and high molecular weight polyvinylpyrrolidone to precursor solutions made it possible to deposit thick films of PbZrO₃ and BaTiO₃ with a single coating [154]. 0.25 μm thick YBCO films with 2×10^6 A/cm² at 77 K has been obtained using diol solution route [154]. More research is necessary for fabrication of high quality thick YBCO coated conductors by chemical solution deposition approach.

CHAPTER 3

EXPERIMENTAL PROCEDURES

This research consists of the preparation and characterization of the textured nickel substrates, the chemical solution deposition of textured CeO_2 and $(\text{Eu}_{1-x}\text{Yb}_x)_2\text{O}_3$ engineered thin films as buffer layers, and the microstructural characterization of these buffer layers.

3.1 Substrate Preparation

1 cm and 0.5 cm wide, 75 μm thick, high purity (99.99%) cold rolled nickel tapes were used as substrates for deposition of buffer layers. The cold rolled Ni substrates were kindly supplied by Hyper Tech Research, Inc. The Ni substrates were cleaned in ultrasonic bath with acetone, and were gently wrapped on a quartz tube prior to annealing process as seen in Figure 3.1. Then the Ni tapes were heat treated based on our published results [160] in an electric furnace under reducing gas flow (4% Hydrogen - 96% Argon) typically at 1050 $^{\circ}\text{C}$ for 30 minutes to obtain desired $[16]\langle 100 \rangle$ cube textured crystal structure.



Figure 3.1. The picture of the 0.5 cm wide Ni tape as wrapped on a quartz tube for annealing process.

Texture characterization of Ni substrate, which includes pole figures, omega and phi scans will be discussed later under the XRD characterization section. After preparing the biaxially textured Ni substrates, the next is preparation and deposition of precursor solution of CeO_2 and $(\text{Eu}_{1-u}\text{Yb}_u)_2\text{O}_3$ buffer layers.

3.2 Processing of CeO_2 Buffer Layers by Chemical Solution Deposition

Several perovskite and rare earth oxide thin films have been considered as candidate buffer layers for fabrications of YBCO coated conductors because of their chemical compatibility and close lattice match with YBCO. CeO_2 is one of the most preferred buffer layers for fabrication of coated conductors, especially it is used as a cap layer when an e-beam evaporation technique is used for YBCO processing and Yttrium Stabilized Zirconia (YSZ) is used as an intermediate diffusion barrier layer. Therefore, processing of CeO_2 buffer layers have been extensively studied using various vacuum deposition techniques. However, a non-vacuum process for preparation of CeO_2 buffer layer, which had not been undertaken until this study, is desired for fabrication of coated conductors to make coated conductors available and affordable for large scale applications.

Processing of CeO_2 buffer layer by non-vacuum chemical solution deposition technique mainly involves three steps, i) preparation of precursor solution, ii) thin film coating and iii) final heat treatment for formation of biaxially textured structure. Low angle grain boundaries and biaxially textured structure are needed in CeO_2 buffer layers to facilitate epitaxial growth of YBCO layers. High angle grain boundaries cause reduction of critical current densities of the coated conductors.

i) Preparation of precursor solution: The synthesis of precursor solution of CeO_2 buffer layers was prepared using cerium 2,4-pentanedionate $[\text{Ce}[\text{CH}_3\text{COCH}=\text{C}(\text{O}-)\text{CH}_3]_3 \cdot \text{XH}_2\text{O}$ (Alfa Aesar)], methanol $[\text{CH}_3\text{OH}$ (Fisher)], glacial acetic acid $[\text{CH}_3\text{CO}_2\text{H}$ (Fisher)], and acetyl acetone $[\text{CH}_3\text{COCH}_2\text{COCH}_3$ (Fisher)]. All chemicals were used as received and the solution preparation was carried out in argon gas in a glovebox. 0.787 g of cerium 2,4-pentandioante was dissolved in 15 ml of methanol and 2 ml of glacial acetic acid mixture. Then 1 ml of acetyl acetone was added into the solution as chelating agent. In order to improve wetting of the solution onto the Ni substrate, 0.5 ml triethanolamine $[(\text{HOCH}_2\text{CH}_2)_3\text{N}$, (Aldrich Chemical Company Inc.)] was added in the solution. The solution was stirred at about 60°C until complete dissolution, which took about 2 hours. After cerium 2, 4-pentanedionate dissolved, the resultant sols were clear and stable at room temperature. This was the reason that 2, 4-pentanedionate precursor was chosen to get a stable solution in air with a long life. Color of the solutions was reddish. Cation concentration of the solution was changed by addition of methanol, and different solution concentrations were tested like 0.025, 0.05, 0.1 and 0.15 M, but most of the time 0.1 M solution was used for buffer layer coatings because that gave better surface coverage and crack free thin films.

ii) Thin film coatings: The biaxially textured Ni tapes, which were 10 cm long and 1 cm wide, were used as substrates. The Ni substrates were gently cleaned with acetone before the deposition of Ce precursor solution. The substrate became so soft after annealing process that extra care was necessary during cleaning and coating process not to form bends and kinks. A reel-to-reel sol-gel dip coating system with an in line three zone furnace was used for deposition of the buffer layers. The picture of reel-to-reel dip

coating system is seen in Figure 3.2. Various withdrawal speeds were applied such as 0.25, 0.60, 1 and 1.5 cm/s. However, most of the time samples were withdrawn from the coating solution bath with a speed of 1.0 cm/s.



Figure 3.2. The reel-to-reel dip coating system with an in-line three zone furnace.

The temperature of the three zone furnace were set around 200, 450 and 550 °C, for zone 1, 2 and 3, respectively. The temperatures of the zones were selected according to the results of differential thermal analysis (DTA) of the xerogels of this solution. The gel films were dried at 200 °C, then organics were burnt at 400-500 °C and oxide formation occurred at higher temperatures. Dip coating process was repeated 1-3 times to

achieve the desired thickness. After each deposition process, the buffer layers went through the heat treatment process for biaxial texture formation.

iii) Final heat treatment: After volatile organics were burned out from the film in three zone furnace, the samples were transferred to a tube furnace and annealed under 4% H_2 -Ar gas flow. A series of experiments at various annealing temperatures and time ranging from 950 °C to 1170 °C, and from 10 minutes to 1hour, respectively, in flowing forming gas atmosphere (5 cc/min.) were made to determine the optimum processing conditions of CeO_2 buffer layers on Ni substrates. 900 °C/h heating rate was used for annealing process. Highly textured CeO_2 buffer layers were obtained by using the 1150 °C and 10 minutes annealing process.

3.3 Engineered Buffer Layers for 100% Lattice Match with YBCO

One of the most important qualities of buffer layers for YBCO coated conductors' growth is the degree of lattice matching with superconducting layers. However, there is no natural material that has 100% lattice match with YBCO, therefore, in this research mixtures of europium and ytterbium oxides were examined to:

- i) investigate formation of mixed oxides (solid solutions) $(\text{Eu}_{1-u}\text{Yb}_u)_2\text{O}_3$, and find a stoichiometric solid solution which has the same lattice parameter as YBCO
- ii) study textured growth of this 100% lattice matched $(\text{Eu}_{1-u}\text{Yb}_u)_2\text{O}_3$ thin film on textured Ni tape by chemical solution deposition technique.

Processing of $(\text{Eu}_{1-u}\text{Yb}_u)_2\text{O}_3$ mixed oxides involves 4 steps, namely:

- i) preparation of bulk $(\text{Eu}_{1-u}\text{Yb}_u)_2\text{O}_3$ mixed oxides and XRD phase analysis
- ii) precursor solution preparation of the 100% lattice matched mixed oxide with YBCO
- iii) thin film coating

iv) heat treatment

i) Preparation of bulk $(\text{Eu}_{1-u}\text{Yb}_u)_2\text{O}_3$ mixed oxides and XRD phase analysis: A total of seven different compositions of precursor solutions were prepared for bulk samples of $(\text{Eu}_{1-u}\text{Yb}_u)_2\text{O}_3$, where u was 0, 0.1, 0.2, 0.5, 0.8, 0.9, and 1. Europium (III) 2,4-pentanedionate, $[\text{Eu}(\text{CH}_3\text{COCHCOCH}_3)_3\text{XH}_2\text{O}]$ (Alfa Aesar), and ytterbium (III) 2,4-pentanedionate, $[\text{Yb}(\text{CH}_3\text{COCHCOCH}_3)_3]$ (Alfa Aesar), were selected as starting precursors to prepare polycrystalline bulk samples. Eu (III) 2,4-pentadioante was first dissolved in a solution mixture containing methanol, glacial acetic acid and acetyl acetone. After complete dissolution of Eu precursor, Yb precursor was added slowly to the solution. The mixture was stirred about 6 hours to get a clear and transparent solution. For example, to make stoichiometric EuYbO_3 ($\text{Eu}/\text{Yb} = 1$), 5.31×10^{-4} mole of europium (III) 2,4-pentanedionate (0.255 g) was dissolved in 15.8 ml of methanol, 0.5 ml of glacial acetic acid and 1.2 ml of acetyl acetone. After complete dissolution of Eu precursor, 5.31×10^{-4} mole of ytterbium (III) 2,4-pentanedionate (0.25 g) was added to the solution slowly. Finally, the precursors solution was stirred several hours. The precursor solutions were stable at room temperature and no precipitations were observed. The solutions were dried at room temperature by waiting a couple of days, and then they were ground and loosely packed by applying 2 tons of pressure on 0.5 inch diameter sample for heat treatment. The seven samples were heat treated at 1150°C for 10 minutes. The powder samples were prepared primarily for XRD phase analysis.

ii) $(\text{Eu}_{0.893}\text{Yb}_{0.107})_2\text{O}_3$ Buffer Layers Preparation: XRD phase analysis revealed (details in chapter 4) that single phase solid solution $(\text{Eu}_{1-u}\text{Yb}_u)_2\text{O}_3$ formed by the mixture of europium and ytterbium precursors, and the pseudocubic lattice parameter of

$(\text{Eu}_{0.893}\text{Yb}_{0.107})_2\text{O}_3$ is same as the lattice parameter of YBCO. Therefore solution of $(\text{Eu}_{0.893}\text{Yb}_{0.107})_2\text{O}_3$ composition was prepared for buffer layer deposition as described above by mixing europium (III) 2,4-pentanedionate and ytterbium (III) 2,4-pentanedionate at the appropriate ratio. The cation concentration in the solution was adjusted by changing the amount of methanol in the solution. Four cation concentrations, which were 0.025, 0.05, 0.1 and 0.15 M were tested. Continuous $(\text{Eu}_{0.893}\text{Yb}_{0.107})_2\text{O}_3$ buffer layers were obtained by using 0.1 M solution and 1.0 cm/sec withdrawal speed.

iii) Thin film coatings: 10 cm long and 1 cm wide biaxially textured Ni tapes were used as substrates, and basically the procedure of cerium oxide deposition was applied. The reel-to-reel sol-gel dip coating system with an in line three zone furnace was also used for deposition of $(\text{Eu}_{0.893}\text{Yb}_{0.107})_2\text{O}_3$ thin films. The samples were withdrawn from the coating solution bath with a speed of 0.25 – 1.8 cm/s. Generally, the samples were withdrawn from the coating solution bath with a speed of 1.5 cm/s. The temperature of three zone furnace were set around 200, 450 and 550 °C, for zone 1, 2 and 3, respectively. Dip coating process was repeated 3-4 times to achieve the desired thickness. After deposition of each layer, films went through the final heat treatment.

iv) Final heat treatment: After volatile organics were burned out from the film in three zone furnace, the samples were transferred to a tube furnace and annealed under 4% H_2 -Ar gas flow with flow rate of 5 cc/min. Various annealing conditions with temperatures and time ranging from 950 °C to 1170 °C, and from 10 minutes to 1 hour, respectively, were tried to determine the optimum processing conditions of $(\text{Eu}_{0.893}\text{Yb}_{0.107})_2\text{O}_3$ buffer layers on Ni substrates. Highly textured $(\text{Eu}_{0.893}\text{Yb}_{0.107})_2\text{O}_3$

buffer layers were obtained by using 1150 °C and 10 minutes annealing process, and the heating rate was 900 °C/h.

3.4 Microstructure Characterization

A detailed understanding of the microstructure and the ability to control the microstructure of materials are key issues for fabrication of YBCO coated conductors. It has been demonstrated that microstructure and crystallographic orientation of substrates, buffer layers and YBCO directly affect the quality of YBCO coated conductors. Therefore microstructure and especially crystallographic orientation (texture analysis) of Ni substrate and buffer layers were investigated using the following characterization techniques: X-ray diffraction analysis (XRD) (pole figure, ω and ϕ - scans are included), environmental scanning electron microscopy (ESEM), orientation imaging microscopy (OIM), energy-dispersive x-ray spectroscopy (EDS), and differential thermal analysis (DTA), were used to determine processing parameters. First DTA was applied to the Ce xerogels, which were dried at room temperature, to determine the thermal reactions and set temperatures of three zone furnace of the dip coating system. All organics should be burnt out in the three zone furnace after each coating process to get highly dense buffer layers.

3.4.1 Differential Thermal Analysis (DTA)

DTA is an analytical experimental technique that is used to investigate the behavior of samples as a function of temperature. The test sample and a thermally inert reference sample are heated or cooled under identical conditions and any temperature differences, which develop between them, are recorded. After that the differential temperature is plotted versus either time or the temperature at some fixed point within the

apparatus. If a physical or chemical change occurs in the test sample, which releases heat, the temperature of the sample rises temporarily above that of the reference sample, thus giving rise to an exothermic peak on the DTA. Conversely, if the test sample absorbs heat, the temperature of the test sample will be behind that of the reference material leading to an endothermic peak. The amount of heat evolved or absorbed by the test samples during any physical or chemical reactions can be quantified by the area under any given DTA peak. The peak area is in fact a measure of the total enthalpy change and that is not affected by the heat capacity of the sample.

Room temperature dried the xerogels of CeO_2 buffer layer precursor solution were ground into powder in an agate mortar and pestle. About 30 mg of powder xerogel were used, and it was sandwiched between high purity Al_2O_3 powder. Typically 20 mg of Al_2O_3 was put at the bottom of the test crucible to prevent contamination of the ceramic DTA crucible from the xerogel during the test, then 30 mg of xerogel powder put on the Al_2O_3 powder and finally 10 mg of Al_2O_3 powder was placed to prevent again contamination of the furnace and crucible of DTA. As a reference material same high purity Al_2O_3 powder was also used. The Perkin Elmer DTA was used, and the temperature range was chosen between 700 and 800 °C and the heating rate was 10 °C/min. for the analysis. The DTA analysis was conducted in air to study thermal phenomena of the buffer layers to mimic the actual processing conditions (non-vacuum, in air).

3.4.2 X-ray Diffraction Analysis (XRD)

XRD is a powerful technique used to uniquely identify the crystalline phases present in materials. It is a nondestructive method, and can be used in most environments.

Thin film XRD is important in many technological applications, because of its abilities to accurately determine strains and to uniquely identify the presence and composition of phases. Although other techniques like Rutherford Backscattering Spectrometry (RBS), X-Ray Photoelectron Spectroscopy (XPS), and X-Ray Fluorescence (XRF) yield film stoichiometry, X-Ray Diffraction (XRD) also provide phase identification.

The X-ray beam interacts with atoms in a crystal structure and the x-rays are scattered in all directions. Some of the scattered beams will be completely in phase and so reinforce each other to form diffracted beams. Basically the primary beam is diffracted from the sample to the detector. W.L. Bragg first time formulated the diffraction condition, which is called Bragg condition and is given by Eq. (3-1)

$$n\lambda = 2d\sin\theta(1) \quad (3.1)$$

In this equation; λ is the monochromatic x-ray wavelength, n is the order of diffraction, and the smallest value of n is 1. 2θ is the angle between the incident and diffracted beams, and d represents the interplanar spacing between the planes that are participating in the diffraction. A plot of the diffraction angle 2θ versus the intensity in counts or counts per second shows diffraction pattern of the test sample.

Each grain in most polycrystalline material has a crystallographic orientation, which is different from these of the adjacent grains. If the aggregate of grains has a particular orientation, it is called preferred orientation or texture, which may be simply defined as a non-random crystal orientation. In metals and alloys preferred orientation is generally formed by a forming process that is called deformation texture. When the deformed metal is recrystallized by annealing process, the new grain structure usually has a preferred orientation, which is called recrystallization texture or annealing texture.

Preferred orientation is also present in rocks, in ceramics, in thin films coatings and in both natural and artificial polymeric fibers and sheets [66]. Since grain orientation of a polycrystalline material affects the macroscopic properties of materials, determination of orientation of grains are always scientists' interests. If all of the grains of a material have a preferred orientation, it is expected to observe anisotropic properties at the microscopic level. On the other hand, if the grains are randomly oriented, dominant isotropic properties are expected. In coated conductors critical current density strongly depends on the texture of superconducting layers, and highly textured superconductors can only be grown on highly textured buffer layers with current processing technologies. Crystalline orientation of materials can be analyzed by XRD pole figure, rocking curve and phi scans.

A pole figure is a stereographic projection and is used to display the angular relationship between crystallographic planes and directions of the specimen. All the crystallographic planes in a crystal can be represented by a set of normals of these planes. If a reference sphere is imagined, the planes' normals intersect the surface of the sphere in a set of points called poles, and the pole of a plane represents, by its position on the sphere, the orientation of the plane. The essential of pole figure measurements of specimens is straightforward using 4-circle X-ray diffractometer. To determine the orientation of a crystallographic plane (hkl) of a crystal by pole figure analysis, the detector is fixed at the proper 2θ Bragg angle of the plane to collect the diffracted beam, and then the specimen is rotated in its own plane. The pole figure is a projection made on a plane parallel to the sheet surface and therefore rotates with the sheet. The intensity of the diffracted beam of a particular plane at each specimen position is taken to be

proportional to the volume fraction of the crystallites [66].

The crystalline structure of buffer layers was analyzed using powder X-ray diffraction. X-ray diffraction profiles of buffer layers were collected using a Scintag diffractometer with Cu K α radiation. Generally the data were recorded at room temperature over the range of 27° and 67° in 0.02° steps with an integration time of 2 second. Since 2 θ degree of (111) plane of CeO₂ buffer layer and (200) plane of Ni substrate are 28.54° and 51.84°, by choosing the range of 27° and 67°, all major peaks of the buffer layer and the substrata were covered. The same range was also chosen for $\theta/2\theta$ scan of (Eu_{0.893}Yb_{0.107})₂O₃ buffer layers. The diffraction data were recorded for (Eu_{1-u}Yb_u)₂O₃ mixed oxide in the range of 18° and 82° in 0.02° steps with an integration time of 12 seconds. Each experiment was set to be an overnight scan to collect precise data because the data were used to calculate lattice parameters of the mixed oxides. Accurate profile fitting was carried out for the seven diffraction patterns applying the profile fitting program ProFit from Philips software with pseudo-Voigt as a profile shape function. The accurate peak positions obtained from the fitting were used to determine precise lattice parameter (a) through a non-linear least squares procedure applying regression diagnostics [161], which allow the refinement of the zero shift.

Texture analysis of CeO₂ and (Eu_{0.893}Yb_{0.107})₂O₃ thin films such as pole figures, out-of-plane and in-plane texture were examined by X-ray Philips MRD four-circle diffractometer. X-ray omega (ω)-scan was used to evaluate out-of-plane texture, whereas in-plane orientation of the films was investigated by phi (ϕ)-scan.

3.4.3 Environmental Scanning Electron Microscopy (ESEM)

Traditionally, the first instrument that would come to mind for small-scale

materials characterization would be an optical microscopy. As the sophistication of investigations increased, the optical microscope often has been replaced by scanning electron microscopy. SEM has good spatial resolution and depth of focus. Because of its reasonable cost and the wide range of information that it provides in a timely manner, the SEM often replaces the optical microscope as the preferred starting tool for materials studies. Not only is topographical information produced in the SEM, but information concerning the chemical composition of near surface regions of the material is provided as well. Surfaces that exhibit grain structure (fracture surfaces, or decorated surfaces) can obviously be used to characterize the grain size and shape [162].

Microstructure of nickel tape and buffer layers were analyzed by environmental scanning electron microscope (ESEM). Basically ESEM is like SEM but provides additional opportunity to examine electrically insulating materials without a conductive coating layer like carbon and gold. Specifically, we will examine surface morphology of coatings, existence of micro cracks and pinholes in the coatings. This examination will give us useful information about uniformity of the films.

3.4.4 Orientation Imaging Microscopy (OIM)

OIM is used with an electron microscope to investigate crystallographic texture or preferred orientation of the grains in the samples. Automated indexing of electron backscatter diffraction (EBSD) patterns (Kikuchi patterns) provide unique features for microstructure characterization of materials like microtexture analysis, phase identification, local grain orientation, orientation distribution of grains, grain size, misorientation angles, and grain boundary and texture maps. EBSD patterns are formed by diffraction of backscattered electrons by crystal lattice near the surface of the sample,

and observation of electron backscatter diffractions was first observed by Kikuchi in 1928 using a thin mica crystal. Kikuchi described the occurrence of remarkable lines by formation of inelastic scattering within the specimen because of divergent beam source. Venables and Harland described how backscattered electrons could theoretically produce Kikuchi patterns in the scanning electron microscope. Then Dingley detected these backscatter electron Kikuchi patterns using a video camera inside an SEM, and also developed computer assisted indexing of Kikuchi patterns [163]. The Orientation Imaging Microscope, developed by Adams et al. in 1993, allows a computer to control both the SEM stage and the camera so that Kikuchi patterns could be quickly collected and rapidly indexed [164]. The advances in hardware and software of OIM have increased in the past decade, and the popularity of OIM also heightened because of integration with existing SEMs and new application areas.

In an SEM with an OIM system the specimen is tilted to have typically 20° between the electron incident beam and the specimen surface. This is to enhance the yield of backscattered electrons that undergo diffraction, and escape from the specimen surface. When the incident electron beam interacts with a crystalline solid material, electrons scatter diffusely and inelastically in all directions. Some of the electrons satisfy the Bragg's law at every set of lattice planes, and these electrons undergo elastic scattering to give a strong and reinforced beam. The paths of the diffracted electrons lie on the surfaces of a cone. Electron scattering can be considered between lattice planes thus two cones of radiation result from each family of planes. When a phosphorous screen of an ESBD camera is placed near the specimen, the diffraction cones are intercepted and appear to be straight parallel lines. A pair of Kikuchi lines is known as a

Kikuchi band, which has a distinct width that is a function of the lattice plane spacing (corresponds to a specific crystallographic plane). The positions of the bands on the screen depend on the crystallographic orientation of the diffracted planes. A collection of Kikuchi bands makes up a Kikuchi pattern. Therefore the Kikuchi patterns have angular relationships in a crystal and implicitly contain the information about crystal symmetry. The bands' intersection is called a zone axis (pole).

Orientations of grains defined by an arbitrary misorientation angle of the nickel tape were analyzed using OIM, which was attached to the ESEM.

3.4.5 Energy-Dispersive X-ray Spectroscopy (EDS)

EDS is an extremely powerful analytical technique of special value in conjunction with electron optic instruments. In a few minutes a qualitative survey of the elements present in almost any sample can be made, and in only a few minutes sufficient data can be collected and analyzed for quantification. With modern detectors and electronics most EDS systems can detect X rays from almost all the elements in the periodic table, if present in sufficient quantity. EDS has been used for quality control and test analysis in many industries including: semiconductors, metals, and polymers. The main advantages of EDS are its speed of data collection, the ease of use. The disadvantages are poor energy resolution of the peaks, relatively low peak-to-background ratio. There are three modes of analysis commonly used: spectrum acquisition, mapping of the elements and elemental line scans [162].

Qualitative analysis of buffer layers structures (multilayer coatings) were analyzed by EDS.

CHAPTER 4 RESULTS AND DISCUSSIONS

4.1 Processing and Characterization of Textured Nickel Substrates

Since substrate preparation is a critical part of fabrication of YBCO coated conductors, sharpness and homogeneity of textured structure, surface smoothness and cleanness of Ni substrates were carefully examined after recrystallization heat treatment. To be able to overcome “weak-link” inter-grain current transport problems in superconducting films, well textured substrates are needed. Therefore, to understand and see biaxial texture formation in thermomechanically processed Ni substrate, X-ray $\theta/2\theta$ scans of a bulk Ni piece, cold rolled Ni tape and heat treated Ni tape at 1050 °C for 30 minutes were investigated. In Figure 4.1(a) and (b) X-ray $\theta/2\theta$ scans of the samples are seen. Figure 4.1(b) is same as Figure 4.1(a) except each scan is shifted to the right by 2.5° with respect to the one below to show peak of each XRD pattern clearly. The peaks of (111), (200) and (220) planes are clearly from bulk Ni sample, and the random peak is (200). When a bulk metal sample is rolled, most of the grains become oriented with a certain crystallographic plane (hkl) roughly parallel to the sheet surface, and a certain direction $[uvw]$ that is generally rolling direction. Since this preferred orientation is due to the rolling process, it is called rolling texture. In the case of FCC Ni tape, the majority of the grains are oriented as their (220) planes to be parallel to the plane of the tape after rolling process, for that reason the highest intensity peak was (220). The reflections from (111) and (200) planes are still exist but intensities were less compare to those of bulk Ni

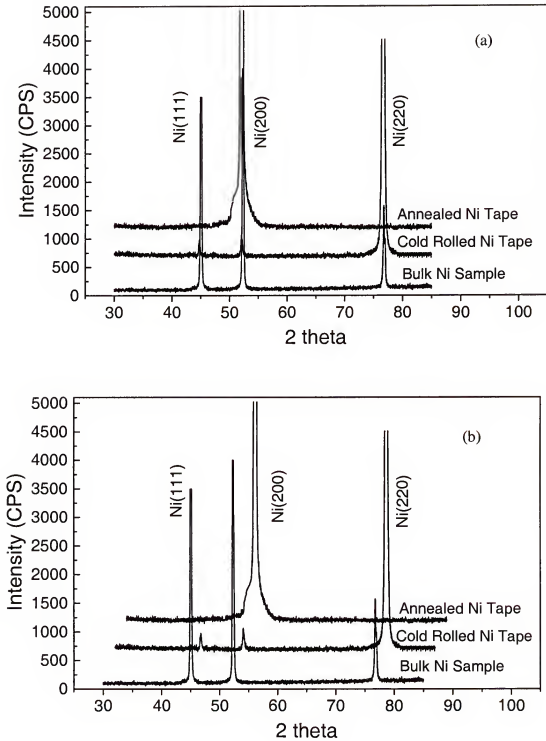


Figure 4.1. The X-ray $\theta/2\theta$ scan of a bulk Ni sample, a cold rolled Ni tape, and an annealed Ni tape. A) without any shift. B) Same as in (a) except each scan has been shifted to the right by 2.5° with respect to the one below to show each peak of each XRD pattern clearly.

sample which indicates that there are some grains in the (111) and (200) planes orientation. However, after recrystallization heat treatment of cold rolled Ni tape which was heat treated at 1050 °C for 30 minutes [160], the only peak of (200) plane was obtained. This shows some degree of texture in the substrate, however, more detailed texture analysis such as pole figure, out-of-plane texture (rocking curve scan) and in-plane texture (phi scan) analysis need to be performed to quantify the texture of Ni tape. The Full-Width-Half-Maximum (FWHM) values of the rocking curve (ω) and phi (ϕ) scans give deviation from perfect alignment, and therefore quantify the degree of texture.

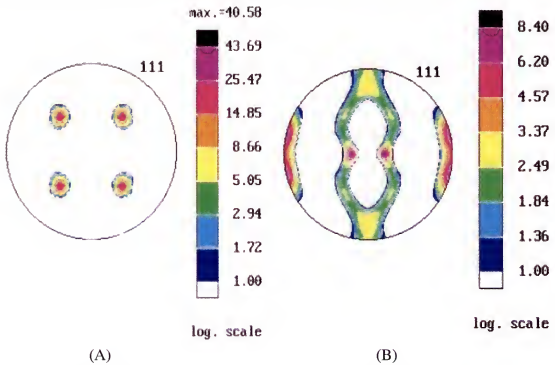


Figure 4.2. The logarithmic scale and background corrected typical (111) pole figures of Ni substrates. A) Biaxially textured Ni tape, which was annealed at 1050 °C for 30 min. B) Cold rolled Ni tape.

Figure 4.2(a) and (b) shows background corrected (111) logarithmic scale pole figures of Ni substrate, which was annealed at 1050 °C for 30 minutes, and cold rolled Ni tape samples, respectively. Four-fold symmetry of the four poles in which the center of

each quadrant is clearly seen from Figure 4.2(a). These poles corresponds four [15] planes of the cubic system like $(\bar{1}11)$, $(\bar{1}\bar{1}1)$, $(1\bar{1}1)$ and (111) , and their positions are the exact position for a cubic crystallographic system. Therefore the (111) pole figure indicates the cube texture quality $[16]\langle 001 \rangle$ in which each grain is oriented with its (100) planes parallel to the sheet surface, and the $[001]$ direction in these planes is parallel to the rolling direction. On the other hand, some deformation texture “rolling texture” is seen from pole figure of cold rolled Ni tape. The $[15]$ planes, which are not parallel to the sample’s surface, are about 10° deviated from normal direction. There are some kinds of a concentration of $[15]$ planes along the transverse direction. $[165]$ planes are aligned parallel to the normal direction of the sample and the $\langle 112 \rangle$ direction is parallel to the rolling direction of the sample, which is called brass texture $[165]\langle 112 \rangle$. These pole figures of cold rolled and annealed Ni substrates are similar with the published results in the literature [166].

As discussed before the degree of out-of-plane (c-axis) texture and in-plane (a, b axis) texture are determined by omega (ω) scan of (200) plane and phi (ϕ) scan of (111) plane, respectively. The FWHMs of the peaks give quantitatively the deviation from the perfect alignment. The ω and ϕ - scans of annealed Ni tape are seen in Figure 4.3 and Figure 4.4, and FWHMs of the ω and ϕ - scans are 6.9° and 8.12° , respectively. These values are similar to the published data in the literature for pure Ni and Ni alloys [8, 22, 167, 168]. Generally, up to 15° of deviation is acceptable but the smaller the value, the better the texture. The data, which were obtained in this research, were way below from the acceptable 15° of deviation, which are indication of good out-of-plane and in-plane texture. FWHM value of ω - scan is smaller than that of ϕ - scan as expected. This shows

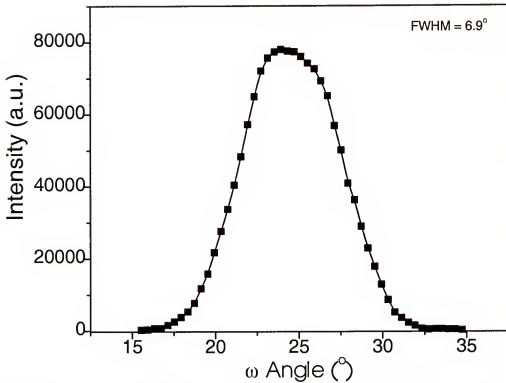


Figure 4.3. The ω -scan of (200) plane of the biaxially textured Ni tape, which was annealed at 1050 $^{\circ}\text{C}$ for 30 min.

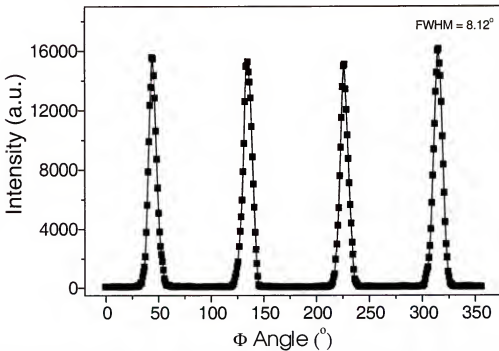


Figure 4.4. The ϕ -scan of (111) plane of the biaxially textured Ni tape, which was annealed at 1050 $^{\circ}\text{C}$ for 30 min.

that the Ni substrate has better out-of-plane texture than in-plane texture. Pole figure, ω , and ϕ - scans results clearly showed that very sharp and fully formed cube textured structure were obtained in pure Ni tapes by this thermomechanical process. To be able to investigate texture uniformity of Ni substrate over the length, XRD out-of-plane and in-plane texture analysis were performed on 3 substrate samples each of which were 10 cm long and were annealed at the same conditions. The substrates were mounted on 12.5 cm diameter sample holder of the XRD machine, x, y, and z coordinates of which are computer controlled. The texture measurements were repeated at 1 cm intervals to cover the entire tape length. The degrees of out-plane and in-plane alignments in, other words the deviations from the perfect alignments were shown in Figure 4.5. It is clearly seen from Figure 4.5 that sharp and homogeneous cube textured structure were obtained over the length of the 1 cm long samples.

EBSD technique yields electron backscatter Kikuchi pattern, which provides orientation and phase identification of the sample. Figure 4.6 shows typical EBSD Kikuchi patterns obtained from biaxially textured Ni substrate, which was annealed at 1050 °C for 30 minutes. Very well defined Kikuchi patterns obtained from the Ni substrate with a step size of 5 μm , and the patterns were indexed, and they were stored for further calculations and regenerations of grain maps. Indexing of the pattern at each location provided a unique measure of the orientation at that point. Basically, the output file contains location and orientation of each point in the scan. Grain boundary misorientations were calculated for all grain boundaries using OIM 2.6 software, and the grain micrographs were then regenerated based on grains' orientations. In Figure 4.7 grains have been colored according to the criterion that a single color represents a unique

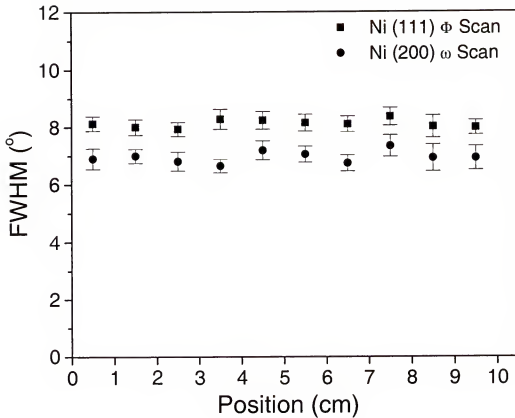


Figure 4.5. FWHM values of ω and ϕ - scans of 10 cm long biaxially textured Ni tapes, which were annealed at 1050 °C for 30 min.

continuous orientation. The grains were colored with the orientation changes less than 11, 9, 8, 7, 6, 5, 3, and 1° in Figure 4.7(a), (b), (c), (d), (e), (f), (g), and (h), respectively. As seen from the figure that most of the substrate is percolatively connected within 6°. The whole scanned area appears to be single grain for 11° misorientation angle, which is smaller than the acceptable 15° for coated conductor development. The surface roughness of Ni substrate is controlled by the surface quality of rolls of the rolling machine.

Therefore, the Ni substrates were rolled with polished rolls as reported by Hyper Tech Research Inc. Surface morphology of the annealed Ni substrates were investigated using ESEM as seen in Figure 4.8. The micrographs were taken after annealing process; therefore grain boundary grooves are clearly discerned. These grain boundary grooves are

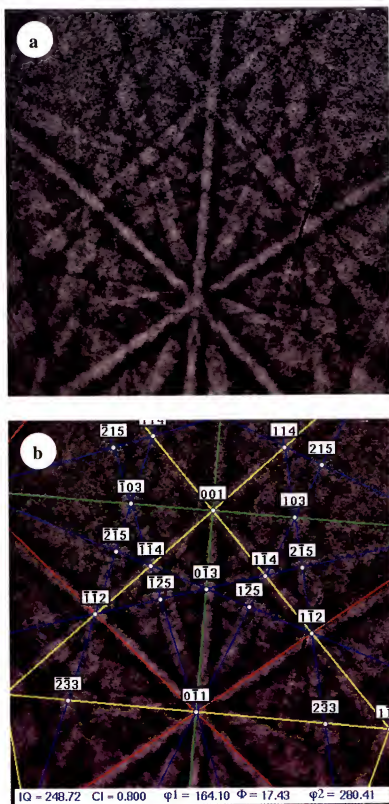


Figure 4.6. EBSD Kikuchi patterns of a biaxially textured Ni tape, A) As collected. B) As indexed EBSD Kikuchi pattern.

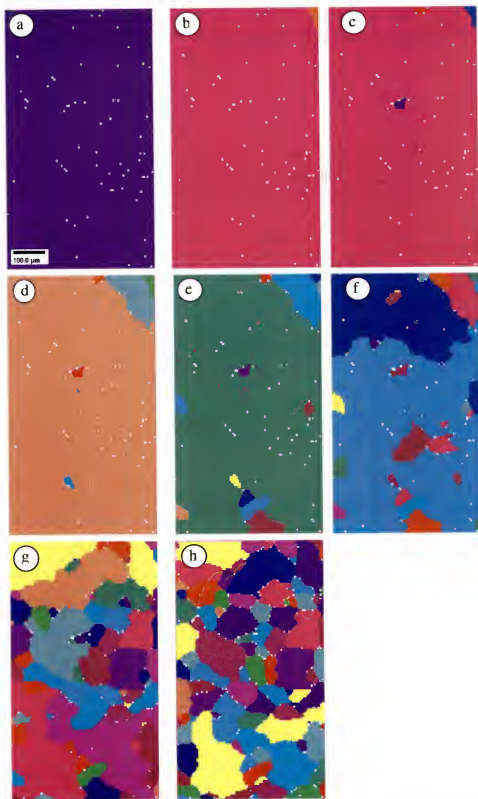


Figure 4.7. OIM micrographs of a biaxially textured Ni tape. The grains were colored based on the orientation changes with criterion less than 11, 9, 8, 7.6, 5, 3, and 1° , in a, b, c, d, e, f, g and h, respectively.

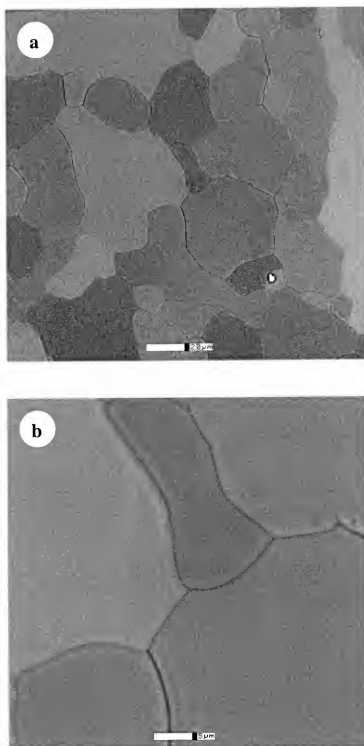


Figure 4.8. ESEM micrographs of biaxially textured Ni substrate, which was annealed at 1050 °C for 30 min. Grain boundary grooves are clearly seen from these plain view micrographs of the surface of the substrate. The white scale bars of (a) and (b) are 20 μm and 5 μm , respectively.

not desirable, however, no solutions have been found to prevent formation of the grooves in pure Ni. Since buffer layers follow the surface morphology of Ni substrate, these grooves are possible places that may promote high angle grain boundaries in YBCO films.

4.2 Processing and Characterization of CeO₂ buffer layer.

Buffer layers transfer the crystal orientation of the metal substrate to the superconducting layer while preventing oxidation of the substrate and diffusion of metal ions into the superconducting layer. Cerium oxide is chemically compatible with Ni and YBCO, and it is stable under hydrogen-argon gas mixture, which is used in annealing process to protect Ni against oxidation, also CeO₂ has very close lattice parameter to that of YBCO. Therefore, CeO₂ is one of the most widely used buffer layers for YBCO coated conductor development. CeO₂ has a fluorite structure with a lattice constant of 5.411 Å at room temperature. The lattice mismatch between CeO₂ and YBCO can be calculated in the following way. Lattice parameter of CeO₂ is 0.13% bigger than that of YBCO along the a axis, and 1.54% smaller than that of YBCO when the CeO₂ basal plane is rotated by 45° as seen in Figure 4.9.

Ni substrate has an FCC crystal structure with 3.52 Å lattice parameter. The lattice mismatch between Ni and CeO₂ is 8.69%. Lattice parameter of CeO₂ is 8.69% bigger than that of Ni when the CeO₂ basal plane is rotated by 45° as seen in Figure 4.10.

As described in Chapter 3, the solution of CeO₂ buffer layer was prepared from cerium 2,4-pentanedionate precursor. It has been known that pentanedionate based precursors and acetylacetone-derived solutions have low reactivity and higher crystallization temperatures [169] than acetic acid derived solutions. Several researchers

have also reported that high density films were obtained using pentanedionate based precursors and acetylacetone-derived solutions in the processing of ZrO_2 films [170] and PZT films [171]. Since longer solution lifetime and denser films are desired in the chemical solution processing of buffer layers, less reactive cerium 2,4-pentanedionate precursor was chosen.

A series of experiments at various solution concentrations and substrate's withdrawal speeds were made to find optimum coating parameters. Cation concentration of the solution was adjusted by methanol, and 4 different solution concentrations like 0.025, 0.05, 0.1 and 0.15 M were tested. Concentration of the solution is one of the parameters that controls thickness per pass of the buffer layers. Substrate's withdrawal speed in the reel-to-reel dip coating system also determines thickness of buffer layers. Therefore, various withdrawal speeds such as 0.25, 0.60, 1 and 1.5 cm/s were used to find optimum withdrawal speed for CeO_2 buffer layers.

At low solution concentrations like 0.05 M non-continuous films were obtained as seen in Figure 4.11. Slow withdrawal speeds also caused non-continuous films because most of the solution returned back to the solution tank before drying on the substrate. After the annealing process cracks were formed in the films, which were deposited using the 0.15 M cerium precursor solution as seen in Figure 4.12. The cracks were also present in CeO_2 buffer layer when withdrawal speed of 1.5 cm/s and solution concentration of 0.1 M was used. Cracks formation at high withdrawal speeds could be explained by deposited film thickness per coating process, because majority of the solution stay on the substrate while the substrate entering the three zone furnace.

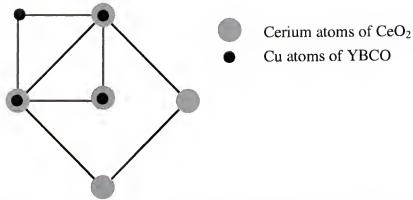


Figure 4.9. Plane view schematic drawing of crystal structures of CeO_2 and YBCO. Only Ce atoms of CeO_2 and Cu atoms of YBCO are shown.

$$a_{\text{CeO}_2} * \frac{\sqrt{2}}{2} = 5.411 * \frac{\sqrt{2}}{2} = 3.826 \text{ \AA}$$

$$a_{\text{YBCO}} = 3.821 \text{ \AA} < 3.826 \text{ \AA}$$

$$b_{\text{YBCO}} = 3.885 \text{ \AA} > 3.826 \text{ \AA}$$

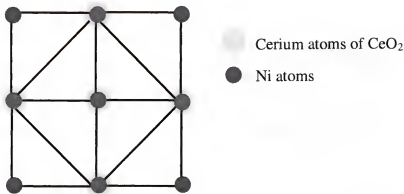


Figure 4.10. Plan view schematic drawing of crystal structures of CeO_2 and Ni. Only Ce atoms of CeO_2 and Ni atoms are shown.

Numerous crack formation have been reported in CeO_2 buffer layers on Ni substrates, which were processed by vacuum techniques, and the crack formation is attributed to the film thickness [96, 172]. However different critical film thicknesses,

which were 50 nm [96] and 20 nm [172] have been reported to get crack free buffer layers. Effects of the thermal expansion coefficient and lattice parameter differences of the film and the substrate on the crack formation were investigated. Oh et al. did a comparative study on crack formations in the CeO₂ buffer layers using Ni and Pt substrates [172]. It was concluded that it is unlikely that the differential thermal expansion initiates cracks in the film. Because the film would be under compressive stress CeO₂/Ni, when a vacuum deposition technique was used. One of the most plausible explanations of the crack formations was intrinsic stress generated by the vacancy defect mechanism that originated from the lattice mismatching [172]. However, in our case the film would be under tensile stress while heating up, and it would be under compressive stress while cooling down to room temperature.

Table 4.1. Some of the physical parameters of Ni and CeO₂.

	Ni	CeO ₂
Thermal expansion coefficient (X 10 ⁻⁶ K ⁻¹)	13.4	9.5
Lattice Parameter (Å)	3.52	3.826*

$$* a_{\text{CeO}_2}/\sqrt{2}$$

Finally, 0.1 M solution concentration and 1 cm/s substrate withdrawal speed were found to be optimum conditions for coating process to have continuous, crack free and homogenous CeO₂ buffer layers using the Ce precursor solution. The thickness of the CeO₂ buffer layers was about 30 nm.

After having some promising results from CeO₂ buffer layers solution, DTA analysis was conducted to understand thermal phenomena of the CeO₂ thin film formation from the precursor solution. In Figure 4.13 DTA analysis of RT dried Ce xerogels is seen. Five exothermic peaks were observed in the range of 25 °C and 350 °C.

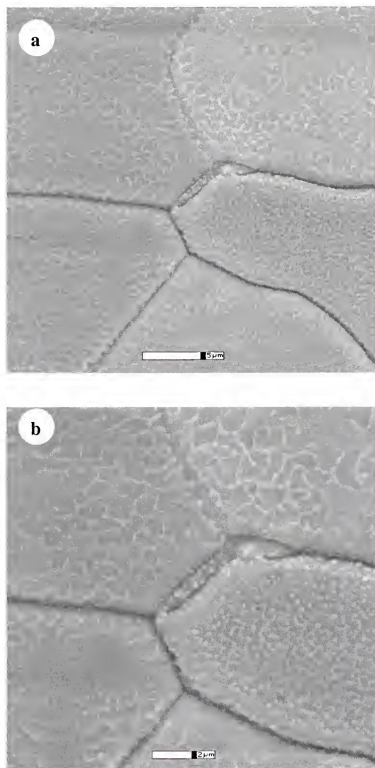


Figure 4.11. Surface morphologies of non-continuous CeO_2 films on biaxially textured Ni substrate, which was processed from 0.05 M Ce cation precursor solution. The white scale bars of (a) and (b) are 5 μm and 2 μm , respectively.

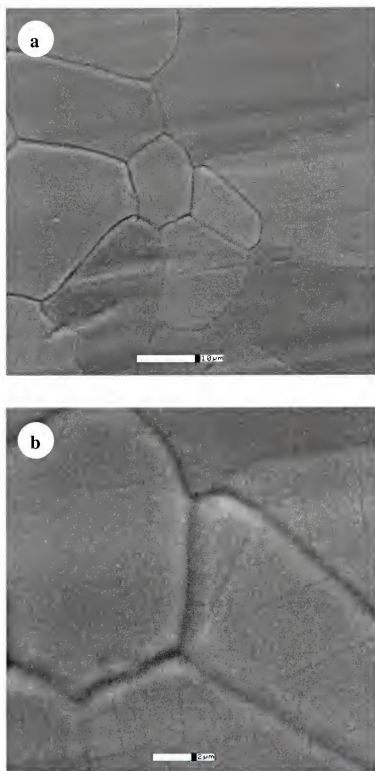


Figure 4.12. Surface morphologies of cracked CeO_2 films on biaxially textured Ni substrate, which was processed from 0.15 M Ce cation precursor solution. The white scale bars of (a) and (b) are 10 μm and 2 μm , respectively.

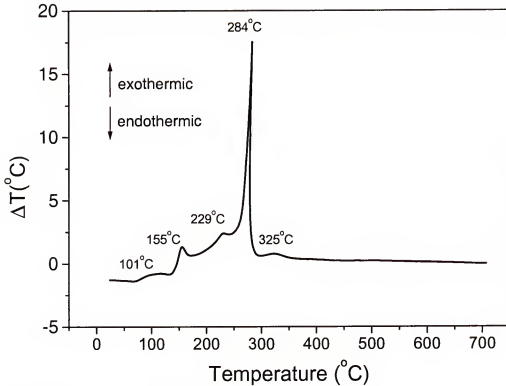


Figure 4.13. DTA analysis of RT dried Ce xerogels.

No peaks were seen above 350 $^{\circ}\text{C}$. One big and four small peaks were seen between 95 $^{\circ}\text{C}$ and 350 $^{\circ}\text{C}$ due to the burning of organics in the xerogels powder. Mainly organics burnt out at 284 $^{\circ}\text{C}$, and then oxidation peak was seen at 325 $^{\circ}\text{C}$. Since the solution was dried at RT, a sudden reaction occurred at 284 $^{\circ}\text{C}$ that the sharp exothermic peak indicates the burning of organics in xerogels.

A series of experiments at various annealing temperatures and time ranging from 900 $^{\circ}\text{C}$ to 1170 $^{\circ}\text{C}$, and from 10 minutes to 1 hour, respectively, in flowing forming gas atmosphere (5 cc/min.) in a tube furnace were made to determine the optimum annealing conditions of CeO_2 buffer layers on Ni substrates. 900 $^{\circ}\text{C}/\text{h}$ heating rate was used for annealing process. X-ray $\theta/2\theta$ scan is the most convenient and fast test to check texture of the materials qualitatively. X-ray $\theta/2\theta$ scans of CeO_2 buffer layers on biaxially textured Ni substrate, which were annealed at 900 $^{\circ}\text{C}$ for 30 min., 1050 $^{\circ}\text{C}$ for 30 min. and 1150

°C for 10 min. are seen in Figure 4.14. (111) and (200) peaks of CeO_2 are seen from the sample, which was annealed at 900 °C for 30 min. Since (111) oriented grains are not desirable, higher annealing temperatures were tried to eliminate (111) oriented grains, and only (200) oriented grains were obtained by annealing process at 1050 °C for 30 minutes and at higher temperatures.

Since biaxially textured Ni substrate was used for CeO_2 deposition, only Ni (200) peak is seen from $\theta/2\theta$ scan of CeO_2/Ni structure. Missing CeO_2 (111) peak at 28.54° which is the random peak, and having only (200) peak from CeO_2 buffer layer is an indication of cube textured structure but pole figure analysis, ω and ϕ - scans are required for full texture characterization.

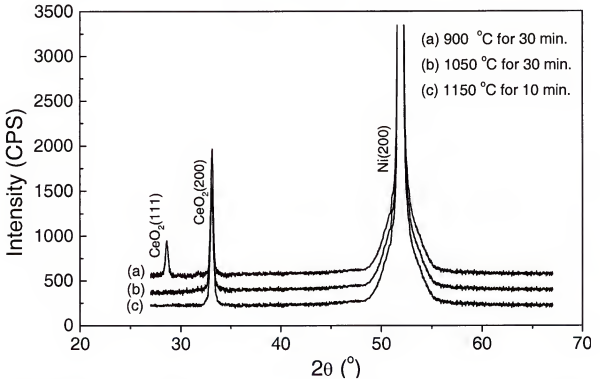


Figure 4.14. The X-ray $\theta/2\theta$ scans of CeO_2 buffer layers, which were annealed at varying temperatures and time as marked, on biaxially textured Ni substrate.

To investigate effect of annealing temperature and time on cube texture quality, ω and ϕ - scans of the buffer layers which were annealed at 1050 °C for 30 min., 1150 °C for 10 and 30 min., 1170 °C for 30 minutes were collected. The background corrected and logarithmic scale (111) pole figure of CeO₂ buffer layer, which was annealed at 1150 °C for 10 minutes deposited on biaxially textured Ni substrate is shown in Figure 4.15(b). The (111) poles of CeO₂ are rotated 45° with respect to the (111) poles of Ni. (100) crystallographic planes of CeO₂ are parallel to the substrate, the [001] axis of CeO₂ buffer layers is 45° rotated from the rolling direction of Ni substrate [166, 173]. The cube texture relationship between CeO₂ buffer layer and Ni substrate can be symbolized as follows: CeO₂ [001]//Ni [001] and CeO₂ [110]//Ni [100]. The CeO₂ buffer layers exhibit good texture, because distinct in-plane alignment is seen from well-defined poles (four fold symmetry).

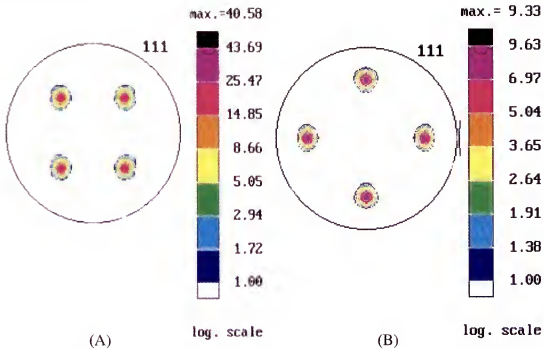


Figure 4.15. The logarithmic scale and background corrected (111) pole figures. A) Biaxially textured Ni tape. B) Biaxially textured CeO₂ buffer layer.

The out-of-plane and in-plane texture qualities of CeO_2 buffer layers, which were investigated by ω and ϕ - scans. It was found that the FWHMs ω and ϕ - scans of annealed 1150°C for 30 minutes annealed CeO_2 are smaller than that of 1050°C for 30 minutes annealed CeO_2 . It means that out-of-plane and in-plane alignments of CeO_2 increase with increasing annealing temperature. However, not big differences were observed between FWHMs of CeO_2 layer for annealing conditions of 1150°C , 10 minutes and 1170°C , 30 minutes as seen in Table 4.2. Therefore, 1150°C , 10 minutes was chosen as an optimum annealing condition for the process. In Figure 4.16 ω - scan of (200) plane of CeO_2 buffer layer, which was annealed at 1150°C for 10 minutes is seen. FWHM of the peak is 6.47° . This is a considerably low value and shows that grains of CeO_2 have high degree of out-of-plane texture. ϕ - scan of (111) plane of CeO_2 buffer layer is seen in Figure 4.17. The FWHM is 7.42° and this also shows that CeO_2 has a good degree of in-plane texture.

Table 4.2. FWHM values of ω and ϕ - scans of Ni and CeO_2 buffer layers, which were annealed at varying conditions.

Materials	Annealing Conditions	ω - scan ($^\circ$)	ϕ - scan ($^\circ$)
Ni	1050°C , 30 min.	6.9	8.12
CeO_2	1050°C , 30 min.	7.43	8.76
CeO_2	1150°C , 10 min.	6.47	7.42
CeO_2	1150°C , 30 min.	6.43	7.39
CeO_2	1170°C , 30 min.	6.35	7.34

Out-of-plane and in-plane texture uniformity of CeO_2 buffer layers over 10 cm long sample is seen in Figure 4.18. Three pieces of 10 cm long CeO_2 buffer layers were

coated on Ni at same conditions but different time. The length of the samples was limited with 10 cm, because the uniform hot zone of the furnace was about 10 cm long. Texture

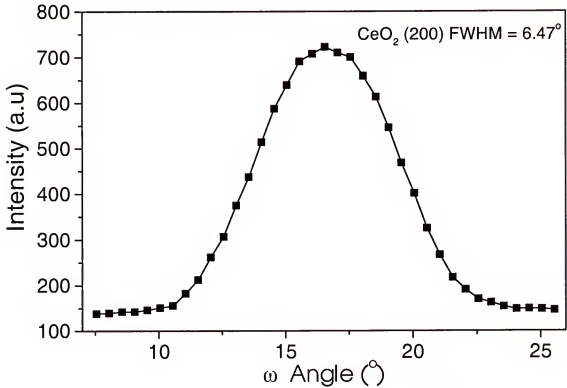


Figure 4.16. The ω - scan of biaxially textured CeO_2 buffer layer, which was annealed at 1150°C for 10 min., on biaxially textured Ni substrate.

uniformity of these 3 samples, each of which was 10 cm long was analyzed along the length. The measurements were repeated with 1 cm intervals to cover the entire tape length, and a total of 30 ω and ϕ - scan data were collected. As seen from Figure 4.18, well textured and uniform CeO_2 buffer layers were deposited over the 10 cm long biaxially textured Ni substrate by chemical solution deposition technique. FWHMs of out-of-plane and in-plane textures of the CeO_2 buffer layers are similar to those of other buffer layers, which were deposited by chemical solution [151, 173-175].

Highly textured structure is one of the important properties that every buffer has to have to facilitate epitaxial growth of YBCO films. But at the same time buffer layers

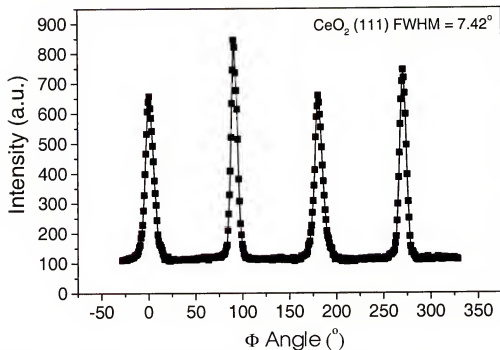


Figure 4.17. The ϕ - scan of biaxially textured CeO_2 , which was annealed at 1150°C for 10 min., on biaxially textured Ni substrate.

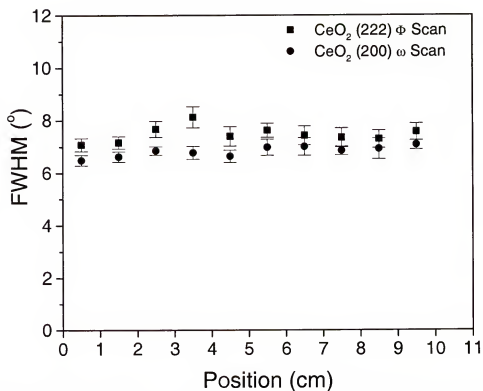


Figure 4.18. FWHMs of ω and ϕ - scan of 10 cm long biaxially textured CeO_2 buffer layer, which was annealed at 1150°C for 10 min., on biaxially textured Ni substrate.

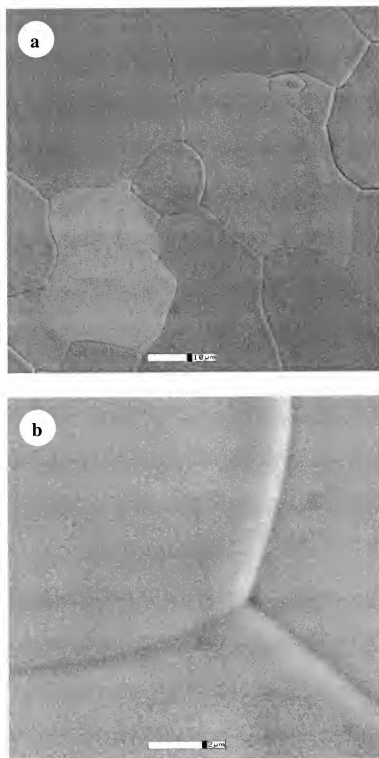


Figure 4.19. Surface morphologies of biaxially textured CeO_2 films on biaxially textured Ni substrate. The white scale bars of (a) and (b) are 10 μm and 2 μm , respectively.

have to be crack free and pinhole free to prevent diffusion of metal ions and any reaction between metal substrate and the superconducting film. Surface morphology is also an important parameter; smooth and textured surfaces are favorable to epitaxial growth. Therefore, the surface morphology of the CeO_2 buffer layers was investigated by using ESEM. One of the advantage of using ESEM is electrically insulating materials can be examined without a conductive coating layer like carbon or gold. The surface morphology of highly textured CeO_2 thin film, which was deposited using 0.1 M concentrated solution and 1 cm/s substrate withdrawal rate is seen in Figure 4.19. Two micrographs with different magnification are presented to show general area and details. The surface is very smooth and is free from cracks and pin holes. Since CeO_2 buffer layers followed the surface morphology of the Ni substrate, grain boundaries and grain boundary triple junctions of it are seen in the figure. Thickness of the highly textured and crack free film was determined to be about 30 nm, and thickness of the buffer layers could be changed by repeating the coating process, and changing viscosity of the solution and withdrawal speed of the substrate.

4.3 Processing and Characterization of $(\text{Eu}_{1-x}\text{Yb}_x)_2\text{O}_3$ Buffer Layers

Several buffer layers have been studied for coated conductor development, and still research and development continue on buffer layers, different buffer layer architectures, processing techniques. As mentioned before one of the most important requirements for buffer layers is lattice match with YBCO to facilitate the epitaxial growth of YBCO. In Table 4.3 lattice mismatch of some oxides, which are used as buffer layers in the coated conductor development with YBCO and Ni are given. As seen from Table 4.3 some of the oxides have very close lattice match with YBCO but there is no natural material that

100% lattice matches with YBCO. Eliminating even small lattice mismatch might enable one to grow thicker (5 μm and up) YBCO layers without compromising the texture quality and hence J_c . By designing a 100% lattice match buffer layer, elimination of interfacial bond straining between the buffer layer and YBCO was intended in this study. Because in heteroepitaxy systems, depending on the extent of the mismatch, three distinct epitaxial regimes forms as they were visualized in Figure 4.20, and structure of the interface greatly influence the properties of the film. If the lattice mismatch is very small, the interfacial structure can be homoepitaxy as seen in Figure 4.20(a). However, the differences in the properties of two materials like thermal expansion coefficients and chemistry could strongly influence electronic properties and the perfection of interface. When the two materials' lattice parameters differ significantly either the two lattices strain to accommodate their differences which is called strained-layer heteroepitaxy as seen in Figure 4.20(b) or defects like edge dislocations form at the interface which is called relaxed epitaxy as seen in Figure 4.20(c) [94].

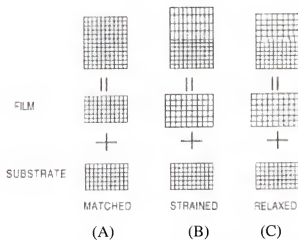


Figure 4.20. Schematic illustration of heteroepitaxial structures. A) Lattice-matched. B) Strained. C) Relaxed [94].

The lattice matching between the buffer layer and YBCO determine the quality of epitaxial growth of YBCO, and it has been known that initial stage of epitaxial growth strongly depends on interfacial strain. Effect of interfacial strain on superconducting properties of YBCO ultra thin films have been studied by deposition of YBCO thin films on different single crystals, which were LaAlO_3 (LAO) and SrTiO_3 (STO) [176]. The lattice constant of STO is ($a = 3.905 \text{ \AA}$) a little larger than that of $\text{YBa}_2\text{Cu}_3\text{O}_7$ ($a = 3.824 \text{ \AA}$, $b = 3.886 \text{ \AA}$), and the lattice constant of LAO is ($a = 3.788 \text{ \AA}$) a little smaller than that of YBCO. It was found that tensile strain occurs when c-axis oriented YBCO films grown on STO, while compressive strain occurs when YBCO films deposited on LAO, and different critical temperatures were reported for LAO and STO depending upon YBCO film thickness [176]. Improvements on critical currents of YBCO coated conductors have also been reported when YBCO thin films were deposited on small lattice mismatch buffer layers. To design a 100% lattice match buffer layer with YBCO, Eu_2O_3 and Yb_2O_3 were chosen from Table 4.3 because pseudocubic lattice parameter of Eu_2O_3 is bigger than lattice parameter of YBCO, and pseudocubic lattice parameter of Yb_2O_3 is smaller than lattice parameter of YBCO. The aims of the present work are (i) to investigate solid solubility of Eu_2O_3 and Yb_2O_3 , in each other and find a stoichiometric solid solution, the lattice parameter of which will be the same as the lattice parameter of YBCO, (ii) to study textured growth of solid solution on biaxially textured Ni substrate. The X-ray diffraction patterns obtained from the powder samples of $(\text{Eu}_{1-u}\text{Yb}_u)_2\text{O}_3$, for $u = 0, 0.1, 0.2, 0.5, 0.8, 0.9$, and 1 , are shown in Figure 4.21. All the XRD patterns looks similar and no extra or split peaks corresponding to the individual elements or any other secondary crystalline phases. This indicates that all seven samples belong to

the same crystal system, and all of them are single phase. Single phase solid solutions are obtained over the whole range of “*u*”. The clear shift in peak positions toward higher diffraction angles indicates a decrease in the lattice parameter, as the composition “*u*” increases, and the increase in intensity is attributed to the higher atomic scattering factor of Yb, with respect to that of Eu. The intensity of the X-ray diffracted beam is given by Eq. (4.1) [66],

$$I = |F|^2 p \left(\frac{1 + \cos^2 2\theta}{\sin^2 \theta \cos \theta} \right) e^{-2M} \quad (4.1)$$

where,

I = intensity of diffracted beam (arbitrary units)

F = structure factor,

p = multiplicity factor,

θ = Bragg angle

e^{-2M} = temperature factor

As it can be seen from the Eq. (4.1), the intensity of the X-ray diffracted beam is directly proportional to the structure factor, and the structure factor is given by Eq. (4.2) [66]

$$F_{hkl} = \sum_1^N f_n e^{2\pi i(hu_n + kv_n + lw_n)} \quad (4.2)$$

where,

F = structure factor,

N = number of atoms in a unit cell

f = atomic scattering factor

u, *v*, *w* = coordinates of each atom

The structure factor (*F*) is also directly proportional to atomic scattering factor, and the atomic scattering factor (*f*) increase with increasing atomic number of elements [66].

Since the atomic number of Yb is higher than that of Eu, the intensity of diffracted beam from (Eu_{1-*u*}Yb_{*u*})₂O₃ increase with increasing “*u*” in the composition.

The accurate peak positions were obtained by accurate profile fitting which was used to determine the precise lattice parameter “a” through a non-linear least squares procedure applying regression diagnostics [161], which allow the refinement of the zero

Table 4.3. Some of the physical properties and lattice mismatches of selected oxides with Ni and YBCO [177].

Oxides & Ni	Lattice Parameters		% Lattice Mismatch		M.P. (°C)
	Lattice parameter a (°Å)	Pseudocubic $a/2\sqrt{3}$ (°Å)	vs. Ni	vs. YBCO	
YBCO	3.82	-	7.85	-	
Ni	3.52	-	-	7.85	1449
Y ₂ O ₃	10.604	3.750	6.22	-1.89	2410
Er ₂ O ₃	10.548	3.730	5.69	-2.42	2400
Yb ₂ O ₃	10.436	3.690	4.61	-3.50	2227
Lu ₂ O ₃	10.390	3.674	4.17	-3.93	2487
Ho ₂ O ₃	10.606	3.750	6.22	-1.89	2360
Tb ₂ O ₃	10.730	3.794	7.39	-0.72	2340
Tm ₂ O ₃	10.487	3.708	5.09	-3.01	2425
Dy ₂ O ₃	10.665	3.771	6.78	-1.33	2340
Gd ₂ O ₃	10.813	3.824	8.17	0.07	2330
La ₂ O ₃	11.327	4.005	12.78	4.69	2307
Sm ₂ O ₃	10.927	3.864	9.21	1.11	2300
Eu ₂ O ₃	10.868	3.843	8.64	0.54	2291
Nd ₂ O ₃	11.080	3.918	10.59	2.50	2272
CeO ₂	5.412	-	8.69	0.13	2400
YSZ	5.14	-	3.3	-4.8	2700
SrTiO ₃	3.91	-	11.1	2.3	2353
BaTiO ₃	3.99	-	13.3	4.5	1625
MgO	4.22	-	19.8	10.5	2825
LaAlO ₃	3.79	-	7.7	-0.7	2453

shift. The lattice parameters obtained from this analysis are shown in Figure 4.22 for varying “u” values. Lattice parameters of (Eu_{1-u}Yb_u)₂O₃ is also given in Table 4.4. Lattice parameters of mixed (Eu_{1-u}Yb_u)₂O₃ oxides were changed between 10.868 Å and 10.428 Å, which are lattice parameter of Eu₂O₃ and Yb₂O₃, respectively, by changing the

ratio of Eu/Yb in the composition.

As shown in Figure 4.22 the variation of the lattice parameter (a) with the composition “ u ” is not linear, i.e., and it does not obey Vegard’s law [66, 178]. However, the nonlinearity is not much where the parameters of the second-degree polynomial could be fitted to the data. Lattice parameter analysis revealed that pseudocubic lattice parameter of $(\text{Eu}_{0.893}\text{Yb}_{0.107})_2\text{O}_3$ is 3.82 \AA , which is same as the lattice parameter of YBCO; the “ u ” value was determined to be 0.107 from the Figure 4.22.

The solution of $(\text{Eu}_{0.893}\text{Yb}_{0.107})_2\text{O}_3$ buffer layers were prepared as described in the experimental section, and a series of experiments at various solution concentrations and substrate’s withdrawal speeds were done to find processing conditions of continuous, crack free and textured buffer layers. Cation concentration of the solution was adjusted by methanol, and 4 different solution concentrations like 0.025, 0.05, 0.1 and 0.15 M were

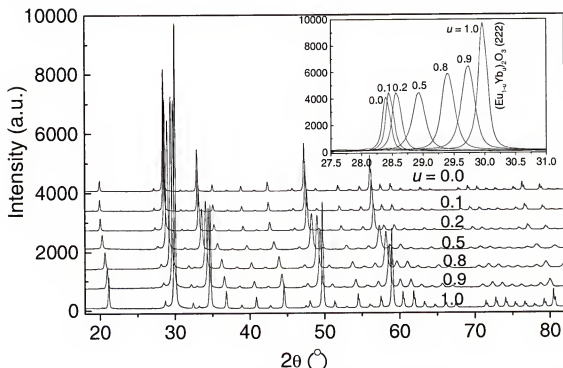


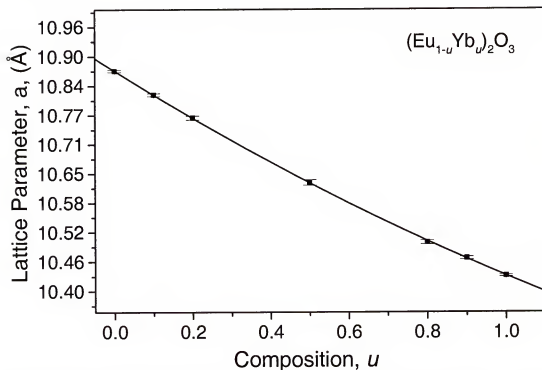
Figure 4.21. The X-ray diffraction patterns of the powder samples of $(\text{Eu}_{1-u}\text{Yb}_u)_2\text{O}_3$ for varying “ u ” values as marked.

Table 4.4. Lattice parameters of $(\text{Eu}_{1-u}\text{Yb}_u)_2\text{O}_3$ for varying “ u ” values.

Materials	Lattice Parameter (Å)
Eu_2O_3	10.868
$(\text{Eu}_{0.9}\text{Yb}_{0.1})_2\text{O}_3$	10.817
$(\text{Eu}_{0.8}\text{Yb}_{0.2})_2\text{O}_3$	10.767
$(\text{Eu}_{0.5}\text{Yb}_{0.5})_2\text{O}_3$	10.628
$(\text{Eu}_{0.2}\text{Yb}_{0.8})_2\text{O}_3$	10.499
$(\text{Eu}_{0.1}\text{Yb}_{0.9})_2\text{O}_3$	10.465
Yb_2O_3	10.428

$$\text{Pseudocubic lattice parameter} = \frac{a}{2\sqrt{2}},$$

where “ a ” is the lattice parameter.

Figure 4.22. Variation of the lattice parameter of $(\text{Eu}_{1-u}\text{Yb}_u)_2\text{O}_3$ for varying “ u ” values.

prepared, and various withdrawal speeds such as 0.25, 0.5, 1, 1.5 and 1.8 cm/s were used to find appropriate withdrawal speed for the buffer layers. At low solution concentrations like 0.025 M non-continuous films were obtained which are seen in Figure 4.23. Slow

withdrawal speeds also caused non-continuous microstructure, because most of the solution returned back to the solution tank before drying on the substrate as observed in the processing of CeO_2 buffer layers. On the other hand randomly orientated films were obtained from 0.15 M solutions after the annealing process. However, no crack formation was observed in $(\text{Eu}_{0.893}\text{Yb}_{0.107})_2\text{O}_3$ unlike CeO_2 . 0.1 M precursor solution with 1.0 cm/s withdrawal speed was used to deposit $(\text{Eu}_{0.893}\text{Yb}_{0.107})_2\text{O}_3$ on biaxially textured Ni substrate. Randomly oriented films which were deposited using 0.15 M solutions and 1-1.5 cm/s withdrawal speeds could be explained by deposition of thicker films per coating process, because majority of the solution stay on the substrate while the substrate entering the three zone furnace.

The samples were annealed at various annealing temperatures and time ranging from 900 °C to 1170 °C, and from 10 minutes to 1hour, respectively, under forming gas atmosphere (5 cc/min.). 900 °C/hour heating rate was used for annealing process, and XRD $\theta/2\theta$ scan is used to check texture quality. X-ray $\theta/2\theta$ scans of $(\text{Eu}_{0.893}\text{Yb}_{0.107})_2\text{O}_3$ buffer layers on biaxially textured Ni substrate, which were annealed at 900 °C for 30 min., 1000 °C for 30 min., 1050 °C for 30 min. and 1150 °C for 10 min. are seen in Figure 4.24. The XRD patterns of $(\text{Eu}_{0.893}\text{Yb}_{0.107})_2\text{O}_3$ buffer layers, which were deposited by chemical solution deposition of precursor solutions were also revealed a pure $(\text{Eu}_{0.893}\text{Yb}_{0.107})_2\text{O}_3$ phase. (222) and (400) peaks are in the XRD of the two samples, which were annealed at 900 and 1000 °C for 30 minutes. However, only (400) peak at 33.06° were present in the XRD of the samples, which were annealed at 1050 and 1150 °C. This is an indication of good out-of-plane alignment of $(\text{Eu}_{0.893}\text{Yb}_{0.107})_2\text{O}_3$ thin film on Ni(100) substrate, further texture analysis need to be done for full texture

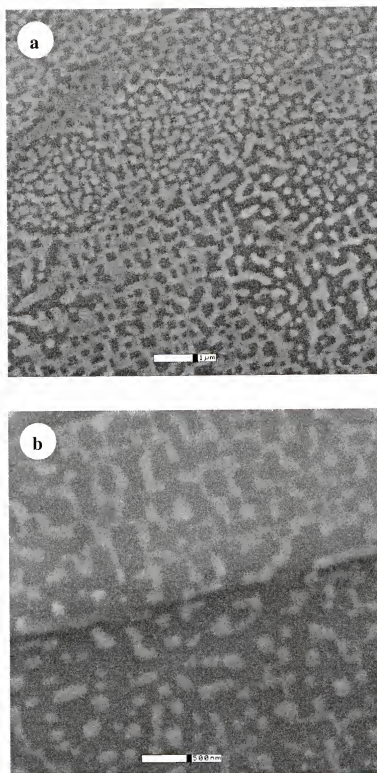


Figure 4.23. Surface morphologies of non-continuous $(\text{Eu}_{0.893}\text{Yb}_{0.107})_2\text{O}_3$ films, which was processed from 0.05 M precursor solution, on biaxially textured Ni substrate. The white scale bars of (a) and (b) are 1 μm and 500 nm, respectively.

characterization. In Figure 4.25 the logarithmic scale and background corrected (222) pole figure of $(\text{Eu}_{0.893}\text{Yb}_{0.107})_2\text{O}_3$ buffer layer, which was annealed at 1150 °C for

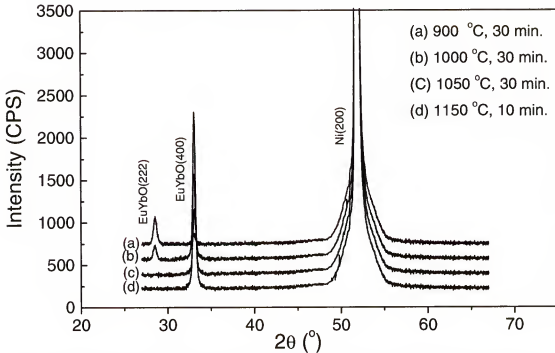


Figure 4.24. The X-ray $\theta/2\theta$ scans of $(\text{Eu}_{0.893}\text{Yb}_{0.107})_2\text{O}_3$ buffer layers, which were annealed at varying temperatures and times, on biaxially textured Ni substrate.

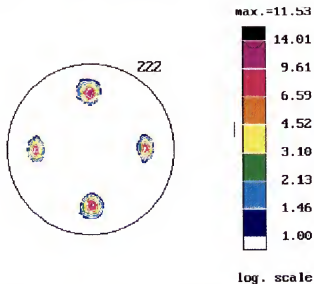


Figure 4.25. The logarithmic scale and background corrected (222) pole figure of $(\text{Eu}_{0.893}\text{Yb}_{0.107})_2\text{O}_3$ buffer layer, which was annealed at 1150 °C for 10 min., on biaxially textured Ni substrate.

10 minutes, is seen. A four-fold symmetry is clearly seen, which is an indication of cube texture, $[16]\langle 001 \rangle$, in the buffer layers. The (222) poles are rotated 45° with respect to the (111) poles of Ni. That means (400) crystallographic planes of $(\text{Eu}_{0.893}\text{Yb}_{0.107})_2\text{O}_3$ are parallel to the substrate, the [002] axis of $(\text{Eu}_{0.893}\text{Yb}_{0.107})_2\text{O}_3$ buffer layers is 45° rotated from the rolling direction of Ni substrate as reported. The cube texture relationship between $(\text{Eu}_{0.893}\text{Yb}_{0.107})_2\text{O}_3$ buffer layer and Ni substrate can be symbolized as follows: $(\text{Eu}_{0.893}\text{Yb}_{0.107})_2\text{O}_3$ [002]//Ni [001] and $(\text{Eu}_{0.893}\text{Yb}_{0.107})_2\text{O}_3$ [220]//Ni [100].

The results of out-of-plane and in-plane texture analyses of $(\text{Eu}_{0.893}\text{Yb}_{0.107})_2\text{O}_3$ buffer layers, which were annealed at 1050°C for 30 min., 1150°C for 10 and 30 min., 1170°C for 30 min. were seen in Table 4.5. FWHMs of ω and ϕ - scans of $(\text{Eu}_{0.893}\text{Yb}_{0.107})_2\text{O}_3$, which was annealed at 1150°C for 30 minutes are smaller than that of $(\text{Eu}_{0.893}\text{Yb}_{0.107})_2\text{O}_3$, which was annealed at 1050°C for 30 minutes. It means that out-of-plane and in-plane alignments increase with increasing annealing temperature. However, there was hardly any difference in the FWHMs of ω and ϕ - scans of $(\text{Eu}_{0.893}\text{Yb}_{0.107})_2\text{O}_3$, which were annealed 1150°C , 10 min. and 1170°C , 30 min. Therefore, 1150°C , 10 minutes was chosen as an appropriate annealing condition. Divergence of the out-of-plane orientation of $(\text{Eu}_{0.893}\text{Yb}_{0.107})_2\text{O}_3$ (400) planes is seen in Figure 4.26. The FWHM values of Ni (200) substrate under the buffer layer and $(\text{Eu}_{0.893}\text{Yb}_{0.107})_2\text{O}_3$ are 6.61° and 7.25° , respectively. Low FWHM values of the ω - scans of the Ni substrate and the buffer layer showed that high degree out-of-plane alignments were present.

The ϕ -scan of (222) plane of the $(\text{Eu}_{0.893}\text{Yb}_{0.107})_2\text{O}_3$ buffer layer is seen in Figure 4.27, and the FWHMs are 7.80° and 7.79° for Ni (111) and $(\text{Eu}_{0.893}\text{Yb}_{0.107})_2\text{O}_3$ (222), respectively. The strong and narrow peaks suggest that both Ni substrate and buffer layer

have good in-plane texture. These FWHM values are similar or smaller than those of the buffer layers, which were chemical solution deposited [17, 18, 151].

Table 4.5. FWHM values of ω and ϕ - scans of Ni and $(\text{Eu}_{0.893}\text{Yb}_{0.107})_2\text{O}_3$ buffer layers, which were annealed at varying conditions.

Materials	Annealing Conditions	ω - scan ($^\circ$)	ϕ - scan ($^\circ$)
Ni	1050 $^\circ\text{C}$, 30 min.	6.61	7.80
$(\text{Eu}_{0.893}\text{Yb}_{0.107})_2\text{O}_3$	1050 $^\circ\text{C}$, 30 min.	7.95	10.28
$(\text{Eu}_{0.893}\text{Yb}_{0.107})_2\text{O}_3$	1150 $^\circ\text{C}$, 10 min.	7.25	7.79
$(\text{Eu}_{0.893}\text{Yb}_{0.107})_2\text{O}_3$	1150 $^\circ\text{C}$, 30 min.	7.13	7.65
$(\text{Eu}_{0.893}\text{Yb}_{0.107})_2\text{O}_3$	1170 $^\circ\text{C}$, 30 min.	7.09	7.63

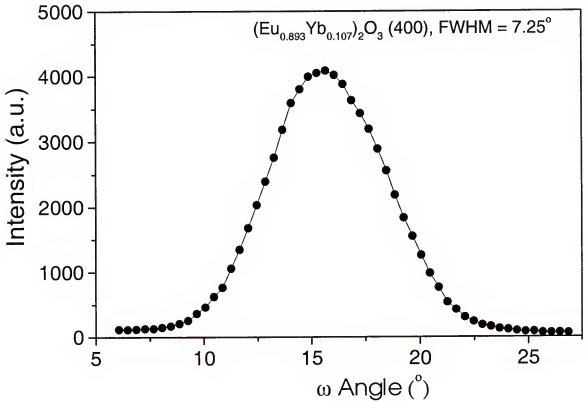


Figure 4.26. The ω - scan of biaxially textured $(\text{Eu}_{0.893}\text{Yb}_{0.107})_2\text{O}_3$ buffer layer, which was annealed at 1150 $^\circ\text{C}$ for 10 min., on biaxially textured Ni substrate.

Texture uniformity of $(\text{Eu}_{0.893}\text{Yb}_{0.107})_2\text{O}_3$ buffer layers over the 10 cm is seen in Figure 4.28. Three pieces of 10 cm long $(\text{Eu}_{0.893}\text{Yb}_{0.107})_2\text{O}_3$ samples were analyzed in the same way as CeO_2 buffer layers were analyzed. Again, the samples were coated and

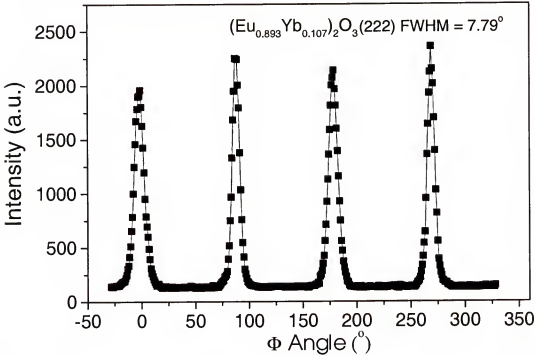


Figure 4.27. The ϕ - scan of biaxially textured $(\text{Eu}_{0.893}\text{Yb}_{0.107})_2\text{O}_3$ buffer layer, which was annealed at 1150 °C for 10 min., on biaxially textured Ni substrate.

annealed at the same conditions. The measurements were repeated every 1 cm intervals to cover the entire tape length, and a total of 30 ω and ϕ - scan data were collected. As seen from the Figure 4.28 well textured and uniform $(\text{Eu}_{0.893}\text{Yb}_{0.107})_2\text{O}_3$ buffer layers were deposited over the 10 cm long biaxially textured Ni substrate by using the chemical solution deposition technique.

Out-of-plane and in-plane textures of $(\text{Eu}_{0.893}\text{Yb}_{0.107})_2\text{O}_3$ buffer layers were investigated for multiple coated samples. In Table 4.6 FWHMs of ω and ϕ - scans of the Ni substrate and 5 times dip coated buffer layers are seen. The buffer layers were annealed after coating. The out-of-plane texture was improved with repeating the coating

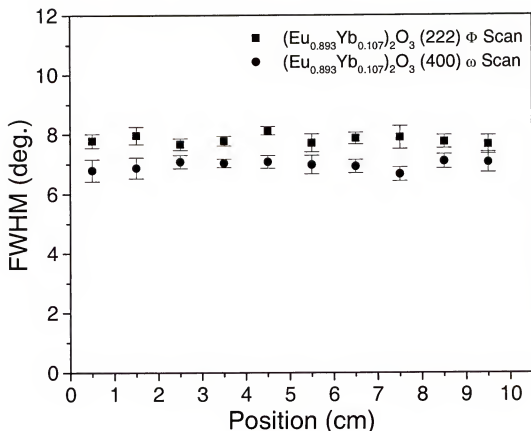


Figure 4.28. FWHM values of ω and ϕ - scans of 10 cm long biaxially textured $(\text{Eu}_{0.893}\text{Yb}_{0.107})_2\text{O}_3$ buffer layer, which was annealed at 1150 °C for 10 min., on biaxially textured Ni substrate.

Table 4.6. FWHM values of ω and ϕ - scans of Ni and $(\text{Eu}_{0.893}\text{Yb}_{0.107})_2\text{O}_3$ buffer layers, which were coated 5 times with dip coating process.

Materials	Annealing Conditions	ω - scan (°)	ϕ - scan (°)
Ni	1050 °C, 30 min.	6.61	7.80
$(\text{Eu}_{0.893}\text{Yb}_{0.107})_2\text{O}_3$ 1 dip	1150 °C, 10 min.	7.25	7.79
$(\text{Eu}_{0.893}\text{Yb}_{0.107})_2\text{O}_3$ 2 dip	1150 °C, 10 min.	7.19	7.85
$(\text{Eu}_{0.893}\text{Yb}_{0.107})_2\text{O}_3$ 3 dip	1150 °C, 10 min.	6.71	7.94
$(\text{Eu}_{0.893}\text{Yb}_{0.107})_2\text{O}_3$ 4 dip	1150 °C, 10 min.	6.81	7.67
$(\text{Eu}_{0.893}\text{Yb}_{0.107})_2\text{O}_3$ 5 dip	1150 °C, 10 min.	6.45	7.70

process, however, almost no changes were observed in in-plane texture. X-ray $\theta/2\theta$ scans of $(\text{Eu}_{0.893}\text{Yb}_{0.107})_2\text{O}_3$ buffer layers were also taken to monitor the (222) random peak, and no (222) oriented grains were observed from the 5 times coated samples. Further increasing the number of coating process cause cracks near the edges of substrate. In Figure 4.29 X-ray $\theta/2\theta$ scans of $(\text{Eu}_{0.893}\text{Yb}_{0.107})_2\text{O}_3$ buffer layer, which were dip coated multiple times, is seen. To shorten the $\theta/2\theta$ scans' time only between 27° and 35° were scanned. This range is good enough to check the texture of samples because the Bragg angle of (222) and (400) planes are about 28.5° and 33° , respectively.

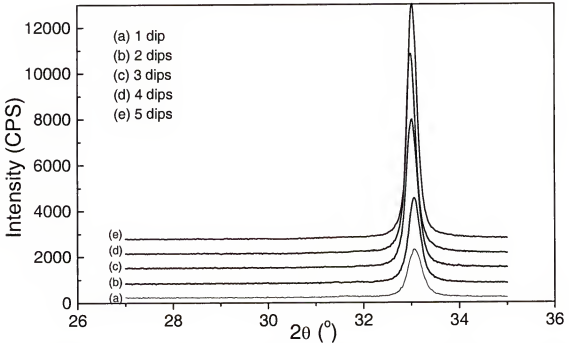


Figure 4.29. The X-ray $\theta/2\theta$ scan of $(\text{Eu}_{0.893}\text{Yb}_{0.107})_2\text{O}_3$ buffer layers which were dip coated multiple times as marked.

Thickness of the film was determined using a Tencor profilometer to be 120 nm. Homogeneous, dense, smooth, crack-free and pinhole-free micrographs are seen in Figure 4.30(a) and (b). $(\text{Eu}_{0.893}\text{Yb}_{0.107})_2\text{O}_3$ buffer layers also followed surface morphology of the Ni substrate, therefore, grain boundaries and grain boundary triple junctions of the

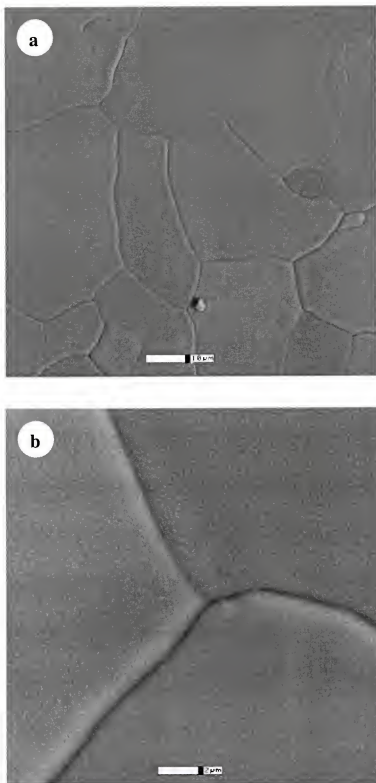


Figure 4.30. Surface morphologies of biaxially textured $(\text{Eu}_{0.893}\text{Yb}_{0.107})_2\text{O}_3$ films on biaxially textured Ni substrate. The white scale bars of (a) and (b) are 10 μm and 2 μm , respectively.

Ni substrate are seen in Figure 4.30(a) and (b). All the results showed that highly textured, dense, smooth and crack-free buffer layers, which have no lattice mismatch to YBCO can be synthesized via a wet-chemical method.

4.4 Multi Buffer Layers Structures

Cube textured growth of CeO_2 and $(\text{Eu}_{0.893}\text{Yb}_{0.107})_2\text{O}_3$ buffer layers have been demonstrated on biaxially textured Ni substrates by chemical solution deposition technique. However, CeO_2 buffer layer is also used as a cap layer underneath the YBCO superconducting films. $(\text{Eu}_{0.893}\text{Yb}_{0.107})_2\text{O}_3$ buffer layers is designed as a cap layer because there is no lattice mismatch between $(\text{Eu}_{0.893}\text{Yb}_{0.107})_2\text{O}_3$ and YBCO. Therefore texture growth of CeO_2 and $(\text{Eu}_{0.893}\text{Yb}_{0.107})_2\text{O}_3$ have to be investigated on an oxide layer. Since Gd_2O_3 buffer layers were readily available in our laboratory, CeO_2 buffer layer was deposited on Gd_2O_3 buffer layers, which was grown on biaxially textured Ni substrate by chemical solution dip coating method. Then $(\text{Eu}_{0.893}\text{Yb}_{0.107})_2\text{O}_3$ buffer layer was coated on $\text{CeO}_2/\text{Gd}_2\text{O}_3$ buffer layers structure using the same dip coating system. Out-of-plane and in-plane texture analysis of Gd_2O_3 buffered Ni substrate were examined before deposition of CeO_2 buffer layers. FWHMs of ω and ϕ - scans of Gd_2O_3 were found to be 6.35° and 7.97° , respectively. The results of texture analysis show that chemical solution deposited Gd_2O_3 have highly textured structure, and it is expected to constructively affect to the texture of CeO_2 buffer layers. The same coating and annealing conditions, which were used to deposit CeO_2 and $(\text{Eu}_{0.893}\text{Yb}_{0.107})_2\text{O}_3$ on Ni were chosen. Out-of-plane and in-plane textures of $\text{CeO}_2/\text{Gd}_2\text{O}_3$ structure have been examined after annealing of CeO_2 buffer layers at 1150°C for 10 min. under reducing gas atmosphere. The ω - scan of $\text{CeO}_2/\text{Gd}_2\text{O}_3$ is seen in Figure 4.31. The theoretical 2θ angle of CeO_2 (200) and Gd_2O_3

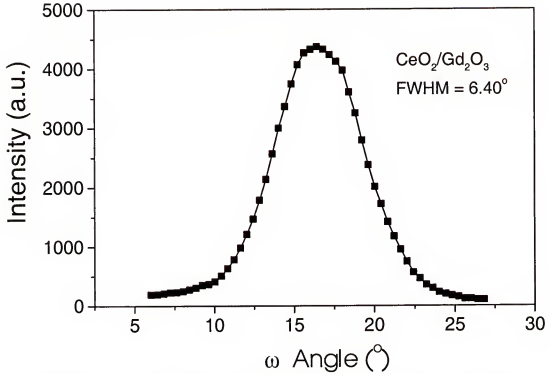


Figure 4.31. The ω - scan of $\text{CeO}_2/\text{Gd}_2\text{O}_3$ buffer layer structure, which was annealed at 1150°C for 10 min., on biaxially textured Ni substrate.

(400) are 33.075° and 33.185° , respectively. Since they almost overlap, and by considering interaction volume of X-ray beam, the diffracted X-ray beams come from both CeO_2 and Gd_2O_3 buffer layers and represent out-of-plane texture of $\text{CeO}_2/\text{Gd}_2\text{O}_3$ structure. FWHM of the ω - scan is 6.40° , which indicates highly textured $\text{CeO}_2/\text{Gd}_2\text{O}_3$ buffer layer structure. The ϕ - scan of $\text{CeO}_2/\text{Gd}_2\text{O}_3$ structure is seen in Figure 4.32. Since 2θ angle of CeO_2 (111) and Gd_2O_3 (222) almost overlap, the figure represents the in-plane texture of $\text{CeO}_2/\text{Gd}_2\text{O}_3$ structure.

Elemental analysis, and surface morphology of the structure were investigated by ESEM with an EDS attachment. Cerium and Gadolinium peaks are clearly seen from the Figure 4.33, which is the EDS spectroscopy of $\text{CeO}_2/\text{Gd}_2\text{O}_3$ /Ni buffer layers structure. Since the beryllium window is present in the EDS detector low atomic number elements

like oxygen cannot be detected. The Ni peak in the spectrum is coming from the substrate. All texture and microstructure analysis show that the textured CeO_2 buffer layer can be grown on Gd_2O_3 buffer layer film by chemical solution deposition process.

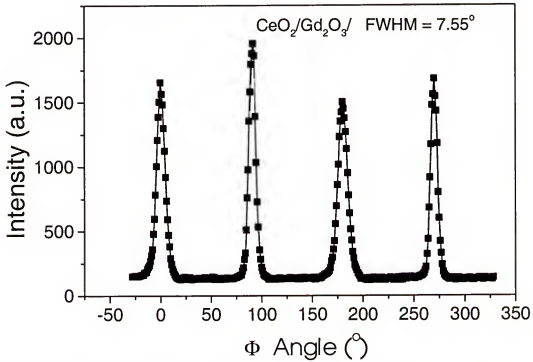


Figure 4.32. The ϕ - scan of $\text{CeO}_2/\text{Gd}_2\text{O}_3$ buffer layer structure, which was annealed at 1150°C for 10 min., on biaxially textured Ni substrate.

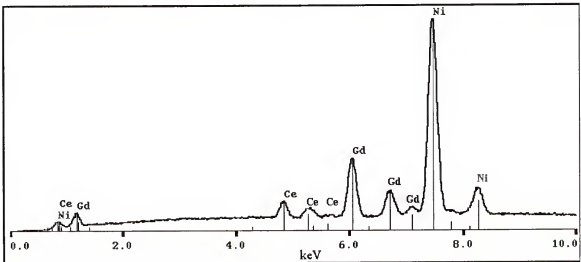


Figure 4.33. EDS spectrum of $\text{CeO}_2/\text{Gd}_2\text{O}_3$ buffer layers structure and the Ni substrate.

Plane view ESEM micrographs of $\text{CeO}_2/\text{Gd}_2\text{O}_3/\text{Ni}$ structure are seen in Figure 4.34(a) and (b). The microstructure is free from cracks and pinholes, and the structure follows surface morphology of the Ni substrate. As a final step $(\text{Eu}_{0.893}\text{Yb}_{0.107})_2\text{O}_3$ was coated on $\text{CeO}_2/\text{Gd}_2\text{O}_3/\text{Ni}$. Even though there is a small lattice mismatch between CeO_2 and YBCO, I wanted to grow a %100 lattice match buffer layer with YBCO on CeO_2 to show that the $(\text{Eu}_{0.893}\text{Yb}_{0.107})_2\text{O}_3$ buffer layer can be grown on an oxide buffer layer. 100% lattice match buffer layers could improve epitaxial growth of thick YBCO films ($\sim 5 \mu\text{m}$ and up), which is desirable for high power applications.

Figure 4.35 shows out-of-plane texture of $(\text{Eu}_{0.893}\text{Yb}_{0.107})_2\text{O}_3/\text{CeO}_2/\text{Gd}_2\text{O}_3$ three buffer layers structure. The 2θ angles of all three buffer layers almost overlap; therefore, the figure represents the texture of three buffer layers structure. Same thing is also true for in-plane texture analysis of the structure. The FWHM of the ω - scan of $(\text{Eu}_{0.893}\text{Yb}_{0.107})_2\text{O}_3/\text{CeO}_2/\text{Gd}_2\text{O}_3$ is 6.67° , which is highly acceptable especially for chemical solution deposited thin films, growth mechanism of which is totally different than that of thin films deposited by vacuum techniques. The FWHM of in-plane texture of $(\text{Eu}_{0.893}\text{Yb}_{0.107})_2\text{O}_3/\text{CeO}_2/\text{Gd}_2\text{O}_3$ is 7.83° , which is an indication of highly textured structure, as seen from Figure 4.36.

In Figure 4.37 the EDS spectrum of the $(\text{Eu}_{0.893}\text{Yb}_{0.107})_2\text{O}_3/\text{CeO}_2/\text{Gd}_2\text{O}_3$ buffer layers structure is seen. Ni, Gd, Ce, Eu and Yb peaks were observed from the spectrum. Yb and Ni peaks overlap at the high energy level but at the low energy level they are separable. Eu and Gd peaks partially overlap. Surface morphology of $\text{Gd}_2\text{O}_3/\text{CeO}_2/(\text{Eu}_{0.893}\text{Yb}_{0.107})_2\text{O}_3$ was investigated by ESEM and micrographs are seen in Figure 4.38(a) and (b). The micrographs show that $(\text{Eu}_{0.893}\text{Yb}_{0.107})_2\text{O}_3/\text{CeO}_2/\text{Gd}_2\text{O}_3$ buffer

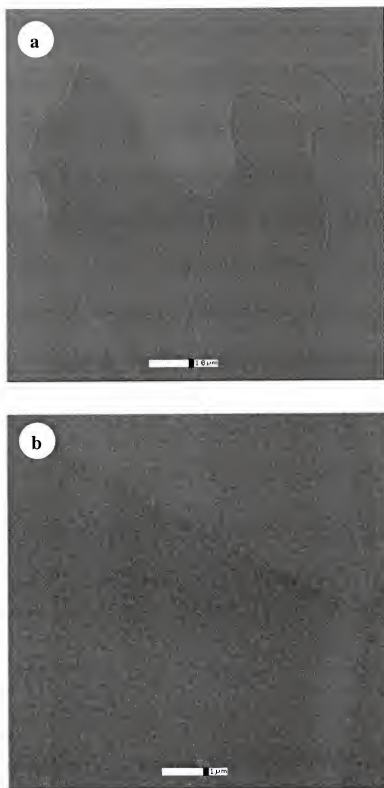


Figure 4.34. ESEM micrographs of $\text{CeO}_2/\text{Gd}_2\text{O}_3$ buffer layers structure on biaxially textured Ni substrate. The white scale bars are 10 μm and 1 μm in (a) and (b), respectively.

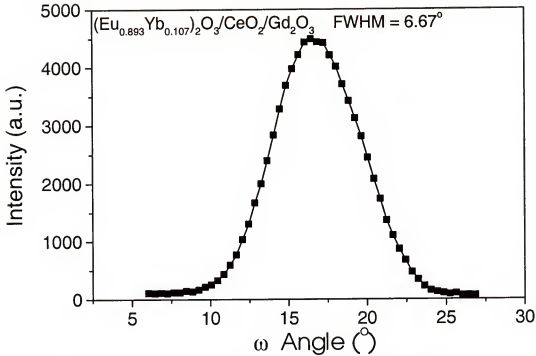


Figure 4.35. The ω - scan of $(\text{Eu}_{0.893}\text{Yb}_{0.107})_2\text{O}_3/\text{CeO}_2/\text{Gd}_2\text{O}_3$ buffer layers structure, which was annealed at 1150°C for 10 min., on biaxially textured Ni substrate.

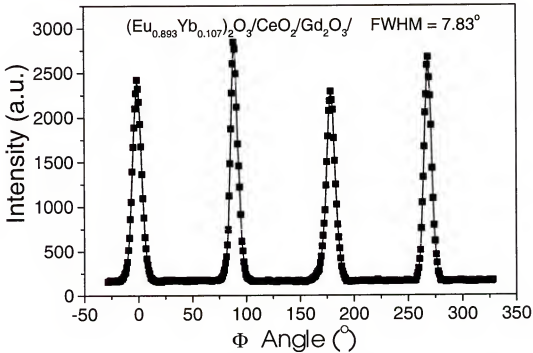


Figure 4.36. The ϕ - scan of $(\text{Eu}_{0.893}\text{Yb}_{0.107})_2\text{O}_3/\text{CeO}_2/\text{Gd}_2\text{O}_3$ buffer layers structure, which was annealed at 1150°C for 10 min., on biaxially textured Ni substrate.

layers structure can be grown crack free and pin hole free by the chemical solution deposition technique. The morphology of grain grooves of the Ni substrate is still seen after the coatings of $(\text{Eu}_{0.893}\text{Yb}_{0.107})_2\text{O}_3/\text{CeO}_2/\text{Gd}_2\text{O}_3$ buffer layers structure. As it can be seen from the Table 4.7 FWHM values of ω and ϕ - scans of all buffer layers structures and Ni substrate are very close to each other. The quality of out-of-plane and in-plane textures could be limited with the texture quality of Ni substrate. The microstructure and

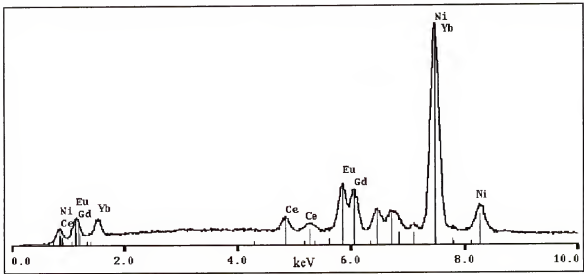


Figure 4.37. EDS spectrum of $(\text{Eu}_{0.893}\text{Yb}_{0.107})_2\text{O}_3/\text{CeO}_2/\text{Gd}_2\text{O}_3$ buffer layers structure and Ni substrate.

Table 4.7. FWHM values of ω and ϕ - scans of Ni, $\text{Gd}_2\text{O}_3/\text{Ni}$, $\text{CeO}_2/\text{Gd}_2\text{O}_3/\text{Ni}$ and $(\text{Eu}_{0.893}\text{Yb}_{0.107})_2\text{O}_3/\text{CeO}_2/\text{Gd}_2\text{O}_3/\text{Ni}$ buffer layers structures.

Materials	Annealing Conditions	ω - scan ($^\circ$)	ϕ - scan ($^\circ$)
Ni	1050 $^\circ\text{C}$, 30 min.	6.62	7.85
$\text{Gd}_2\text{O}_3/\text{Ni}$	1150 $^\circ\text{C}$, 10 min.	6.35	7.97
$\text{CeO}_2/\text{Gd}_2\text{O}_3/\text{Ni}$	1150 $^\circ\text{C}$, 10 min.	6.40	7.55
$(\text{Eu}_{0.893}\text{Yb}_{0.107})_2\text{O}_3/\text{CeO}_2/\text{Gd}_2\text{O}_3/\text{Ni}$	1150 $^\circ\text{C}$, 10 min.	6.67	7.83

texture analysis showed that crack free, pinhole free, and highly textured $\text{CeO}_2/\text{Gd}_2\text{O}_3$ and $(\text{Eu}_{0.893}\text{Yb}_{0.107})_2\text{O}_3/\text{CeO}_2/\text{Gd}_2\text{O}_3$ buffer layers structures can be deposited on biaxially textured Ni substrates by the chemical solution deposition. The FWHMs of out-of-plane and in-plane textures of the $\text{CeO}_2/\text{Gd}_2\text{O}_3$ structure are 6.40° and 7.55° , respectively. The FWHMs of out-of-plane and in-plane textures of the $(\text{Eu}_{0.893}\text{Yb}_{0.107})_2\text{O}_3/\text{CeO}_2/\text{Gd}_2\text{O}_3$ buffer layers structure are 6.67° and 7.83° , respectively. The thicknesses of CeO_2 and $(\text{Eu}_{0.893}\text{Yb}_{0.107})_2\text{O}_3$ were built up by repeating the coating process. The average total thickness of the buffer layers is about 150 nm.

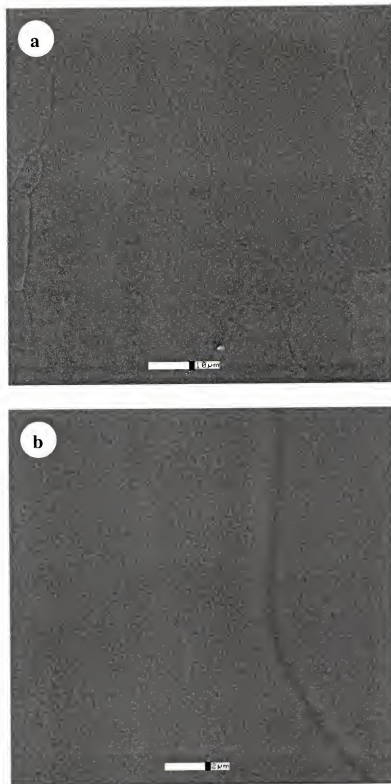


Figure 4.38. ESEM micrographs of $\text{Eu}_{0.893}\text{Yb}_{0.107})_2\text{O}_3/\text{CeO}_2/\text{Gd}_2\text{O}_3$ buffer layers structure on biaxially textured Ni substrate. The white scale bars are 10 μm and 2 μm in (a) and (b), respectively.

CHAPTER 5 CONCLUSIONS

5.1. Conclusions

The primary goal of the research was to investigate development of buffer layers by chemical solution deposition on biaxially textured Ni substrates for YBCO coated conductors. As it was discussed before biaxially textured growth of buffer layers and/or YBCO on flexible metallic substrates by chemical solution deposition technique could make long length coated conductors available in the market with cheaper prices because of high throughput and inexpensive coating process. CeO_2 has been recognized as a one of the best cap layers for YBCO coated conductors, and has been coated on YSZ buffer layers successfully by vacuum techniques. Therefore investigation of chemical solution deposition of CeO_2 was chosen in this work. Before studying chemical solution deposition of CeO_2 buffer layers on Ni substrates, heat treatment conditions of cold rolled Ni substrate was established to form biaxially cube textured structure. Because cold rolled Ni substrates were the starting material in this research, and depending upon rolling conditions, Ni substrates require a unique heat treatment process to obtain cube textured structure. Biaxially textured substrates and/or biaxially textured buffer layers structures are necessary to facilitate epitaxial growth of YBCO layers. Highly out-of-plane and in-plane textured, and low angle grain boundaries in YBCO films are necessary because critical current density of the YBCO coated conductors are adversely affected from high angle grain boundaries. The heat treatment results of 99.99% pure Ni

substrates showed that highly cube textured structure were obtained at 1050 °C for 30 minutes under 4% H₂-Ar gas flow. Cold rolling process form some alignments of Ni grains, which is called “rolling texture”. There is no unique single orientation, however some degree of alignment is seen. Pole figure analysis of heat treated Ni substrates revealed that single phase cube texture structure was obtained. Quantitative texture analyses of the substrates were completed by X-ray omega and phi scans. FWHM of omega scan of (200) plane of Ni substrate of 6.90°, and FWHM of phi scan of (111) plane of Ni substrate of 8.12° are routinely achieved. These FWHM values and pole figures of the substrate showed that highly biaxially textured Ni substrates were obtained in house for chemical solution deposition. Texture uniformity 3 substrates, each of which was 10 cm long, was analyzed along the length. The measurements were repeated with 1cm intervals to cover the entire tape length, and a total of 30 ω and ϕ - scans data were collected. The results showed that reproducible and uniform texture over the length was obtained from the Ni substrates. Surface morphology studies of the substrates showed that very smooth surfaces, which are required for epitaxial growth of buffer layers, were obtained. However, grain boundary grooves are clearly seen from the ESEM micrographs. Basically these grooves are undesirable because they affect the surface morphology of buffer layers. On the other hand, they are unavoidable and no solution was proposed so far except polishing. Chemical and mechanical polishing of the substrates might be the solution, but annealed Ni is very soft and kinks and bends could easily be introduced to the substrates during the polishing. These kinks and bends might affect J_c of the conductor more severely than the grooves. Addition of some alloying elements to pure Ni increases mechanical properties of Ni substrates but also increases

surface roughness. It was reported that addition of vanadium to Ni reduces the grain boundary grooving.

Textured CeO_2 buffer layers were grown both on biaxially textured Ni substrates and Gd_2O_3 buffer layered Ni substrates as a seed and a cap layer, respectively, by chemical solution deposition technique. Lattice parameter of CeO_2 is very close to that of YBCO, and CeO_2 does not react with YBCO if it is deposited in the optimum thickness. Lattice parameter of CeO_2 is 0.13% bigger than that of YBCO along the a axis, and 1.54% smaller than that of YBCO when the CeO_2 basal plane is rotated 45° . X-ray $\theta/2\theta$ scan of CeO_2 buffer layer which was grown on biaxially textured Ni substrate showed highly out-of-plane textured structure, which was annealed at 1150°C for 10 minutes under 4% H_2 -Ar gas flow. Pole figure analysis of CeO_2 buffer layer confirmed that cube textured CeO_2 buffer layers were successfully grown on biaxially textured Ni substrates. FWHM of omega scan of (200) plane of CeO_2 is about 6.47° , and FWHM of phi scan of (111) plane of CeO_2 is about 7.42 . Texture uniformity of the CeO_2 buffer layers was also analyzed by taking ω and ϕ scans from three 10 cm long CeO_2 buffer layers which were annealed under the same conditions. A measurement was taken from every 1 cm of the 10 cm long sample, and the results showed that reproducible and uniform texture over the length was obtained. Highly textured, crack free and pin-hole free very smooth CeO_2 buffer layers were grown on Ni substrates in this research.

After successfully depositing highly textured CeO_2 buffer layers on Ni substrates, to eliminate the lattice mismatch between the buffer layer and YBCO, a new buffer layer, which is a mixture of Eu_2O_3 and Yb_2O_3 , was developed. Single phase solid solutions, $(\text{Eu}_{1-u}\text{Yb}_u)_2\text{O}_3$ were obtained from mixture of Eu_2O_3 and Yb_2O_3 . Lattice parameters of

mixed $(\text{Eu}_{1-u}\text{Yb}_u)_2\text{O}_3$ oxides were changed between 10.868 Å and 10.428 Å, which are the lattice parameters of Eu_2O_3 and Yb_2O_3 , respectively, by changing the ratio of Eu/Yb in the mixture. Pseudocubic lattice parameters of $(\text{Eu}_{0.893}\text{Yb}_{0.107})_2\text{O}_3$ were found to be 3.82 Å, which is also the lattice parameter (a) of YBCO. Highly textured $(\text{Eu}_{0.893}\text{Yb}_{0.107})_2\text{O}_3$ buffer layers were deposited on biaxially textured Ni substrates by chemical solution deposition technique. Interfacial strain because of lattice misfit was eliminated between $(\text{Eu}_{0.893}\text{Yb}_{0.107})_2\text{O}_3$ buffer layers and YBCO. Pole figure analysis showed that cube textured $(\text{Eu}_{0.893}\text{Yb}_{0.107})_2\text{O}_3$ were grown on the Ni substrates, and FWHM values of omega and phi scans were 6.45° and 7.70°, respectively. It was shown that highly textured and uniform $(\text{Eu}_{0.893}\text{Yb}_{0.107})_2\text{O}_3$ buffer layers can be coated on biaxially textured Ni substrates by the chemical solution deposition technique.

Since CeO_2 buffer layers are used as a seed and cap layer in the development of YBCO coated conductors, growth of CeO_2 on Gd_2O_3 buffer layers were investigated. FWHMs of ω and ϕ scans of Gd_2O_3 buffer layers were 6.35° and 7.97°, respectively. $\text{Gd}_2\text{O}_3/\text{CeO}_2$ buffer layer structure showed highly textured structure, and FWHMs of omega and phi scans of $\text{Gd}_2\text{O}_3/\text{CeO}_2$ were 6.40° and 7.55°, respectively. $(\text{Eu}_{0.893}\text{Yb}_{0.107})_2\text{O}_3$ buffer layer was also grown on $\text{Gd}_2\text{O}_3/\text{CeO}_2$ buffer layers structure and FWHMs of omega and phi scans of $\text{Gd}_2\text{O}_3/\text{CeO}_2/(\text{Eu}_{0.893}\text{Yb}_{0.107})_2\text{O}_3$ were 6.67° and 7.83°, respectively. Both buffer layer structures were crack-free, pin hole-free and had smooth microstructures.

5.2 Suggestions for Future Work

Having biaxially textured, crack-free and pin hole-free microstructures is a fundamental requirement for every buffer layer, which is used in fabrication of YBCO

coated conductors, and this current research demonstrated that biaxially textured, crack-free, and pin hole-free CeO_2 and $(\text{Eu}_{0.893}\text{Yb}_{0.107})_2\text{O}_3$ buffer layers were grown on pure Ni substrates and oxide buffer layers by chemical solution deposition technique. However, Ni alloys have been used for fabrication of YBCO coated conductors. These Ni-Cr, Ni-W, and Ni-V alloys have some advantages over the pure Ni substrates. Basically, their mechanical properties are better than pure Ni substrates, and this provides ease of handling of annealed substrates, and prevents formation of kinks and bends. Moreover, pure Ni substrate has ferromagnetic properties, and some applications of YBCO coated conductors require non-magnetic substrates. Growth of CeO_2 could be investigated on these substrates by chemical solution deposition technique. Generally, Ni alloys require higher annealing temperatures and longer time for formation of biaxial texture, and some problems might be faced during coating of buffer layer solutions. In the case of Ni-Cr alloys Cr sites oxidize faster than Ni; therefore all these issues need to be considered while depositing and annealing the buffer layers by chemical solution deposition technique. Buffer layer processing parameters might require some revision when Ni alloys are chosen as substrates. The FWHMs values of Ni and buffer layers were found very close to each other. By further improving out-of-plane and in-plane texture of Ni or Ni alloys substrates, lower FWHMs could be obtained from the buffer layers. Longer biaxially textured substrates could also be coated, because kilometer long coated conductors are needed for practical applications. A new chemical solution tank might be designed according to the width of substrate. Growth of CeO_2 and $(\text{Eu}_{0.893}\text{Yb}_{0.107})_2\text{O}_3$ on YSZ buffer layers should be studied. YSZ is recognized as one of the perfect diffusion barrier layers, but it has to be coated with a cap layer before YBCO deposition. YBCO

layer/layers could be deposited on these buffer layer structures. Performance of buffer layer structures may be monitored by measuring J_c of the conductor. Buffer layer structures might require optimization like changing the thickness of each layer.

In case there is an optimum lattice mismatch between the cap layer and the YBCO layer the lattice constant of the engineered buffer layer can be adjusted to that value. Or alternatively by continuously changing the lattice constant of the engineered buffer layer that optimum mismatch can be searched.

LIST OF REFERENCES

1. V. Z. Kresin and S. A. Wolf, *Fundamentals of Superconductivity* (Plenum Press, New York, 1990).
2. M. K. Wu, J. R. Ashburn, C. J. Torng, P. H. Hor, R. L. Meng, L. Gao, Z. J. Huang, Y. Q. Wang, and C. W. Chu, *Physical Review Letters* **58**, (9), 908-910 (1987).
3. K. Heine, J. Tenbrink, and M. Thoner, *Applied Physics Letters* **55**, (23), 2441-2443 (1989).
4. American Superconductors, 2003. News, <http://www.amsuper.com/>, (accessed March 2003).
5. Y. Iijima, K. Onabe, N. Futaki, N. Tanabe, N. Sadakata, O. Kohno, and Y. Ikeno, *Journal of Applied Physics* **74**, (3), 1905-1911 (1993).
6. M. Rupp, A. Gupta, and C. C. Tsuei, *Applied Physics Letters* **67**, (2), 291-293 (1995).
7. U.S. Department of Energy, 2003. Accelerated coated conductor initiative, http://www.eren.doe.gov/superconductivity/pdfs/acci_to_print.pdf, (accessed March 2003).
8. A. Goyal, D. P. Norton, J. D. Budai, M. Paranthaman, E. D. Specht, D. M. Kroeger, D. K. Christen, Q. He, B. Saffian, F. A. List, D. F. Lee, P. M. Martin, C. E. Klabunde, E. Hartfield, and V. K. Sikka, *Applied Physics Letters* **69**, (12), 1795-1797 (1996).
9. U.S. Department of Energy, 2003. High temperature superconductivity, 2002. News update, http://www.eren.doe.gov/superconductivity/pdfs/hts_apr02_hts_update.pdf, (accessed June 2002).
10. S. P. Hornfeldt, *Physica C* **341**, 2531-2533 (2000).
11. D. P. Norton, A. Goyal, J. D. Budai, D. K. Christen, D. M. Kroeger, E. D. Specht, Q. He, B. Saffian, M. Paranthaman, C. E. Klabunde, D. F. Lee, B. C. Sales, and F. A. List, *Science* **274**, (5288), 755-757 (1996).

12. E. D. Specht, F. A. List, D. F. Lee, K. L. More, A. Goyal, W. B. Robbins, and D. O'Neill, *Physica C-Superconductivity and Its Applications* **382**, (2-3), 342-348 (2002).
13. G. Celentano, V. Boffa, L. Ciontea, F. Fabbri, V. Galluzzi, U. Gambardella, A. Mancini, T. Petrisor, R. Rogai, A. Rufoloni, and E. Varesi, *Physica C* **372**, 790-793 (2002).
14. O. Stadel, J. Schmidt, G. Wahl, F. Weiss, D. Selbmann, J. Eickemeyer, O. Y. Gorbenko, A. R. Kaul, and C. Jimenez, *Physica C* **372** 751-754 (2002).
15. Y. Akin, E. Celik, W. Sigmund, and Y. S. Hascicek, *IEEE Transactions on Applied Superconductivity* **13**, (2), 2563-2566 (2003).
16. Y. Akin, Z. Aslanoglu, E. Celik, L. Arda, W. Sigmund, and Y. S. Hascicek, *IEEE Transactions on Applied Superconductivity* **13**, (2), 2673-2676 (2003).
17. M. P. Paranthaman, T. G. Chirayil, F. A. List, X. T. Cui, A. Goyal, D. F. Lee, E. D. Specht, P. M. Martin, R. K. Williams, D. M. Kroeger, J. S. Morrell, D. B. Beach, R. Feenstra, and D. K. Christen, *Journal of the American Ceramic Society* **84**, (2), 273-278 (2001).
18. T. G. Chirayil, M. Paranthaman, D. B. Beach, J. S. Morrell, E. Y. Sun, A. Goyal, R. K. Williams, D. F. Lee, P. M. Martin, D. M. Kroeger, R. Feenstra, D. T. Verebelyi, and D. K. Christen, in *Materials Research Society Symposium* (Materials Research Society, Warrendale, PA, USA, 1999), Vol. 574, p. 51-56.
19. P. Chaudhari, R. H. Koch, R. B. Laibowitz, T. R. McGuire, and R. J. Gambino, *Physical Review Letters* **58**, (25), 2684-2686 (1987).
20. T. R. Dinger, T. K. Worthington, W. J. Gallagher, and R. L. Sandstrom, *Physical Review Letters* **58**, (25), 2687-2690 (1987).
21. Y. Iijima, N. Tanabe, O. Kohno, and Y. Ikeno, *Applied Physics Letters* **60**, (6), 769-771 (1992).
22. A. Goyal, R. Feenstra, M. Paranthaman, J. R. Thompson, B. Y. Kang, C. Cantoni, D. F. Lee, F. A. List, P. M. Martin, E. Lara-Curzio, C. Stevens, D. M. Kroeger, M. Kowalewski, E. D. Specht, T. Aytug, S. Sathiyamurthy, R. K. Williams, and R. E. Ericson, *Physica C* **382**, 251-262 (2002).
23. R. F. Service, *Science* **295**, (5556), 787-787 (2002).
24. S. R. Foltyn, Q. X. Jia, P. N. Arendt, L. Kinder, Y. Fan, and J. F. Smith, *Applied Physics Letters* **75**, (23), 3692-3694 (1999).

25. D. P. Norton, C. Park, C. Prouteau, D. K. Christen, M. F. Chisholm, J. D. Budai, S. J. Pennycook, A. Goyal, E. Y. Sun, D. F. Lee, D. M. Kroeger, E. Specht, M. Paranthaman, and N. D. Browning, *Materials Science and Engineering B-Solid State Materials for Advanced Technology* **56**, (2-3), 86-94 (1998).
26. A. Gupta, R. Jagannathan, E. I. Cooper, E. A. Giess, J. I. Landman, and B. W. Hussey, *Applied Physics Letters* **52**, (24), 2077-2079 (1988).
27. R. E. Hummel, *Electronic Properties Materials* (Springer-Verlag, New York, 1993).
28. C. P. Poole Jr., H. A. Farach, and R. J. Creswick, *Superconductivity* (Academic Press, San Diego, 1995).
29. J. G. Bednorz and K. A. Muller, *Science* **237**, (4819), 1133 (1987).
30. C. Michel, M. Hervieu, M. M. Borel, A. Grandin, F. Deslandes, J. Provost, and B. Raveau, *Zeitschrift Fur Physik B-Condensed Matter* **68**, (4), 421-423 (1987).
31. H. Maeda, Y. Tanaka, M. Fukutomi, and T. Asano, *Japanese Journal of Applied Physics Part 2-Letters* **27**, (2), L209-L210 (1988).
32. Z. Z. Sheng and A. M. Hermann, *Nature* **332**, (6160), 138-139 (1988).
33. A. Schilling, M. Cantoni, J. D. Guo, and H. R. Ott, *Nature* **363**, (6424), 56-58 (1993).
34. T. G. Holesinger, P. S. Baldonado, N. Van Vo, W. M. Dai, K. R. Marken, and S. Hong, *IEEE Transactions on Applied Superconductivity* **9**, (2), 1800-1803 (1999).
35. Z. Z. Sheng, W. Kiehl, J. Bennett, A. Elali, D. Marsh, G. D. Mooney, F. Arammash, J. Smith, D. Viar, and A. M. Hermann, *Applied Physics Letters* **52**, (20), 1738-1740 (1988).
36. A. Goyal, M. Paranthaman, Q. He, F. A. List, E. D. Specht, D. K. Christen, D. M. Kroeger, J. E. Tkaczyk, and P. Haldar, *IEEE Transactions on Applied Superconductivity* **5**, (2), 1405-1408 (1995).
37. Super Power, Inc., 2003. HTS components and applications, http://www.igc.com/superpower/products/sp_products.asp, (accessed July 2003).
38. The University of Wisconsin Madison, 2003. Applied superconductivity center, <http://www.asc.wisc.edu/>, (accessed May 2003).
39. The University of Houston, 2003. Superconductivity center, <http://www.uh.edu/tcsuh/>, (accessed May 2002).

40. Stanford University, 2003. KGB research project, <http://www.stanford.edu/group/kgb/projects.html>, (accessed May 2003).
41. Oak Ridge National Laboratory, 2003. Superconductivity for electric systems, <http://www.ornl.gov/HTSC/htsc.html>, (accessed March 2003).
42. Los Alamos National Laboratory, 2003. Superconductivity technology center, <http://www.lanl.gov/orgs/mst/stc/stc.shtml> (accessed March 2003).
43. Argonne National Laboratory, 2003. Superconductivity center <http://superconductivity.et.anl.gov/>, (March 2003).
44. National High Magnetic Field Laboratory, 2003. HTS magnets and materials group, <http://www.nhmfl.gov/>, (accessed June 2003).
45. Oxford Instruments, 2003. HTS conductors, <http://www.oxford-instruments.com>, (accessed January 2003).
46. U.S. Department of Energy, 2002. <http://www.eren.doe.gov/superconductivity/statemap.html>, (accessed March 2003).
47. B. Ma, M. Li, Y. A. Jee, R. E. Koritala, B. L. Fisher, and U. Balachandran, *Physica C* **366**, (4), 270-276 (2002).
48. X. D. Wu, S. R. Foltyn, P. N. Arendt, W. R. Blumenthal, I. H. Campbell, J. D. Cotton, J. Y. Coulter, W. L. Hults, M. P. Maley, H. F. Safar, and J. L. Smith, *Applied Physics Letters* **67**, (16), 2397-2399 (1995).
49. S. R. Foltyn, P. N. Arendt, P. C. Dowden, R. F. DePaula, J. R. Groves, J. Y. Coulter, Q. X. Jia, M. P. Maley, and D. E. Peterson, *IEEE Transactions on Applied Superconductivity* **9**, (2), 1519-1522 (1999).
50. U.S. Department of Energy, 2003. Energy efficiency and renewable energy, http://www.eren.doe.gov/budget/pdfs/fy03_renewables.pdf, (accessed September 2003)
51. American Superconductors, 2002. Coated conductors, <http://www.amsuper.com/solutions.htm>, (accessed June 2002).
52. K. Helming, 2000. Texture and anisotropy of crystalline materials http://www.texture.de/index_e.htm, (accessed September 2003)
53. A. Goyal, *US Patent*, 6,375,768 (UT-Battelle, LLC, US, 2002)
54. D. Dimos, P. Chaudhari, and J. Mannhart, *Physical Review B* **41**, (7), 4038-4049 (1990).

55. D. P. Norton, D. H. Lowndes, J. D. Budai, D. K. Christen, E. C. Jones, K. W. Lay, and J. E. Tkaczyk, *Applied Physics Letters* **57**, (11), 1164-1166 (1990).
56. A. Goyal, J. D. Budai, D. M. Kroeger, D. P. Norton, E. D. Specht, and D. K. Christen, *Structures having enhanced biaxial texture and method of fabricating same* (UT-Battelle, LLC, US, 1999)
57. J. M. Phillips, *Journal of Applied Physics* **79**, (4), 1829-1848 (1996).
58. R. E. Russo, R. P. Reade, J. M. McMillan, and B. L. Olsen, *Journal of Applied Physics* **68**, (3), 1354-1356 (1990).
59. J. P. Singh, D. Shi, and D. W. Capone, *Applied Physics Letters* **53**, (3), 237-239 (1988).
60. W. Tao, M. P. Yuan, H. T. Huang, X. Z. Liao, X. M. Xie, H. L. Zhou, and Z. L. Wu, *Applied Physics Letters* **62**, (8), 894-895 (1993).
61. E. Furubayashi *Scripta Metallurgica Et Materialia* **27**, (11), 1493-1496 (1992).
62. H. Makita, S. Hanada, and O. Izumi, *Acta Metallurgica* **36**, (2), 403-412 (1988).
63. M. M. Borodkina and T. S. Orekhova, *Fizika Metallov I Metallovedenie* **54**, (6), 1204-1207 (1982).
64. J. Eickemeyer, D. Selbmann, R. Opitz, B. de Boer, B. Holzapfel, L. Schultz, and U. Miller, *Superconductor Science & Technology* **14**, (3), 152-159 (2001).
65. R. M. Nekkanti, V. Seetharaman, L. Brunke, I. Maartense, D. Dempsey, G. Kozlowski, D. Tomich, R. Biggers, T. Peterson, P. Barnes, and C. E. Oberly, *IEEE Transactions on Applied Superconductivity* **11**, (1), 3321-3324 (2001).
66. B. D. Cullity and S. R. Stock, *Elements of X-Ray Diffraction* (Prentice Hall, Upper Saddle River, 2001).
67. J. R. Thompson, A. Goyal, D. K. Christen, and D. M. Kroeger, *Physica C* **370**, 169-176 (2002).
68. B. de Boer, N. Reger, L. Fernandez, J. Eickemeyer, B. Holzapfel, L. Schultz, and W. Prusseit, *Physica C* **351**, (1), 38-41 (2001).
69. Q. He, D. K. Christen, J. D. Budai, E. D. Specht, D. F. Lee, A. Goyal, D. P. Norton, M. Paranthaman, F. A. List, and D. M. Kroeger, *Physica C* **275**, (1-2), 155-161 (1997).
70. E. Celik, Y. Akin, W. Sigmund, and Y. S. Hascicek, *IEEE Transactions on Applied Superconductivity* **13**, (2), 2669-2672 (2003).

71. T. Aytug, M. Paranthaman, H. Y. Zhai, H. M. Christen, S. Sathyamurthy, D. K. Christen, and R. E. Ericson, *Journal of Materials Research* **17**, (9), 2193-2196 (2002).
72. T. A. Gladstone, J. C. Moore, A. J. Wilkinson, and C. R. M. Grovenor, *IEEE Transactions on Applied Superconductivity* **11**, (1), 2923-2926 (2001).
73. P. Sachenko, J. H. Schneibel, J. G. Swadener, and W. Zhang, *Philosophical Magazine Letters* **80**, (9), 627-631 (2000).
74. E. Rabkin, L. Klinger, T. Izyumova, A. Berner, and V. Semenov, *Acta Materialia* **49**, (8), 1429-1438 (2001).
75. L. Klinger and E. Rabkin, *Interface Science* **9**, (1-2), 55-63 (2001).
76. M. X. Jin, E. Shimada, and Y. Ikuma, *Journal of Materials Research* **14**, (6), 2548-2553 (1999).
77. Y. Ikuma and S. Taku, *Journal of Materials Synthesis and Processing* **6**, (4), 267-270 (1998).
78. R. P. Reade, P. Berdahl, R. E. Russo, and S. M. Garrison, *Applied Physics Letters* **61**, (18), 2231-2233 (1992).
79. T. Araki, Y. Takahashi, K. Yamagiwa, Y. Iijima, K. Takeda, Y. Yamada, J. Shibata, T. Hirayama, and I. Hirabayashi, *Physica C* **357** 991-994 (2001).
80. D. K. Fork, D. B. Fenner, R. W. Barton, J. M. Phillips, G. A. N. Connell, J. B. Boyce, and T. H. Geballe, *Applied Physics Letters* **57**, (11), 1161-1163 (1990).
81. D. P. Norton, D. H. Lowndes, J. D. Budai, D. K. Christen, E. C. Jones, J. W. McCamy, T. D. Ketcham, D. St Julien, K. W. Lay, and J. E. Tkaczyk, *Journal of Applied Physics* **68**, (1), 223-227 (1990).
82. T. Aytug, J. Z. Wu, B. W. Kang, D. T. Verebelyi, C. Cantoni, E. D. Specht, A. Goyal, M. Paranthaman, and D. K. Christen, *Physica C* **340**, (1), 33-40 (2000).
83. C. M. Carlson, J. C. Price, P. A. Parilla, D. S. Ginley, D. Niles, R. D. Blaugher, A. Goyal, M. Paranthaman, D. M. Kroeger, and D. K. Christen, *Physica C* **304**, (1-2), 82-88 (1998).
84. F. Fabbri, C. Annino, V. Boffa, G. Celentano, L. Ciontea, U. Gambardella, G. Grimaldi, A. Mancini, and T. Petrison, *Physica C: Superconductivity* **341-348**, (4), 2503-2504 (2000).
85. Y. Akin, Z. K. Heiba, W. Sigmund, and Y. S. Hascicek, *Solid State Electronics* **47**, 2171-2175 (2003).

86. T. Aytug, J. Z. Wu, C. Cantoni, D. T. Verebelyi, E. D. Specht, M. Paranthaman, D. P. Norton, D. K. Christen, R. E. Ericson, and C. L. Thomas, *Applied Physics Letters* **76**, (6), 760-762 (2000).
87. C. Cantoni, T. Aytug, D. T. Verebelyi, M. Paranthaman, E. D. Specht, D. P. Norton, and D. K. Christen, *IEEE Transactions on Applied Superconductivity* **11**, (1), 3309-3312 (2001).
88. Q. X. Jia, S. R. Foltyn, P. N. Arendt, J. R. Groves, T. G. Holesinger, M. E. Hawley, and P. Lu, *Applied Physics Letters* **81**, (24), 4571-4573 (2002).
89. D. P. Norton, K. Kim, D. K. Christen, J. D. Budai, B. C. Sales, M. F. Chisholm, D. M. Kroeger, A. Goyal, and C. Cantoni, *Physica C* **372**, 818-820 (2002).
90. Y. Y. Zeng, Z. J. Zhang, W. A. Luo, N. P. Yang, Y. M. Cai, Z. Y. Hua, and X. L. Shen, *Thin Solid Films* **214**, (2), 235-237 (1992).
91. C. Cantoni, D. K. Christen, R. Feenstra, A. Goyal, G. W. Ownby, D. M. Zehner, and D. P. Norton, *Applied Physics Letters* **79**, (19), 3077-3079 (2001).
92. C. Cantoni, D. K. Christen, L. Heatherly, M. M. Kowalewski, F. A. List, A. Goyal, G. W. Ownby, D. M. Zehner, B. W. Kang, and D. M. Kroeger, *Journal of Materials Research* **17**, (10), 2549-2554 (2002).
93. M. Cyrot and D. Pavuna, *Introduction to Superconductivity and High-Tc Materials* (World Scientific, Singapore, 1992).
94. M. Ohring, *The Materials Science of Thin Films* (Academic Press, San Diego, 1991).
95. D. P. Norton, *Annual Review of Materials Science* **28**, 299-347 (1998).
96. M. Paranthaman, A. Goyal, F. A. List, E. D. Specht, D. F. Lee, P. M. Martin, Q. He, D. K. Christen, D. P. Norton, J. D. Budai, and D. M. Kroeger, *Physica C* **275**, (3-4), 266-272 (1997).
97. A. Ichinose, C. Y. Yang, D. C. Larbalestier, S. E. Babcock, A. Kikuchi, K. Tachikawa, and S. Akita, *Physica C* **324**, (3-4), 113-122 (1999).
98. M. Paranthaman, D. F. Lee, A. Goyal, E. D. Specht, P. M. Martin, X. Cui, J. E. Mathis, R. Feenstra, D. K. Christen, and D. M. Kroeger, *Superconductor Science & Technology* **12**, (5), 319-325 (1999).
99. S. Kreiskott, M. Getta, B. Monter, H. Piel, and N. Puper, *Physica C* **383**, (4), 306-314 (2003).
100. H. Fuji, T. Honjo, Y. Nakamura, T. Izumi, A. Takeshi, I. Hirabayashi, Y. Shiohara, Y. Iijima, and K. Takeda, *Physica C* **357**, 1011-1014 (2001).

101. C. Park, D. P. Norton, D. F. Lee, D. T. Verebelyi, A. Goyal, D. K. Christen, and J. D. Budai, *Physica C* **341**, 2481-2482 (2000).
102. C. Cai, R. I. Chakalova, G. Kong, K. Kawano, T. W. Button, J. S. Abell, and E. Maher, *Physica C* **372**, 786-789 (2002).
103. H. G. Lee, Y. M. Lee, H. S. Shin, C. H. Jung, D. Youm, and G. W. Hong, *Superconductor Science & Technology* **13**, (9), 1368-1372 (2000).
104. H. G. Lee, Y. M. Lee, H. S. Shin, C. J. Kim, and G. W. Hong, *Materials Science and Engineering B-Solid State Materials for Advanced Technology* **90**, (1-2), 20-24 (2002).
105. J. L. MacManus-Driscoll, *Annual Review of Materials Science* **28**, 421-462 (1998).
106. M. Nasatasi, J. W. Mayer, and J. K. Hirvonen, in *Cambridge Solid State Science Series* (Cambridge Univ. Press, Cambridge, 1996), p. 363-406.
107. R. M. Bradley, J. M. E. Harper, and D. A. Smith, *Journal of Applied Physics* **60**, (12), 4160-4164 (1986).
108. Y. Iijima, N. Tanabe, Y. Ikeno, and O. Kohno, *Physica C* **185**, 1959-1960 (1991).
109. K. Kakimoto, Y. Iijima, and T. Saitoh, *Physica C* **378**, 937-943 (2002).
110. J. R. Groves, P. N. Arendt, S. R. Foltyn, Q. X. Jia, T. G. Holesinger, H. Kung, R. F. DePaula, P. C. Dowden, E. J. Peterson, L. Stan, and L. A. Emmert, *Physica C* **382**, (1), 43-47 (2002).
111. U. Balachandran, M. Li, R. E. Koritala, B. F. Fisher, and B. Ma, *Physica C* **372**, 869-872 (2002).
112. U. Balachandran, B. Ma, A. Li, B. L. Fisher, R. E. Koritala, R. A. Erck, and S. E. Dorris, *Physica C* **378**, 950-954 (2002).
113. B. Ma, M. Li, B. L. Fisher, R. E. Koritala, and U. Balachandran, *Physica C* **382**, (1), 38-42 (2002).
114. Y. Sato, S. Honjo, Y. Takahashi, K. Muranaka, K. Fujino, T. Taneda, K. Ohmatsu, and H. Takei, *Physica C* **378** 1118-1121 (2002).
115. K. Hasegawa, Y. Nakamura, T. Izumi, and Y. Shiohara, *Physica C* **378** 955-959 (2002).
116. A. Furukawa, K. Sudoh, Y. Yoshida, N. Matsunami, and Y. Takai, *Physica C* **378** 932-936 (2002).

117. J. M. Phillips, in *High-Temperature Superconducting Materials Science and Engineering*, edited by D. Shi (Elsevier Science Inc., New York, 1995), p. 305-320.
118. X. Cui, F. A. List, D. M. Kroeger, D. F. Lee, M. Paranthaman, A. Goyal, B. W. Kang, E. D. Specht, P. M. Martin, and W. B. Robbins, *Physica C* **351**, (2), 175-181 (2001).
119. T. Kawae, S. Kambe, and O. Ishii, *Physica C: Superconductivity* **341-348**, (4), 2367-2368 (2000).
120. J. Yang, D. Shi, X. Wang, A. Liu, and G. Yuan, *Physica C: Superconductivity* **337**, (1-4), 67-70 (2000).
121. N. Savvides, A. Thorley, S. Gnanarajan, J. Herrmann, A. Katsaros, and A. Molodyk, *Physica C: Superconductivity* **341-348**, (4), 2491-2492 (2000).
122. J. O. Willis, P. N. Arendt, S. R. Foltyn, Q. X. Jist, J. R. Groves, R. F. DePaula, P. C. Dowden, E. J. Peterson, T. G. Holesinger, J. Y. Coulter, M. Ma, M. P. Maley, and D. E. Peterson, *Physica C* **335**, (1-4), 73-77 (2000).
123. Y. Ma, K. Watanabe, S. Awaji, and M. Motokawa, *Journal of Crystal Growth* **233**, (3), 483-489 (2001).
124. K. Onabe, T. Doi, N. Kashima, S. Nagaya, and T. Saitoh, *Physica C: Superconductivity* **378-381**, (2), 907-910 (2002).
125. V. Selvamanickam, G. B. Galinski, G. Carota, J. DeFrank, C. Trautwein, P. Haldar, U. Balachandran, M. Chudzik, J. Y. Coulter, and P. N. Arendt, *Physica C: Superconductivity* **333**, (3-4), 155-162 (2000).
126. C. C. Chang, X. D. Wu, A. Inam, D. M. Hwang, T. Venkatesan, P. Barboux, and J. M. Tarascon, *Applied Physics Letters* **53**, (6), 517-519 (1988).
127. S. Witanachchi, H. S. Kwok, X. W. Wang, and D. T. Shaw, *Applied Physics Letters* **53**, (3), 234-236 (1988).
128. R. K. Singh, J. Narayan, A. K. Singh, and J. Krishnaswamy, *Applied Physics Letters* **54**, (22), 2271-2273 (1989).
129. Y. Iijima, M. Hosaka, N. Tanabe, N. Sadakata, T. Saitoh, O. Kohno, and K. Takeda, *Applied Superconductivity* **4**, (10-11), 475-485 (1996).
130. Y. Qiao, Y. Li, S. Sathiraju, J. Reeves, K. Lenseth, and V. Selvamanickam, *Physica C-Superconductivity and Its Applications* **382**, (1), 48-51 (2002).
131. H. Hilgenkamp and J. Mannhart, *Reviews of Modern Physics* **74**, (2), 485-549 (2002).

132. M. Paranthaman, T. G. Chirayil, S. Sathyamurthy, D. B. Beach, A. Goyal, F. A. List, D. F. Lee, X. Cui, S. W. Lu, B. Kang, E. D. Specht, P. M. Martin, D. M. Kroeger, R. Feenstra, C. Cantoni, and D. K. Christen, *IEEE Transactions on Applied Superconductivity* **11**, (1), 3146-3149 (2001).
133. G. Hammerl, A. Herrnberger, A. Schmehl, A. Weber, K. Wiedenmann, C. W. Schneider, and J. Mannhart, *Applied Physics Letters* **81**, (17), 3209-3211 (2002).
134. D. Dimos, P. Chaudhari, J. Mannhart, and F. K. Legoues, *Physical Review Letters* **61**, (2), 219-222 (1988).
135. H. Hilgenkamp, C. W. Schneider, R. R. Schulz, B. Goetz, A. Schmehl, H. Bielefeldt, and J. Mannhart, *Physica C* **326-327**, 7-11 (1999).
136. A. Berenov, C. Farvacque, X. Qi, J. L. MacManus-Driscoll, D. MacPhail, and S. Foltyn, *Physica C* **372-376**, 1059-1062 (2002).
137. A. V. Berenov, R. Marriott, S. R. Foltyn, and J. L. MacManus-Driscoll, *IEEE Transactions on Applied Superconductivity* **11**, (1), 3780-3783 (2001).
138. A. Schmehl, B. Goetz, R. R. Schulz, C. W. Schneider, H. Bielefeldt, H. Hilgenkamp, and J. Mannhart, *Europhysics Letters* **47**, (1), 110-115 (1999).
139. G. Hammerl, A. Schmehl, R. R. Schulz, B. Goetz, H. Bielefeldt, C. W. Schneider, H. Hilgenkamp, and J. Mannhart, *Nature* **407**, (6801), 162-164 (2000).
140. J. T. Kucera and J. C. Bravman, *Physical Review B* **51**, (13), 8582-8590 (1995).
141. J. Mannhart, R. Gross, K. Hipler, R. P. Huebener, C. C. Tsuei, D. Dimos, and P. Chaudhari, *Science* **245**, (4920), 839-841 (1989).
142. T. Matsushita, H. Wada, T. Kiss, M. Inoue, Y. Iijima, K. Kakimoto, T. Saitoh, and Y. Shiohara, *Physica C* **378**, 1102-1107 (2002).
143. J. M. Phillips, in *High-Temperature Superconducting Materials Science and Engineering*, edited by D. Shi (Elsevier Science Inc., New York, 1994), p. 321-344.
144. R. W. Schwartz, *Chemistry of Materials* **9**, (11), 2325-2340 (1997).
145. F. F. Lange, *Science* **273**, (5277), 903-909 (1996).
146. C. J. Brinker and G. W. Scherer, *Sol-Gel Science: The Physics and Chemistry of Sol-Gel Processing* (Academic Press, San Diego, 1990).
147. D. E. Bornside, C. W. Macosko, and L. E. Scriven, *Journal of Imaging Technology* **13**, (4), 122-130 (1987).

148. E. Celik, H. Okuyucu, I. H. Mutlu, M. Tomsic, J. Schwartz, and Y. S. Hascicek, *IEEE Transactions on Applied Superconductivity* **11**, (1), 3162-3165 (2001).
149. J. S. Morrell, Z. B. Xue, E. D. Specht, A. Goyal, P. M. Martin, D. F. Lee, R. Feenstra, D. T. Verebelyi, D. K. Christen, T. G. Chirayil, M. Paranthaman, C. E. Vallet, and D. B. Beach, *Journal of Materials Research* **15**, (3), 621-628 (2000).
150. T. G. Chirayil, M. Paranthaman, D. B. Beach, D. F. Lee, A. Goyal, R. K. Williams, X. Cui, D. M. Kroeger, R. Feenstra, D. T. Verebelyi, and D. K. Christen, *Physica C* **336**, (1-2), 63-69 (2000).
151. S. Sathyamurthy, M. Paranthaman, H. Y. Zhai, H. M. Christen, P. M. Martin, and A. Goyal, *Journal of Materials Research* **17**, (9), 2181-2184 (2002).
152. A. Gupta, G. Koren, E. A. Giess, N. R. Moore, E. J. M. Osullivan, and E. I. Cooper, *Applied Physics Letters* **52**, (2), 163-165 (1988).
153. T. Kumagai, H. Yokota, K. Kawaguchi, W. Kondo, and S. Mizuta, *Chemistry Letters*, (8), 1645-1646 (1987).
154. J. T. Dawley, P. G. Clem, M. P. Siegal, D. L. Overmyer, and M. A. Rodriguez, *IEEE Transactions on Applied Superconductivity* **11**, (1), 2873-2876 (2001).
155. M. P. Siegal, P. G. Clem, J. T. Dawley, R. J. Ong, M. A. Rodriguez, and D. L. Overmyer, *Applied Physics Letters* **80**, (15), 2710-2712 (2002).
156. M. W. Rupich, Q. Li, S. Annavarapu, C. Thieme, W. Zhang, V. Prunier, M. Paranthaman, A. Goyal, D. F. Lee, E. D. Specht, and F. A. List, *IEEE Transactions on Applied Superconductivity* **11**, (1), 2927-2930 (2001).
157. D. L. Shi, Y. L. Xu, S. X. Wang, J. Lian, L. M. Wang, S. M. McClellan, R. Buchanan, and K. C. Goretta, *Physica C* **371**, (2), 97-103 (2002).
158. P. C. McIntyre, M. J. Cima, J. A. Smith, R. B. Hallock, M. P. Siegal, and J. M. Phillips, *Journal of Applied Physics* **71**, (4), 1868-1877 (1992).
159. Y. Takahashi, Y. Aoki, T. Hasegawa, Y. Iijima, T. Saito, I. Hirabayashi, T. Honjo, Y. Yoshida, Y. Takai, and Y. Shiohara, *Physica C* **378** 1024-1027 (2002).
160. H. Okuyucu, M. K. Ramazanoglu, Y. Akin, T. Alp, W. Sigmund, J. E. Crow, and Y. S. Hascicek, in *CEC/ICMC, Advances in Cryogenics Engineering*, edited by U. Balachandran (American Institute of Physics, Wisconsin, Madison, 2001), Vol. 48 B, p. 557-563.
161. T. J. B. Holland and S. A. T. Redfern, *Mineralogical Magazine* **61**, (1), 65-77 (1997).

162. J. I. Goldstein, D. E. Newbury, P. Echlin, D. C. Joy, A. D. Roming, Jr., C. E. Lyman, C. Fiori, and E. Lifshin *Scanning Electron Microscopy and X-Ray Microanalysis* (Plenum Press, New York, 1992).
163. D. J. Dingly, in *Electron Backscatter Diffraction in Materials Science*, edited by A. J. Schwartz, M. Kumar and B. L. Adams (Kluwer Academic, New York, 2000)
164. J. Reeves, 1999. Using orientation imaging microscopy to investigate current flow barriers in high temperature superconductors, (<http://filebox.vt.edu/eng/mech/writing/me5984/examples/reeves.html>, (accessed August 2003).
165. T. Aytug, M. P. Paranthaman, B. W. W. Kang, D. B. Beach, S. Sathyamurthy, E. D. Specht, D. F. Lee, R. Feenstra, A. Goyal, D. M. Kroeger, K. J. Leonard, P. M. Martin, and D. K. Christen, *Journal of the American Ceramic Society* **86**, (2), 257-265 (2003).
166. A. Goyal, S. X. Ren, E. D. Specht, D. M. Kroeger, R. Feenstra, D. Norton, M. Paranthaman, D. F. Lee, and D. K. Christen, *Micron* **30**, (5), 463-478 (1999).
167. E. Varesi, V. Boffa, G. Celentano, L. Ciontea, F. Fabbri, V. Galluzzi, U. Gambardella, A. Mancini, T. Petrison, A. Rufoloni, and A. Vannozzi, *Physica C* **372**, 763-766 (2002).
168. T. G. Truchan, F. H. Rountree, M. T. Lanagan, S. M. McClellan, D. J. Miller, K. C. Goretta, M. Tomsic, and R. Foley, *IEEE Transactions on Applied Superconductivity* **10**, (1), 1130-1133 (2000).
169. W. H. Shih and Q. Lu, in (*MRS Sym Proc*, 1993), Vol. 248, p. 481.
170. R. W. Schwartz, T. J. Boyle, S. J. Lockwood, M. B. Sinclair, D. Dimos, and C. D. Buchheit, *Integrated Ferroelectrics* **7**, (1-4), 259-277 (1995).
171. R. W. Schwartz, J. A. Voigt, B. A. Tuttle, D. A. Payne, T. L. Reichert, and R. S. DaSalla, *Journal of Materials Research* **12**, (2), 444-456 (1997).
172. S. Oh, J. Yoo, K. Lee, J. Kim, and D. Youm, *Physica C* **308**, (1-2), 91-98 (1998).
173. A. P. Malozemoff, S. Annavarapu, L. Fritzemeier, Q. Li, V. Prunier, M. Rupich, C. Thieme, W. Zhang, A. Goyal, M. Paranthaman, and D. F. Lee, *Superconductor Science & Technology* **13**, (5), 473-476 (2000).
174. H. J. Kim, J. Joo, B. K. Ji, B. H. Jun, C. H. Jung, S. D. Park, H. W. Park, G. W. Hong, and C. J. Kim, *IEEE Transactions on Applied Superconductivity* **13**, (2), 2555-2558 (2003).

- 175. K. Ohmatsu, K. Muranaka, T. Taneda, K. Fujino, H. Takei, N. Hobara, S. Honjo, and Y. Takahashi, *IEEE Transactions on Applied Superconductivity* **13**, (2), 2462-2465 (2003).
- 176. H. Y. Zhai and W. K. Chu, *Applied Physics Letters* **76**, (23), 3469-3471 (2000).
- 177. CRC, *CRC Handbook of Chemistry and Physics*, (83 Edition).
- 178. L. Vegard, *Z. Physics* **5**, (17), (1921).

BIOGRAPHICAL SKETCH

Yalcin Akin was born on March 23, 1970, in Izmit, Turkey. He grew up and attended elementary and secondary schools in his hometown and he graduated from Izmit Technical High School in 1988. He went on to Dokuz Eylul University, Izmir, Turkey, and completed his Bachelor of Science (B.S.) in mineral engineering in 1993. After that he started his Master of Science at the Istanbul Technical University, and worked as a research assistant. Then he came to Gainesville, FL, U.S.A., and attended The University of Florida, Department of Materials Science and Engineering, and he earned his Master of Science (M.S.) in December 1998. After that he continued his Ph.D. with Dr. Sigmund, and he began work on his dissertation topic with development of buffer layers by chemical solution deposition for YBCO coated conductors. After he finished his Ph.D. course work and qualifying exam he went to the National High Magnetic Field Laboratory (NHMFL), Tallahassee, FL, and joined Dr. Hascicek's group. He performed the research to complete his Ph.D. dissertation at the NHMFL. In spite of his Ph.D. research he contributed several projects to the NHMFL. During his Ph.D. education he attended and presented at several national and international conferences and workshops like the Applied Superconductivity Conference in 2000 and 2002, the 9th International Workshop on Oxide Electronics in 2002, International Magnet Technology Conference in 1999 and 2001, and the International Cryogenic Materials Conference in 2001 and 2003. He has written more than 30 scientific papers, which were published in journals and peer

reviewed conference proceedings. He is one of the founders of Innovative Environmental Magnets and Materials, Inc.

I certify that I have read this study and that in my opinion it conforms to acceptable standards of scholarly presentation and is fully adequate, in scope and quality, as a dissertation for the degree of Doctor of Philosophy.



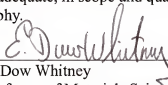
Wolfgang M. Sigmund, Chair
Associate Professor of Materials Science
and Engineering

I certify that I have read this study and that in my opinion it conforms to acceptable standards of scholarly presentation and is fully adequate, in scope and quality, as a dissertation for the degree of Doctor of Philosophy.



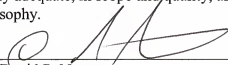
Yusuf S. Hascicek, Cochair
Scholar/Scientist of National High Magnetic
Field Laboratory, Tallahassee, Florida

I certify that I have read this study and that in my opinion it conforms to acceptable standards of scholarly presentation and is fully adequate, in scope and quality, as a dissertation for the degree of Doctor of Philosophy.



E. Dow Whitney
Professor of Materials Science and
Engineering

I certify that I have read this study and that in my opinion it conforms to acceptable standards of scholarly presentation and is fully adequate, in scope and quality, as a dissertation for the degree of Doctor of Philosophy.



David P. Norton
Professor of Materials Science and
Engineering

I certify that I have read this study and that in my opinion it conforms to acceptable standards of scholarly presentation and is fully adequate, in scope and quality, as a dissertation for the degree of Doctor of Philosophy.



Charles R. Martin
Professor of Chemistry

This dissertation was submitted to the Graduate Faculty of the College of Engineering and to the Graduate School and was accepted as partial fulfillment of the requirements for the degree of Doctor of Philosophy.

December 2003



Pramod P. Khargonekar
Dean, College of Engineering

Winfred M. Phillips
Dean, Graduate School